

Magneto-optic holographic three-dimensional
display with artificial magnetic lattice

January 2017

DOCTOR OF ENGINEERING

Kazuki Nakamura

TOYOHASHI UNIVERSITY OF TECHNOLOGY

Date of Submission:

January 10th, 2017

Department of Electrical and Electronic Information Engineering	Student ID Number	103328	Supervisors	Hiroyuki Takagi
Applicant's name	Kazuki Nakamura			Yuichi Nakamura

Abstract

Title of Thesis	Magneto-optic holographic three-dimensional display with artificial magnetic lattice
-----------------	--

Holographic display is expected as an attractive technique to visualize three-dimensional (3D) images with high presence. For practical use, a high speed display, which can represent holograms with order of light wavelength, is required. The magneto-optic holographic three-dimensional display expected to solve this problem by using magnetic media which is excellent in recording speed and recording density. In particular, by using artificial magnetic lattice, a media had high brightness and could be recorded by low energy, and reduction of noise of magnetic hologram was realized. In addition, calculation methods of computer generated holograms for complex 3D object, optical systems to represent holographic video, and quality improvement of reconstructed images were discussed.

1. Magnetic holographic media with artificial magnetic lattice

To applicate magnetic hologram for holographic display, light efficiencies of recording and reconstructing of hologram were regarded as a problem, and these efficiencies dominated by media material. In this thesis, by using the magnetophotonic crystal (MPC), recording and reconstructing light efficiencies were improved. The diffraction efficiency of MPC was $2.1 \times 10^{-2}\%$, and required illumination light to represent 100 cd/m^2 brightness reduced from 24 mW/cm^2 to 10.8 mW/cm^2 compared to a case of amorphous terbium iron (*a*-TbFe) film. In addition, a multilayer structure which comprised two different magnetic materials as magnetic hologram media showing high diffraction efficiency and low writing energy was proposed.

2. Computer generated holograms for magneto-optic holographic three dimensional display

To calculate complex object with surface, two-dimensional image based method was adopted. This method was suitable for generating complicated hologram composed of many point light sources. Holograms on magneto-optic holographic three-dimensional display were binary hologram and, usual reconstructed images with binary holograms included binarization errors. I focused on that pixel position of magnetic hologram wasn't fixed mechanically. To reduce binarization errors, pixels position of holograms was considered by simulated annealing (SA) method, and error value included in simulated reconstruction images were reduced.

3. Optical systems for holographic video

The holographic video system consisted of three elements; hologram recording system, hologram reconstruction system and erasure system of magnetic hologram. To demonstrate holographic video, synchronization of recording and erasure systems were constructed. By using the optical system, a holographic video, rotating wireframe cube, was displayed with the optical system: framerate was 10 fps, $13.6 \mu\text{m/pixel}$, 367×367 pixels. In addition, the new hologram recording system used micro lens array matching to DMD pixels to reduce scanning length.

4. Representing method of color and gray scale holograms

In previous chapters, the magneto-optic holographic three-dimensional display has developed to represent holographic video with monochrome. However, in order to put it into practical use, colorization and multilevel gradations of reconstruction images are important. To proof principle of colorization, the optical space division method was adopted. By using the thickness designed BiDyYFeAlG films, the synthesized reconstructed image covered standard RGB color region included white color.

By effectively combining these elements of technologies, magneto-optic holographic display could be expected more realistic and natural 3D images. In addition, each element technologies can be applied to other optical addressed spatial light modulator and storages using magneto-optic effect.

Date of Submission:

平成 29年 1月 10日

Department 電気・電子情報工学専攻	Student ID Number 学籍番号	第 103328 号	Supervisors 指導教員	高木 宏幸
Applicant's name 氏名	中村 和樹			中村 雄一

Abstract

論文内容の要旨 (博士)

Title of Thesis 博士学位論文名	Magneto-optic holographic three-dimensional display with artificial magnetic lattice (人工磁気格子を用いた磁気光学ホログラフィック 3次元ディスプレイ)
----------------------------	--

(要旨 1,200字程度)

自然な立体像を表示できる3次元(3D)表示技術にホログラフィックディスプレイがある。本ディスプレイを実現するには、光の波長レベルの周期構造であるホログラムを高速かつ高密度に表示できるディスプレイの開発が重要である。

本論文では、ホログラムの表示に必要な高密度の情報を高速に記録し表示できる磁性体を用いた磁気光学ホログラフィック 3Dディスプレイの開発を行った。特に人工磁気格子構造を用いることで、高輝度かつ低エネルギー記録の磁性体、磁気ホログラムのノイズ低減を実現した。また、複雑な3D像のホログラムの計算方法、3D像を動画速度で表示させる光学系、再生像の画質向上について検討した結果を報告する。

1. 人工磁気格子を用いた磁気ホログラムメディア

磁気ホログラムをディスプレイに応用する際に、磁性体の材料で決まる記録および再生時の光効率が課題となる。本論文では、人工磁気格子構造である磁性フォトニック結晶 (MPC) をディスプレイに用いることで、記録効率および回折効率を向上し、輝度100 cd/m²の画像の表示に必要な照明光の強度を従来の24 W/cm²から10 W/cm²まで低減できることを示した。さらに、記録エネルギーに優れる希土類遷移系金属合金膜と、回折効率に優れる磁性ガーネット系薄膜を組み合わせた構造を作製することで、低記録エネルギーかつ高回折効率を実現した。

2. 磁気ホログラムディスプレイのための計算機合成ホログラム

複雑な3D像のホログラムを計算するために2次元面間の光伝搬を基本としたホログラム計算手法を用いた。本手法は多数の点光源から構成される複雑な物体のホログラムの生成に適した方法である。さらに、先行研究の磁気ピクセルは、光照射の有無によるバイナリホログラムであった。2値化の際に生じるノイズの低減手法として、機械的なピクセル構造を必要としないという本ディスプレイの特徴に着目し、磁気ピクセルの位置を制御することでノイズ低減を行った。

3. 動画表示のための光学系構築

磁気ホログラムを用いた動画表示のために、連続的な磁気ホログラムの記録再生を行った。外部磁界印加による磁気ピクセルの初期化と熱磁気書き込みを繰り返すことで10 Hzでの動画再生を実現した。しかし、光学系の関係から低視野角にとどまっていたため、広視野角の動画再生を目的にマイクロレンズアレイを用いた新たな記録光学系を作製し、その原理実証を行った。

4. 表示像のカラー化および多値化

本章までの研究は、モノクロの立体像表示を実現することを目的としたが、応用を考える上でホログラムの多階調表示および、カラー表示は重要である。磁気ホログラムを用いたカラー像表示の原理実証として、空間分割方式を用いることで、白色を含むsRGB規格の色調表現を実現した。また、書き込み光のエネルギー密度を制御することで1ピクセル中の磁気光学効果の大きさを制御し、4値のグレー表現を実現した。

本研究で確立した手法を組み合わせることで、ホログラフィックディスプレイを実現できるだけでなく、光アドレス型空間光変調器の開発や磁気光学効果を用いた情報記録技術にも大きく貢献できるものと考えられる。

Index

1. Introduction.....	1
1.1 Background.....	1
1.2 Visualization of three dimensional images	2
1.2.1 Physiological factors of stereoscopic vision.....	2
1.2.2 Three dimensional displays	3
1.3 Holography and holographic display	4
1.3.1 Holography.....	4
1.3.2 Holographic display.....	6
1.3.3 Holographic display with optical scanning.....	8
1.4 Magneto-optic holographic three-dimensional display.....	9
1.4.1 Magneto-optic effect	9
1.4.2 Magnetic hologram	12
1.4.3 Previous works of magneto-optic holographic three-dimensional display	15
1.5 Outline of the research	21
References	23
2. Magnetic holographic medium with artificial magnetic lattice	26
2.1 Introduction	26
2.2 Background of magnetic media	27
2.2.1 Basic requests for magnetic material	27
2.2.2 Diffraction efficiency of magnetic hologram	28
2.2.3 Illumination light power required for reconstructing hologram.....	30
2.3 Controlling magneto-optical property with artificial magnetic lattice	31
2.3.1 Magnetophotonic crystals	31
2.3.2 Numerical calculation for designing media structure	33
2.4 Development of magnetic garnet media with artificial magnetic lattice.....	35
2.4.1 Samples fabrication.....	35
2.4.2 Magneto-optical and optical properties	37
2.4.3 Measurement of diffraction efficiency.....	38
2.4.4 Reconstruction of 3D image.....	41
2.5 Artificial magnetic lattice media with dissimilar materials	42
2.5.1 Design of structure	42
2.5.2 Sample fabrication.....	44
2.5.3 Evaluation of light efficiencies	45

2.5.4 Reconstruction of 3D image.....	47
2.6 Summary.....	48
References.....	49
3. Computer generated hologram for binary hologram.....	51
3.1 Introduction.....	51
3.2 Hologram calculation with point based method.....	52
3.2.1 Fresnel zone plate.....	52
3.2.2 Half zone plate method.....	53
3.3 Hologram calculation with two-dimensional image based method.....	54
3.3.1 Angular spectrum and light propagation.....	54
3.3.2 Computing light propagation.....	57
3.3.3 Calculation process of 2D image-based method.....	60
3.3.4 Calculation process of occlusions.....	62
3.4 Hologram optimization with simulated annealing.....	64
3.4.1 Simulated annealing.....	64
3.4.2 Parameters of simulated annealing.....	66
3.4.3 Comparison of error value.....	68
3.5 Summary.....	71
References.....	72
4. Optical systems for holographic video.....	75
4.1 Introduction.....	75
4.2 Rewriting of magnetic holograms.....	76
4.2.1 Optical system for continuously recording and erasing magnetic holograms.....	76
4.2.2 Magneto-optical properties of amorphous TbFe film with thermal assist.....	76
4.2.3 Continuously recording and erasure of magnetic hologram.....	80
4.3 Optical system with micro lens array for holographic video.....	83
4.3.1 Recording algorithm.....	83
4.3.2 Overview of optical system.....	85
4.3.3 Recording of arbitrary image.....	86
4.3 Summary.....	87
References.....	88
5. Representing method of color and gray holograms.....	89
5.1 Introduction.....	89

5.2 Colorization of reconstructed image	90
5.2.1 Wavelength dependence of brightness	90
5.2.2 Magnetic films for each color	92
5.2.3 Optical space division method	93
5.2.4 Reconstruction of color image	94
5.3 Representation of gray level hologram	97
5.3.1 Faraday rotation angle modulation	97
5.3.2 Evaluation of Faraday rotation angle	99
5.3.3 Reconstruction of magnetic hologram with multilevel brightness	102
5.4 Summary	104
References	105
6. Conclusion	107
Acknowledgments	109
Research achievements.....	110

1. Introduction

1.1 Background

Display technologies are being developed to represent more realistic and natural images. While flat panel displays with 4k resolution have been in use, 8k displays have also recently been developed [1], [2]. These resolutions of images represented on two dimensional (2D) displays have reached the resolution limit of our eyes [1]. On the other hand, three-dimensional (3D) displays are also an attractive approach for visualization of realistic images. Of late, interest in 3D video has had a resurgence for entertainment applications [3]. Some products and services with 3D display are in the market. However, many of them have limitations with 3D information. For example, 3D movies in cinemas can represent binocular stereoscopic vision, but not a motion parallax corresponding to view point.

Holographic displays can reconstruct realistic 3D images without the need for the viewer to wear special glasses [4]. The reconstructed image can satisfy physiological factors for recognizing 3D spaces. However, holographic displays are difficult to build, as they require submicron scale pixels for reconstructing 3D images with a wide viewing angle [3], [5]. To build holographic displays with wide viewing angle, many approaches that use multiplex high speed spatial light modulators and optical scanners have been proposed [6][7]. However, the size of the optical systems required for this approach tends to be large because it requires the optical imaging system to display hologram patterns; if holograms could be recorded on non-volatile material, optical systems with this approach could be chosen over other optical imaging systems.

A wide-viewing-angle holographic display based on magnetic hologram was previously proposed by this project group [8]. This display consisted of a magnetic medium as screen and an optical system to record and reconstruct holograms on the screen. The magneto-optic holographic three-dimensional display uses magnetic domains on the magnetic medium with perpendicular magnetization as submicron scale pixels. Light incident on the display is modulated by the magneto-optic effect [9], [10]. The magnetic pixels can be controlled with a switching speed quicker than 1 μ s using thermomagnetic recording with an optical addressing method. In previous work, this project group demonstrated the reconstruction of still 3D images with a viewing angle greater than 30° using amorphous terbium iron film [8], [11]. However, the optical system took several minutes to record a hologram, and the reconstructed image had low brightness.

This thesis is about the development of a magneto-optic holographic three-dimensional display that can represent holographic video with clear images. To use magnetic material for holographic displays, structures of magnetic medium, calculation methods

of computer generated holograms, and optical systems to drive tiny magnetic pixels were discussed. All elemental technologies for magneto-optic holographic three-dimensional display have been established in this thesis. Chapter 1 discusses the basics of three-dimensional displays and the background of this research.

1.2 Visualization of three dimensional images

1.2.1 Physiological factors of stereoscopic vision

This section describes the basics of human vision for recognizing 3D space [4], [12]. Humans recognize 3D spaces and object-position relationships by using oculomotor and visual information. Table 1.2.1-1 contains roughly-grouped physiological factors for recognizing 3D spatial relationships. The spatial relationships are caused by human perception mechanisms and the morphology of eyes; they are stimulated by monocular vision (single-eyed vision), binocular vision (properly-combined two-eyed vision), or by static or moving images in various combinations.

The primary cue is obtained from the triangulation of point sources by binocular vision. Implicit in this are other cues arising from the motion of one eye from side to side, which makes a kind of “temporal triangulation” possible, although the sliding of near objects over far objects also seems to be an important cue. Human eyes fixate on a point to get an image, and the angle of convergence between the eyes is sensed via muscular proprioception. Binocular cues are based on, and easily affected by, monocular cues—especially overlap cues. The fact that one object’s image terminates at the boundary of another object’s, is convincing evidence that it is behind the other and is being hidden by it, despite possibly conflicting binocular cues. This effect can be demonstrated by an animation using two white lines.

Table 1.2.1-1 Physiological factors to recognize spatial space and 3D objects [12].

	Static	Dynamic
Monocular	Overlap	Kinetic depth
	Perspective	effect
	Focus, etc.	Motion parallax
Binocular	Convergence	
	Fusion	-
	Edge effects	

1.2.2 Three dimensional displays

In 1838, Charles Wheatstone invented the Wheatstone stereoscope, the earliest one of its kind [13]. Since then, various display technologies for visualizing 3D images have been demonstrated and studied. This section discusses the advantages and disadvantages of each type of 3D display. Binocular displays, multi-view displays, and integral imaging displays are dealt with in this section [4]. Holographic displays are discussed in the next section.

(1) Binocular displays

This method uses two 2D images, which are given a parallax corresponding to the vision of both eyes, and each image is delivered to the viewer's left and right eye, respectively. The human brain synthesizes these images into one and recognizes it as binocular stereoscopic vision. A set of two images is generated by multiplexing methods, e.g., utilizing wavelength (anaglyph), polarization, and timing. These division methods require special glasses to separate the images. Another effective approach that requires no glasses is controlling the direction of light, such as the parallax barrier and lenticular lens methods. These approaches are effective for perception of stereoscopic vision. However, the static monocular cues mentioned in table 1.2.1-1 do not work, and this induces eyestrain for long term viewing. The eyestrain is caused by the mismatch between binocular parallax and monocular parallax. In addition, the binocular display does not receive overlapped object information.

(2) Multi-view displays

Multi-view displays enlarge the viewpoint of binocular displays by creating a discrete set of perspective views per frame and distributing them across the viewing field. This method provides motion parallax corresponding to observer movement in the viewing zone, and viewing freedom for one or more observers. In principle, multi-view displays reduce the resolution of each image. However, 3D images can be seen without any special glasses.

(3) Integral imaging displays

This technology is based on Integral Photography, which was a kind of stereoscopic photography introduced by Lippmann in 1908 [14]. A set of 2D images with different perspectives are displayed and synthesized on a plane via a lens array. The set of images can create a 3D image. They can inherently provide full and continuous motion parallax. In addition, the created 3D images can be observed by several viewers with multiple viewing positions. These 3D images have low lateral and depth resolution, and a limitation of depth range.

1.3 Holography and holographic display

1.3.1 Holography

Holography was invented by Dennis Gabor in 1948 [15] when he proposed “wavefront reconstruction” as a new principle in microscopy. In the 1960s, hologram technology was dramatically improved by E.N. Leith and J. Upatnieks [16]–[18]. Y. N. Denisyuk invented reflection hologram by synthesizing ideas of Gabor and G. Lippmann. The other important progress in display holography was the invention of rainbow holograms by S.A. Benton [19]. These methods can be characterized by recording method, optical system, and light sources. In addition, holography has been studied for reasons other than display, such as holographic memory [20]–[23].

Holography can be said to be a technology that records all the information included in light, such as phase, intensity, and wavelength. Figure 1.3.1-1 shows the basic principle of recording and reconstruction of a hologram. Figure 1.3.1-1 (a) shows hologram recording—signal light is diffracted by, or scattered from, an object and coherent reference waves are incident on photosensitive materials, light information about the amplitude and phase of the diffracted or scattered waves can be recorded as transmittance or refractive index distributions. The recorded interference pattern is called “hologram”. Later, when reference light is incident on the recorded area, the object light field can be reconstructed. 3D images can be observed via the photosensitive material. The fringe pattern on the media is described below. The intensity of the sum of two complex fields then depends on both the amplitude and phase of the unknown field. Thus, if

$$a(x, y) = |a(x, y)|\exp[-j\varphi(x, y)] \quad (1.3.1-1)$$

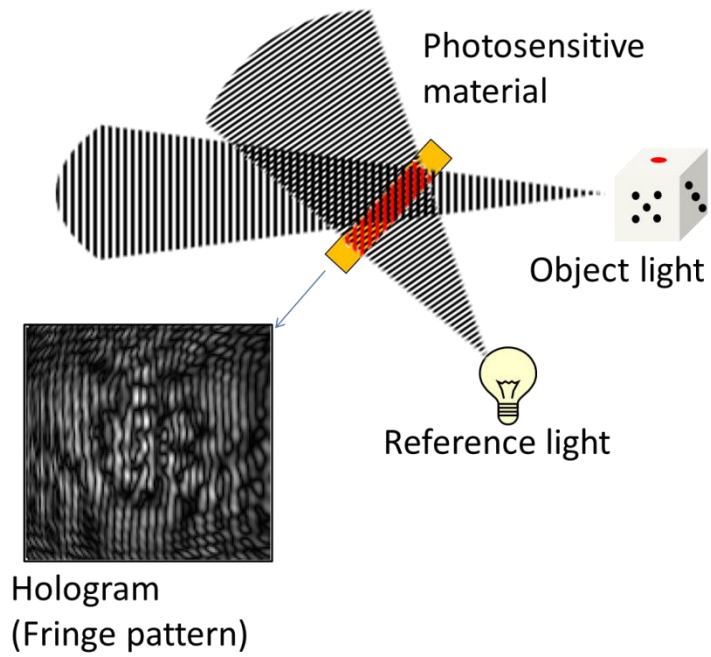
represents the wavefront to be detected and reconstructed, and if

$$A(x, y) = |A(x, y)|\exp[-j\Psi(x, y)] \quad (1.3.1-2)$$

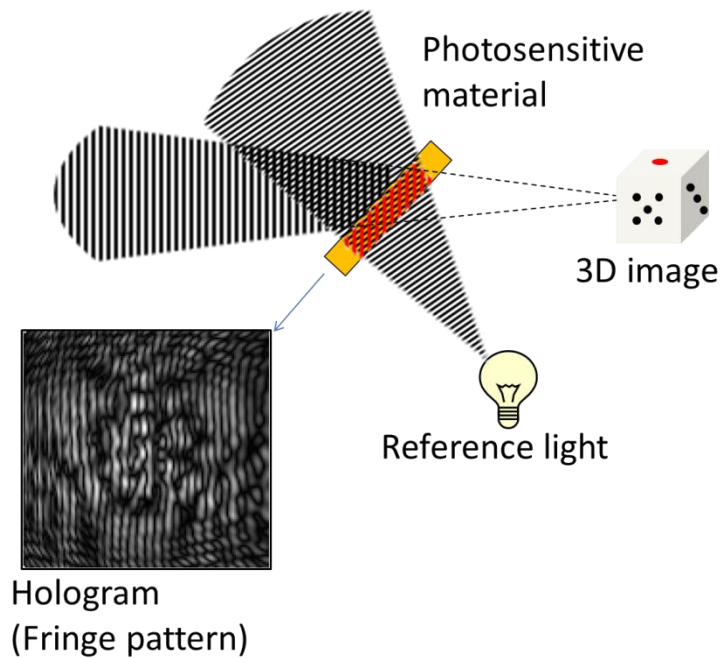
represents the “reference” wave with which $a(x, y)$ interferes, the intensity of the sum is given by

$$I(x, y) = |A(x, y)|^2 + |a(x, y)|^2 + 2|A(x, y)||a(x, y)| \cos[\Psi(x, y) - \varphi(x, y)]. \quad (1.3.1-3)$$

$I(x, y)$ includes the whole information of object light and reference light. If the interference pattern and reference light are known, the hologram can be reconstructed.



(a)



(b)

Fig. 1.3.1-1 Schematic image of hologram recording and reconstruction on photosensitive material medium. (a) Hologram recording on a photosensitive material. (b) Hologram reconstruction with reference light using the same optical setup.

1.3.2 Holographic display

Holographic displays, which represent holograms on spatial light modulators (SLMs), have been studied to develop high presence 3D displays [24], [25]. The reconstructed 3D image can potentially satisfy the physiological factors of stereoscopic vision [4], and can accurately represent an object's shape, position, and size. These characteristics emerge from using diffraction to represent 3D images. Table 1.3.2-1 shows a comparison of the major 3D display technologies.

The first holographic display was proposed in 1966 [26]. Basic elements of the holographic display are an SLM, an illumination light source with high coherence, and holograms that are represented on the SLM. However, holographic display is not in practical use [25]. The reason for this is pixel size and number in the SLMs [3]. A key characteristic of holographic displays is viewing angle, which means visible area of reconstructed images. The viewing angle depends on the pixel size of SLM. A relationship between the viewing angle and pixel size can be expressed as below,

$$\theta = 2\sin^{-1}\left(\frac{\lambda}{2p}\right) \quad (1.3.2-1)$$

Where, θ is the viewing angle, p is the pixel size of SLMs, and λ is the wavelength of illumination light.

Figure 1.3.2-1 shows preliminary calculation results of the relationship between viewing angle and pixel size. At present, there are electronic holographic displays utilizing conventional SLMs (for example, liquid crystal SLMs and digital micromirror devices). However, these 3D electronic holographic displays cannot deliver 3D images over a wide range of viewing angles because their working pixels have dimensions in the range 10–100 μm . The limit on downsizing the pixel size in SLMs come from fabrication processes or the necessity of introducing current lines. According to estimations, SLMs with 1 μm pixels can display holographic images for viewing angles of more than 30°. The other issue is the number of pixels required to represent a hologram. The right vertical axis in Fig 1.3.2-1 means the required number of pixels to fulfill an area equivalent to an iPhone 5's display. The number of pixels is calculated with a fill factor of 1.0. A holographic iPhone5 would require over 10^9 pixels, which is approximately 100 times the number in an 8k display. In addition, all pixels need to be controlled to represent holograms with wide viewing angle.

Table 1.3.2-1 3D display types and provided depth cues [4].

Type of 3D display	Provided depth cues			Remarks on possible limitations
	Disparity	Motion parallax	Focus	
Binocular	✓			Limited comfort depth range Shear distortion
Multi-view	✓	(✓)		Limited comfort depth range Only horizontal motion parallax Picket-fence effect Image flipping, Limited resolution
Integral imaging	✓	✓		Limited depth range Limited resolution
Holographic	✓	✓	✓	Limited 3D volume

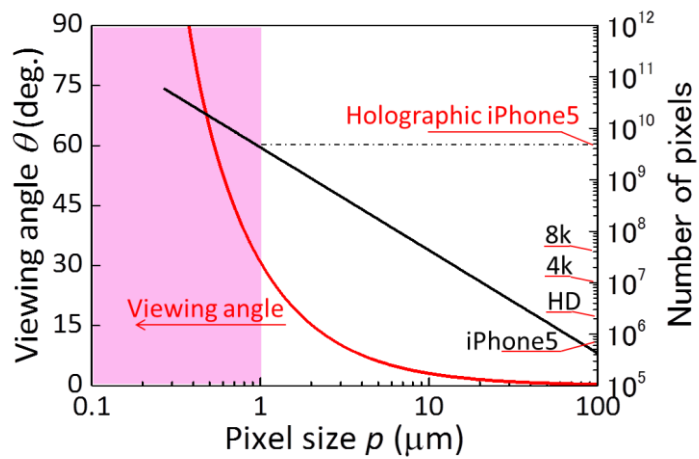


Fig. 1.3.2-1 Preliminary calculation results of relationship between pixel size, viewing angle, and number of pixels.

1.3.3 Holographic display with optical scanning

To visualize holograms on a large screen and wide viewing angle, SLMs with many pixels are required. One of the attractive approaches for solving the issue is using optical scanning. In this section, holographic displays with optical scanning and related technologies are discussed.

(1) Constitution of optical system

This approach uses a high-speed spatial light modulator, imaging optical system, scanning system, and a screen [6], [7]. The high-speed spatial light modulator can control a large amount of information per second, so the SLM can provide a hologram in which total resolution is larger than that of the SLM. One image on the SLM is a part of the original hologram and is transformed by the optical system to obtain desired viewing angle. Elementary holograms are scanned on the screen by a mechanical scanner. A high-speed SLM uses an acousto-optic modulator, digital micromirror, etc., whereas a mechanical scanner uses a Galvano mirror and a Polygon mirror. In some case, lenses or diffusers are used as the screen.

(2) Hologram for optical scanning

Holograms on a high speed SLM for optical scanning method with scanner are used resolution redistributed holograms with considering properties of optical imaging system. For reducing the resolution required for an SLM, many researchers of holographic display with optical addressing have adopted horizontal-parallax-only (HPO) holography [6]. HPO holography limits hologram parallax to only the horizontal direction, which is most the effective direction for perceiving 3D space. This method can reduce both the total resolution of holograms and the scanning axis of mechanical scanners for optical scanning. Holo-video, which was the first optical scanning type holographic display, was demonstrated to reconstruct a hologram in 1990 [7].

However, the optical system for this method tends to be large because it needs to transfer the hologram onto the screen. If the screen material were to be non-volatile and re-writable, an optical system without an imaging system can be chosen. This type of display is called “optical addressed spatial light modulator” [27].

1.4 Magneto-optic holographic three-dimensional display

A magneto-optic holographic three dimensional display is an optically addressable holographic display that uses a magnetic medium as a screen [8], [11]. The basic technologies are from magneto-optic spatial light modulators [9], [28]. This section introduces the basic technologies of the magneto-optic holographic three-dimensional display, and past results.

1.4.1 Magneto-optic effect

The magneto-optic (MO) effect is an interaction effect between light and magnetism [29]. The magnetic hologram, which is a type of hologram using the magneto-optic holographic three-dimensional display, is reconstructed by the MO effect. In this section, the MO effect, which is an optical rotation and circular dichroism due to magnetization, is described.

The MO Faraday effect is caused by a phase difference between the right and left circular polarization of transparent light in magnetic materials. Linear polarized light is split into right and left circular polarizations; this is shown in Fig. 1.4.1-1. In the magnetic material, these circular polarizations can propagate at different speeds and show phase differences. The transmitted or reflected light can then be rotated. The direction of rotation angle depends on the direction of magnetic field applied to the material.

Permittivity of the material relates to the MO effect. Permittivity of an isotropic material can be defined as follows.

$$\tilde{\epsilon} = \begin{pmatrix} \epsilon_{xx} & 0 & 0 \\ 0 & \epsilon_{xx} & 0 \\ 0 & 0 & \epsilon_{xx} \end{pmatrix} \quad (1.4.1-1)$$

For a magnetized material with uniaxial anisotropy, the permittivity tensor transforms into equation 1.4.1-2 (e.g., the z-axis is anisotropy axis).

$$\tilde{\epsilon} = \begin{pmatrix} \epsilon_{xx} & \epsilon_{xy} & 0 \\ -\epsilon_{xy} & \epsilon_{xx} & 0 \\ 0 & 0 & \epsilon_{zz} \end{pmatrix} \quad (1.4.1-2)$$

Off-diagonal components ϵ_{xy} dominate the optical activities of the material, so they cause a difference corresponding to the circular polarizations. The difference between the refractive indices ($N_+ = n_+ + ik_+$, $N_- = n_- + ik_-$) for each circular polarization can be described using ϵ_{xx} and ϵ_{xy} .

$$N_{\pm}^2 = \epsilon_{xx} \pm i\epsilon_{xy} \quad (1.4.1-3)$$

Difference between N_+ and N_- is not large. The following identities

$$\Delta n = n_+ - n_- \quad (1.4.1-4)$$

$$\Delta \kappa = \kappa_+ - \kappa_- \quad (1.4.1-5)$$

$$n = (n_+ + n_-)/2 \quad (1.4.1-6)$$

$$\kappa = (\kappa_+ + \kappa_-)/2 \quad (1.4.1-7)$$

can be used to write

$$\varepsilon_{xx}' = n^2 - \kappa^2 \quad (1.4.1-8)$$

$$\varepsilon_{xx}'' = 2n\kappa \quad (1.4.1-9)$$

$$\varepsilon_{xy}' = n\Delta\kappa + \kappa\Delta n \quad (1.4.1-10)$$

$$\varepsilon_{xy}'' = \kappa\Delta\kappa - n\Delta n \quad (1.4.1-11)$$

From equations 1.4.1-8~1.4.11, the relationship between Δn and $\Delta\kappa$ can be written as follows.

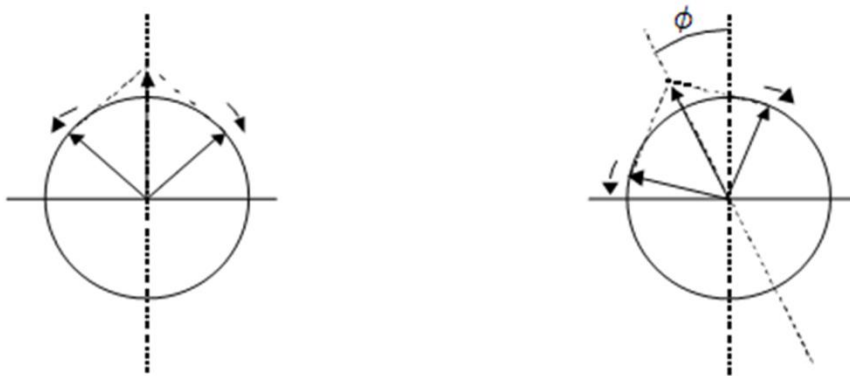


Fig. 1.4.1-1 Magneto-optic effect. (a) Linear polarization and split circular polarization in magnetic material. (b) Rotation of polarization.

$$\Delta n = \frac{\kappa \varepsilon_{xy}' - n \varepsilon_{xy}''}{n^2 + \kappa^2} \quad (1.4.1-12)$$

$$\Delta \kappa = \frac{n \varepsilon_{xy}' + \kappa \varepsilon_{xy}''}{n^2 + \kappa^2}. \quad (1.4.1-13)$$

The linear polarization transmitted to a film with thickness d and Faraday rotation angle θ_F can be described using Δn and $\Delta \kappa$, as follows.

$$\theta_F = -\frac{\omega \Delta n}{2c} d. \quad (1.4.1-14)$$

Faraday ellipticity η_F is given as the ratio of long and short axes of elliptic polarization

$$\eta_F = -\frac{\omega \Delta \kappa}{2c} d. \quad (1.4.1-15)$$

Equation 1.4.1-14 and 1.4.15 can be written as

$$\theta_F = -\frac{\omega d}{2c} \cdot \frac{\kappa \varepsilon_{xy}' - n \varepsilon_{xy}''}{n^2 + \kappa^2} \quad (1.4.1-16)$$

$$\eta_F = -\frac{\omega d}{2c} \cdot \frac{n \varepsilon_{xy}' + \kappa \varepsilon_{xy}''}{n^2 + \kappa^2}, \quad (1.4.1-17)$$

using the off-diagonal components of the permittivity tensor.

1.4.2 Magnetic hologram

Holograms, which are recorded fringes of magnetic information on magnetic media, are called “magnetic holograms”. In previous research, G. Fan’s group recorded magnetic holograms on MnBi film and reconstructed 2D page data from the hologram [30]. A magnetic hologram can be represented on the medium without using mechanical structures such as electrodes and pixels. Magnetic information can be rewritten with high switching speed. The magneto-optic holographic three-dimensional display adopts a magnetic hologram to represent holograms. This section deals with the recording and reconstruction of magnetic holograms.

(1) Recording of magnetic holograms

To record magnetic holograms, this project group used thermomagnetic recording with light addressing. The thermomagnetic recording stored information on an MO disk, which is a digital optical disc storage using the MO effect [31], [32]. Figure 1.4.2-1 shows the schematic image of the process of thermomagnetic recording. A magnetic medium is irradiated at a spot with perpendicular magnetization using a focused laser, and heated to a temperature greater than the Curie temperature. Magnetization in the heated spot is erased, and after cooling, reversed with external magnetic field.

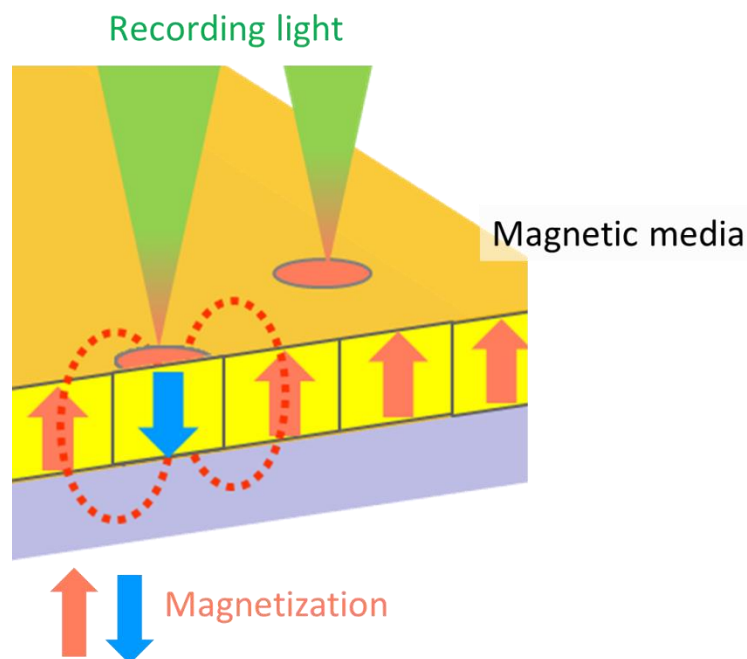


Fig. 1.4.2-1 Thermomagnetic recording with focused laser.

There are three ways of recording magnetic hologram fringes of 3D objects—using interference on magnetic medium, bit by bit recording, or using an imaging system such as a holographic display with optical scanning discussed in section 1.3.3. In the first method, holograms are recorded on a magnetic medium by interference of object light and reference light [33][16]. This is a basic method of recording a hologram on photosensitive media; however, a high-powered laser is required to record this magnetic hologram. The second method has been adopted for some fringe printers. It uses a focused laser and scanning system to record holograms, which are treated as electronic data [34]. Holograms with wide-viewing-angle require submicron scale pixels, so it takes a long time for recording. The third method uses recording light modulated by SLMs [35][36]. A part of the hologram is represented on the SLM and then transferred to a magnetic medium with pixel size reduction. This is similar to the second method, but it can have a higher recording speed, corresponding to the resolution of the SLM.

(2) Reconstruction of magnetic holograms [30], [37]

Figure 1.4.2-2 shows the schematic image of reconstruction of a magnetic hologram. Illumination monochromatic light with linear polarization is incident on the magnetic hologram,

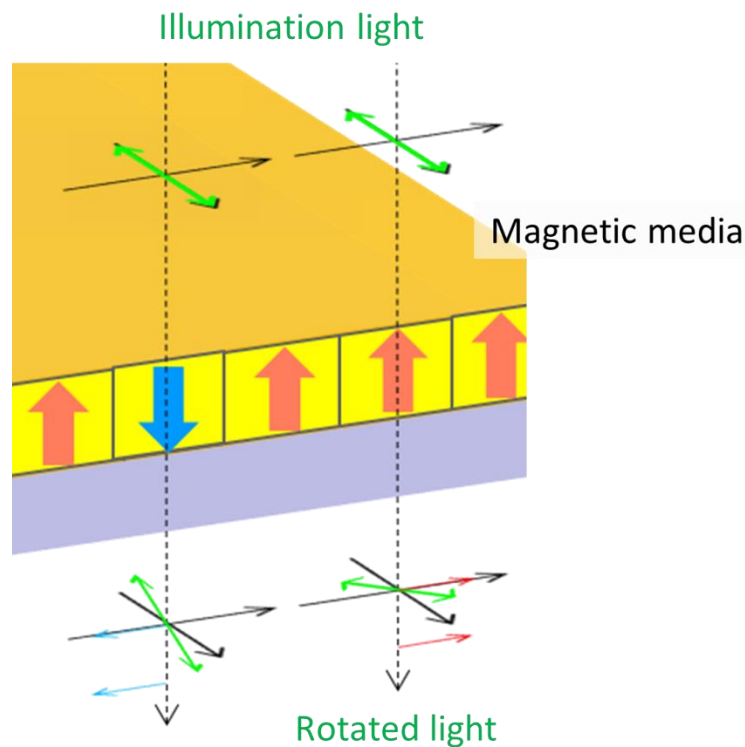


Fig. 1.4.2-2 Reconstruction of magnetic holograms. Blue and red arrows have a phase difference of π , and cause diffraction.

and is rotated by the MO Faraday effect. The rotation direction depends on the direction of magnetization of each pixel. Horizontal components of rotated light transmitted along each magnetization direction have a phase difference of 180° , and are diffracted. On the other hand, vertical components of transmitted light do not have a phase difference, so these components are not diffracted. The ratio of the horizontal to the vertical components depends on the Faraday rotation angle. An advantage of the magnetic hologram is that non-diffracted components can be cut or attenuated by a polarizer. A mathematical analysis of the reconstruction of magnetic holograms will be dealt with in Chapter 2.

1.4.3 Previous works of magneto-optic holographic three-dimensional display

This section describes the previous work that has been done to develop the magneto-optic holographic three-dimensional display. These results have acted as a proof of principle for magneto-optic holographic three-dimensional displays. They clarified basic properties of magnetic material with thermomagnetic recording as display media for optical addressed holographic displays. Some results of this section were published as a reference [8], [11].

(1) Magnetic medium with amorphous terbium iron

To evaluate magnetic pixel size fabricated optical addressing, amorphous Terbium Iron (*a*-TbFe) film, which is a popular material for research into thermomagnetic recording, was used as the magnetic medium as a proof of principle for the magneto-optic holographic three dimensional display [38]. The *a*-TbFe film shown below has these advantages. (1) A magnetic film that has a flat surface to decrease the scattering noise of reflected and diffracted light, (2) Amorphous MO thin films with perpendicular magnetic anisotropy for easy magnetization direction reversal over a submicron area, (3) A low Curie temperature for decreasing the heat-assisted laser power, and (4) A large MO rotation angle for high diffraction efficiency [37].

The *a*-TbFe films were fabricated by rf-magnetron sputtering and had an amorphous structure with perpendicular magnetic anisotropy (Fig. 1.4.3-1). The experimental samples had a structure that consisted of layers of SiO₂ substrate/SiN (20 nm)/*a*-TbFe (100 nm)/SiN (50 nm); this structure protected the *a*-TbFe layer from oxidation and provided a good magneto-optical response (the Kerr rotation was 1.1°, the Faraday rotation was 1.4°, the reflectivity was 10 %, and the transmittance was 0.8 % at 600 nm).

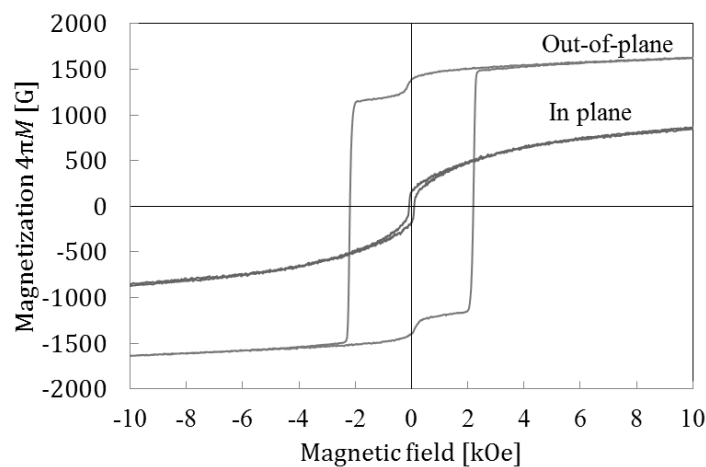


Fig. 1.4.3-1 Hysteresis loop of an amorphous TbFe film (*a*-TbFe). Thickness of the *a*-TbFe layer was 100 nm.

For writing the magnetic submicron pixel array, a laser system was fabricated with high-resolution lenses ($NA=0.5$), a pulse laser ($\lambda = 532$ nm, 10 ns/pulse), a 3-axis-positioning stage, and a laser focusing system (continuous wave laser at $\lambda = 633$ nm). The focused spot of the laser defined the magnetic pixel size. The theoretical diameter of a laser spot on the a -TbFe surface can be calculated by using

$$d = 1.2 \times \frac{\lambda}{NA}. \quad (1.4.3-1)$$

The diameter of the laser spot of this system was approximately 1.3 μm . A magnetic pixel was fabricated in a -TbFe with only a single laser pulse (10 ns/pulse). The smallest pixel array (256×256) was composed of 800 nm-wide magnetic domains, as shown in Fig. 1.4.3-2. The pixel size, as a function of the laser power, is shown in Fig 1.4.3-3.

In this result, the magnetic pixel size could be made smaller than the spot size of the laser because the laser intensity profile was Gaussian. To record a magnetic pixel, a single laser pulse with 10 ns pulse width was used, implying that the magnetic pixels could be driven with high speed. Magnetic pixels were constructed in a pixel array of 1 μm pitch, which is important to represent holograms with wide-viewing-angle. Fig 1.4.3-3 also shows that the magnetic pixel size could be modulated by changing laser pulse power. This result suggested that the minimum pixel size can be downsized by the laser power and optical system, and indicates a possibility for improving the expression of magnetic holograms.

The other important advantage of a magnetic hologram is that the ratio of diffracted light and 0th order reflected or transmitted light can be improved by a polarizer. Figure 1.4.3-4 shows the reflected light intensity and diffracted light intensity from the simple magnetic

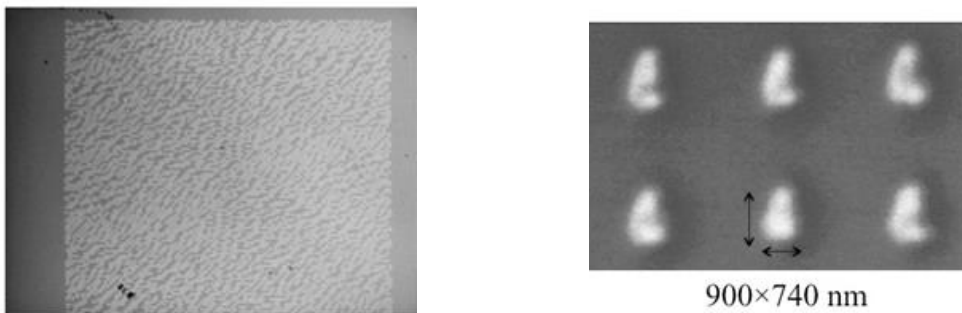


Fig. 1.4.3-2 Thermomagnetic recorded pixels on the a -TbFe. (a) Shows a fringe pattern with 1 μm pitch, 256×256 pixels, (b) Magnetic force microscope image of magnetic pixels with 2.5 μm pitch.

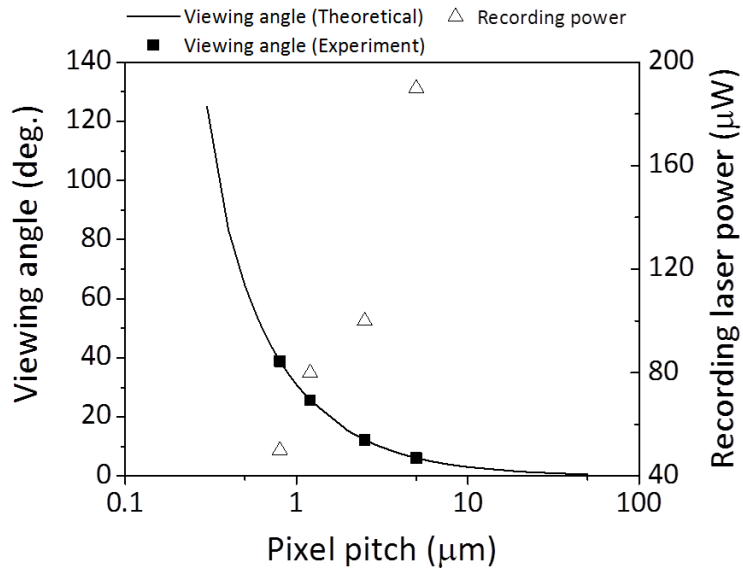


Fig. 1.4.3-3 Laser power dependence of pixel size and the viewing angle. Theoretical curve calculated using equation (1.3.2-1).

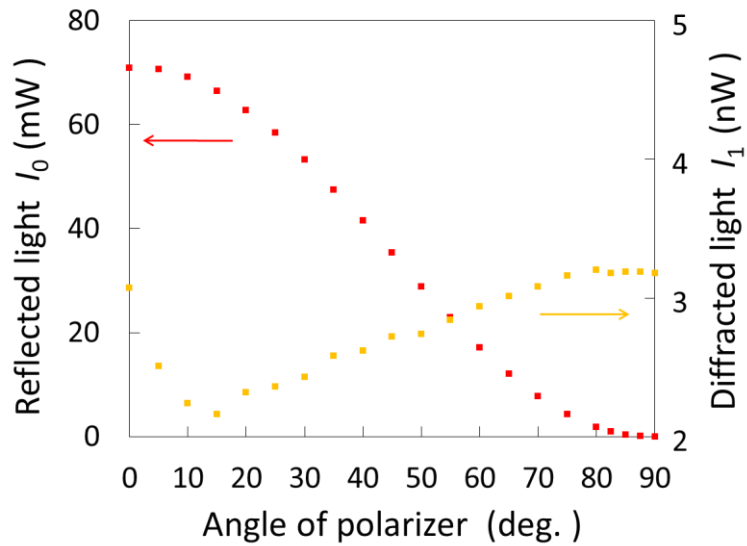


Fig. 1.4.3-4 Ratio of 1st order diffracted light and reflected light intensity of magnetic grating on the *a*-TbFe media.

grating on the *a*-TbFe film with rotating polarizer. The simple magnetic grating was recorded with 1 μm linewidth. The maximum ratio of the result achieved was up to 18 %, using polarizers with cross-Nicol placement.

(2) Computer generated hologram with half zone plate method

As proof of principle, a computer generated hologram (CGH) [39], [40] of a 3D object was produced, the details and principles of which will be dealt with in chapter 3. The 3D object used a wire frame cube, in which the length of a side was 3.74 mm, the length of a side of hologram-area on the magnetic media was approximately 14 mm, and the distance from the magnetic media was 20 mm. There were approximately 10000×10000 pixels in the hologram area, and the pixel size was 1.36 μm , which was minimum pixel size of the optical system. The generated hologram was binarized using the medium value of intensity distribution as a threshold to represent on *a*-TbFe.

(3) Optical system to record still images on magnetic medium

To represent an arbitrary magnetic hologram on the media, a tiling optical system was constructed. In this method, a part of the fringe image displays on DMDs and transfers the fringe pattern to magnetic film. This is the same approach taken by fringe printers or optical addressing spatial light modulators [27], [36], [41]. This method can enlarge the area of a holograms and increase the viewing angle by using the optical imaging system with demagnification.

The optical system with tiling optical addressing method was constructed using a pulsed laser, DMD, object lenses, x-y-z stage, and magnetic media (Fig 1.4.3-5). A DMD (Discovery 1100, $1024 \text{ pixels} \times 768 \text{ pixels}$, max driving speed is 22 kHz/frame) was used as an SLM to represent parts of holograms. For writing the hologram, a pulsed laser (pulse width: 10 ns, repetition frequency: 10 Hz, wavelength: 532 nm) was used to illuminate the DMD. A 2D hologram pattern image on the DMD was transferred to the magnetic film by two object lenses with one-tenth demagnification. The pixel size of DMD was 13.6 μm , and the magnetic pixel size was 1.36 μm . The viewing angle of the 3D images was approximately 23° in the case of 532 nm illumination light wavelength.

Figure 1.4.3-6 shows the mesh pattern of magnetic pixels produced on magnetic media when using the tiling optical addressing method. The mesh width was 136 μm on the DMD that was formed with 10×10 pixels. Figure 1.4.3-6 (b) shows a recorded magnetic pixel array on the *a*-TbFe media. The hologram pattern on DMD was downsized to one-tenth and transferred to the magnetic film, and 13.6 μm of pixel size of DMD was reduced to 1.4 μm on the magnetic pixels. Figure 1.4.3-7 (a) shows a part of the hologram pattern that was displayed on the DMD.

This pattern was also transferred onto the α -TbFe film with downsizing (Fig.1.4.3-7 (b)). The 2D hologram pattern displayed on the DMD was accurately transferred reducing size on magnetic film.

Figure 1.4.3-8 shows the reconstructed holographic 3D image from the α -TbFe. The media was placed within two polarizers with cross-Nicol placement, and was incident with light from a CW laser (wavelength 532 nm). The 3D image could be reconstructed from a transferred 2D hologram pattern when a reference light illuminated the magnetic pixel array. The reconstructed images showed the same pattern as that designed by computer. These results show that a magnetic hologram with optical addressing can represent arbitrary 3D images.

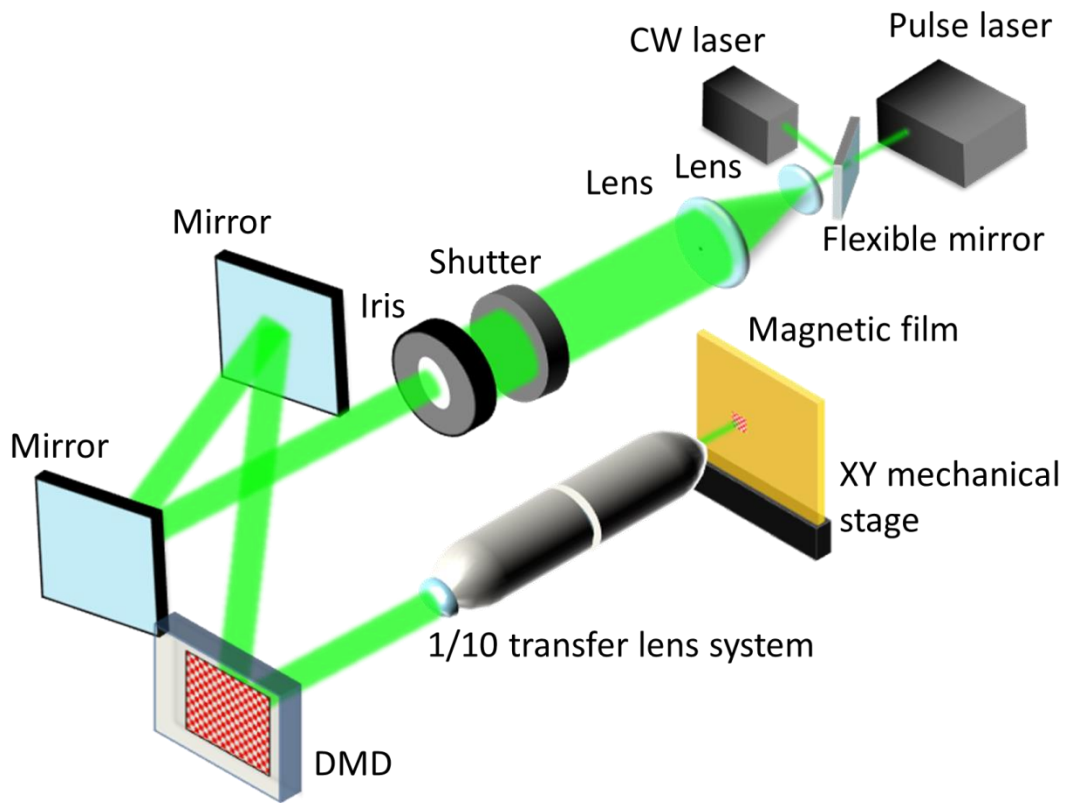
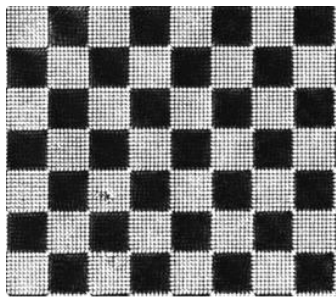
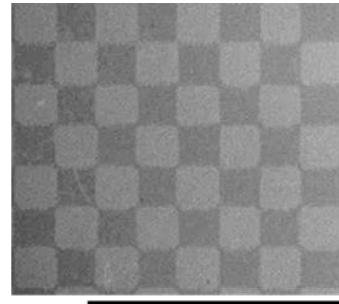


Fig. 1.4.3-5 Schematic image of constructed tiling optical system. 1/10 transfer lens system was constructed with two objective lenses with focal lengths of 100 mm and 10 mm. A CW laser was used to align the optical system.



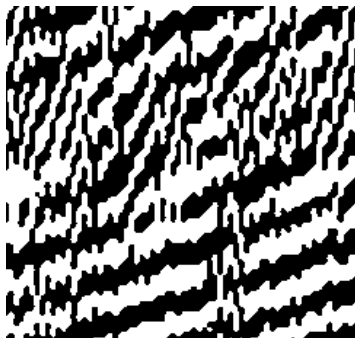
(a)



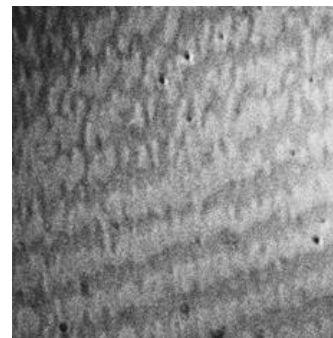
100 μm

(b)

Fig. 1.4.3-6 Mesh pattern of magnetic pixels. (a) Hologram pattern on the DMD, and (b) Magnetic pixel pattern on magnetic media.

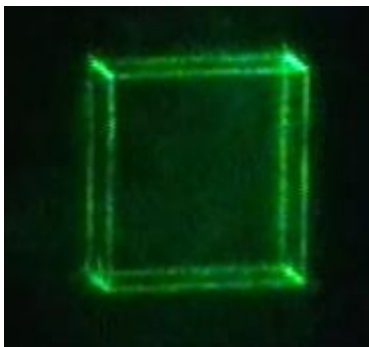


(a)

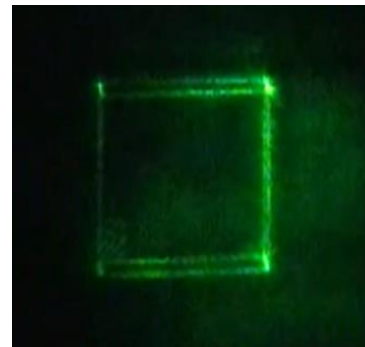


(b)

Fig. 1.4.3-7 A fringe pattern of 3D-object. (a) A part of hologram image on the DMD, (b) Magnetic pixel image at the same location as (a).



(a)



(b)

Fig. 1.4.3-8 Reconstruction image of 3D object. (a) Viewing angle was 5° left side, and (b) Viewing angle was 0° .

1.5 Outline of the research

This research is for development of the magneto-optic holographic three-dimensional display, which is an optically addressed type of holographic display. Holographic displays can reconstruct realistic 3D images without the need for the viewer to wear special glasses. Factors in the reconstructed image can satisfy physiological requirements for recognizing 3D spaces. However, holographic displays are difficult to build as they require submicron scale pixels for reconstructing 3D images with a wide viewing angle. Magneto-optic holographic three-dimensional displays are expected to solve this problem by using magnetic media, which is excellent in recording speed and recording density. The magnetic medium used in the first magneto-optic holographic three-dimensional display was an amorphous $Tb_{22}Fe_{78}$ (*a*-TbFe) film, and it reconstructed a still 3D image with wide-viewing angle. However, recording speed was too slow to apply to video. In addition, the reconstructed image from the *a*-TbFe film had low brightness.

The purpose of this research is the investigation of elemental technologies for magneto-optic holographic three-dimensional display to represent holographic video with clear images.

Chapter 2 discusses the improvement of light efficiency of magnetic media. To use magnetic media for holographic display, light efficiencies of recording and reconstruction of hologram were regarded as a problem, and these efficiencies are dominated by the material of the media. To improve recording and reconstruction light efficiencies, magnetic media with artificial magnetic lattice was adopted. They can control optical or magneto-optical behavior of the media by structure.

Chapter 3 discusses calculation methods of computer generated holograms for magnetic hologram. To compute a complex object and its surface, a two-dimensional image based method was adopted. Reconstructed images with binary holograms included binarization errors. To reduce noise, a new calculation method with pixel position was proposed for magnetic holograms that were not fixed mechanically.

Chapter 4 discusses the optical system for holographic video system, and demonstrates a holographic video on magnetic medium with narrow viewing angle. To demonstrate holographic video, synchronization of recording and erasure systems were constructed, and the optical system demonstrated continuous recording and reconstruction of holographic video. In addition, the new hologram recording system used micro lens array matching to DMD pixels to reduce scanning length.

Chapter 5 discusses the improvement method for image quality. In previous chapters, the magneto-optic holographic three-dimensional display was developed to represent holographic video with monochrome and monotone. However, to put it into practical use,

colorization and multilevel gradations of reconstruction images are important. As proof of principle for colorization, the optical space division method was adopted. By using thickness designed BiDyYFeAlG films, the synthesized reconstructed image covered standard RGB color region, and included white.

The Faraday rotation angle, which depends on recording depth and could be controlled via recording laser power, was used to represent a gray level hologram. The relationship between Faraday rotation angle of recorded pixel and recording energy was discussed.

References

- [1] M. Kanazawa, K. Hamada, I. Kondoh, F. Okano, Y. Haino, M. Sato, and K. Doi, “An ultrahigh-definition display using the pixel-offset method,” *J. Soc. Inf. Disp.*, vol. 12, no. 1, p. 93, 2004.
- [2] M. Emoto and M. Sugawara, “Viewers’ optimization of preferred viewing distance by spatial resolution of TV display,” *Displays*, vol. 45, pp. 1–5, 2016.
- [3] V. M. Bove, “Display Holography’s Digital Second Act,” *Proc. IEEE*, vol. 100, no. 4, pp. 918–928, Apr. 2012.
- [4] S. Reichelt, R. Haussler, G. Fütterer, and N. Leister, “Depth cues in human visual perception and their realization in 3D displays,” *Three Dimens. Imaging, Vis. Disp. 2010*, vol. 7690, no. 0, p. 76900B–76900B–12, 2010.
- [5] T. Kozacki, G. Finke, P. Garbat, W. Zaperty, and M. Kujawińska, “Wide angle holographic display system with spatiotemporal multiplexing.,” *Opt. Express*, vol. 20, no. 25, pp. 27473–81, 2012.
- [6] Y. Takaki and N. Okada, “Hologram generation by horizontal scanning of a high-speed spatial light modulator,” *Appl. Opt.*, vol. 48, no. 17, p. 3255, 2009.
- [7] P. St. Hilaire, S. A. Benton, and M. Lucente, “Synthetic aperture holography: a novel approach to three-dimensional displays,” *J. Opt. Soc. Am. A*, vol. 9, no. 11, p. 1969, 1992.
- [8] H. Takagi, K. Nakamura, T. Goto, P. B. Lim, and M. Inoue, “Magneto-optic spatial light modulator with submicron-size magnetic pixels for wide-viewing-angle holographic displays.,” *Opt. Lett.*, vol. 39, no. 11, pp. 3344–7, 2014.
- [9] J. H. Park, H. Takagi, K. Nishimura, H. Uchida, M. Inoue, J. H. Park, and J. K. Cho, “Magneto-optic spatial light modulators driven by an electric field,” *J. Appl. Phys.*, vol. 93, no. 10 3, pp. 8525–8527, 2003.
- [10] J. H. Park, H. Takagi, J. K. Cho, K. Nishimura, H. Uchida, and M. Inoue, “Magneto-optic spatial light modulator with one-step pattern growth on ion-milled substrates by liquid-phase epitaxy,” *IEEE Trans. Magn.*, vol. 40, no. 4 II, pp. 3045–3047, 2004.
- [11] H. Takagi, K. Nakamura, S. Tsuda, T. Goto, P. Boey Lim, and M. Inoue, “Magneto-optic Three-Dimensional Holographic Display with Tiling Optical Addressing Method,” *Sensors Mater.*, vol. 27, no. 10, pp. 1003–1008, 2015.
- [12] S. A. Benton and V. M. Bove, *Holographic Imaging*. 2008.
- [13] C. Wheatstone, “Contributions to the Physiology of Vision. Part the First. On Some Remarkable, and Hitherto Unobserved, Phenomena of Binocular Vision,” *Philos. Trans. R. Soc. London*, vol. 128, no. 0, pp. 371–394, 1838.
- [14] G. Lippmann, “Épreuves Réversibles Donnant la Sensation du Relief,” *J. Phys.*

- Théorique Appliquée*, vol. 7, no. 1, pp. 821–825, 1908.
- [15] D. Gabor, “A New Microscopic Principle,” *Nature*, vol. 161, no. 4098, pp. 777–778, May 1948.
- [16] E. N. Leith and J. Upatnieks, “Reconstructed Wavefronts and Communication Theory,” *J. Opt. Soc. Am.*, vol. 52, no. 10, p. 1123, 1962.
- [17] E. N. Leith and J. Upatnieks, “Wavefront Reconstruction with Diffused Illumination and Three-Dimensional Objects,” *J. Opt. Soc. Am.*, vol. 54, no. 11, pp. 1295–1301, 1964.
- [18] E. N. Leith and J. Upatnieks, “Wavefront Reconstruction with Continuous-Tone Objects,” *J. Opt. Soc. Am.*, vol. 53, no. 12, pp. 1377–1381, 1963.
- [19] S. A. Benton, “Rainbow holograms,” *Opt. Photonics News*, vol. 2, no. 7, p. 50, Jul. 1991.
- [20] Y. Nakamura, H. Takagi, P. B. Lim, and M. Inoue, “Magnetic volumetric hologram memory with magnetic garnet,” *Opt. Express*, vol. 22, no. 13, pp. 16439–16444, 2014.
- [21] H. Horimai, X. Tan, and J. Li, “Collinear holography,” *Appl. Opt.*, vol. 44, no. 13, p. 2575, May 2005.
- [22] H. Horimai and D. Horimai, “Full-Color 3D Display System with 360 Degree Horizontal Viewing Angle,” *Proc. Int. Symp. 3D Contents*, pp. 7–10, 2010.
- [23] D. H. Close, “Holographic Optical Elements,” *Optical Engineering*, vol. 14, no. 5, pp. 1–21, 1975.
- [24] L. Onural, F. Yaras, and H. Kang, “Digital holographic three-dimensional video displays,” *Proc. IEEE*, vol. 99, no. 4, pp. 576–589, 2011.
- [25] L. Onural, “Television in 3-D: What are the prospects?,” *Proc. IEEE*, vol. 95, no. 6, pp. 1143–1145, 2007.
- [26] L. H. Enloe, J. A. Murphy, and C. B. Rubinstein, “Hologram Transmission via Television,” *Bell Syst. Tech. J.*, vol. 45, no. 2, pp. 335–339, Feb. 1966.
- [27] G. Moddel, K. M. Johnson, W. Li, R. A. Rice, L. A. Pagano-Stauffer, and M. A. Handschy, “High-speed binary optically addressed spatial light modulator,” *Appl. Phys. Lett.*, vol. 55, no. 6, pp. 537–539, 1989.
- [28] H. Takagi, P. Boey Lim, M. Inoue, and H. Umezawa, “Solid-State Spatial Light Modulator with Magneto-Optical Effect,” *Rev. Laser Eng.*, vol. 38, no. 5, pp. 356–362, 2010.
- [29] 佐藤勝昭, “光と磁気”, 朝倉書店. 2007. (in Japanese.)
- [30] G. Fan, “Magneto-Optic Hologram,” *J. Appl. Phys.*, vol. 40, no. 3, p. 974, 1969.
- [31] M. Kenny, I. Z. Rahman, M. A. Rahman, B. Bechevet, J. Mouchot, and J. Daval, “Thermomagnetic recording properties of novel bismuth-substituted garnet films,” *J. Magn. Magn. Mater.*, vol. 120, no. 1–3, pp. 265–267, Mar. 1993.

- [32] Y. Nakamura, H. Takagi, P. B. Lim, and M. Inoue, "Effect of recording condition on the diffraction efficiency of magnetic hologram with magnetic garnet films," *J. Appl. Phys.*, vol. 116, no. 10, 2014.
- [33] H. Horimai, A. Inoue, T. Miyama, T. Fujii, S. Suzuki, R. Kusaka, and T. Tokushima, "High-Density Information Storage by Means of Magnetic Holography on Amorphous TbFe Thin Films," *J. Magn. Soc. Japan*, vol. 8, no. 2, pp. 109–112, 1984.
- [34] K. Matsushima, S. Kobayashi, and H. Miyauchi, "A high-resolution fringe printer for studying synthetic holograms," *Proc. SPIE*, vol. 354, pp. 347–354, 2006.
- [35] Y. Kim, E. Stoykova, H. Kang, S. Hong, J. Park, J. Park, and J. Hong, "Seamless full color holographic printing method based on spatial partitioning of SLM," *Opt. Express*, vol. 23, no. 1, pp. 172–182, 2015.
- [36] M. Stanley, R. W. Bannister, C. D. Cameron, S. D. Coomber, I. Cresswell, J. R. Hughes, P. Jackson, K. Milham, R. Miller, D. A. Payne, D. C. Scattergood, A. Smith, M. A. Smith, P. Watson, P. Webber, and C. W. Slinger, "100 Mega-Pixel Computer Generated Holographic Images From Active Tiling(Tm)---a Dynamic and Scalable Electro-Optic Modulator System," *Proc. SPIE, Pract. Hologr. XVII Hologr. Mater. IX*, vol. 5005, pp. 247–258, 2003.
- [37] H. Haskal, "Polarization and efficiency in magnetic holography," *IEEE Trans. Magn.*, vol. 6, no. 3, pp. 542–545, Sep. 1970.
- [38] S. K. Lee and S. G. Kim, "Domain formation characteristics during thermomagnetic recording for amorphous TbFe and TbFeCo alloy thin films," *IEEE Trans. Magn.*, vol. 25, no. 5, pp. 4039–4041, 1989.
- [39] T. Mishina, F. Okano, and I. Yuyama, "Time-alternating method based on single-sideband holography with half-zone-plate processing for the enlargement of viewing zones.," *Appl. Opt.*, vol. 38, no. 17, pp. 3703–3713, 1999.
- [40] O. Bryngdahl and A. Lohmann, "Single-Sideband Holography*," *J. Opt. Soc. Am.*, vol. 58, no. 5, p. 620, 1968.
- [41] H. Yoshikawa and T. Yamaguchi, "Computer-generated holograms for 3D display," *Chinese Opt. Lett.*, vol. 7, no. 12, pp. 1079–1082, 2009.

2. Magnetic holographic medium with artificial magnetic lattice

2.1 Introduction

Some inherent characteristics of a magnetic hologram are appropriate for use as screen material in optically addressed holographic displays; magnetic domains can be controlled with laser light, switching speed is faster than microsecond order [1], and they are stable to frequent recording and erasure. On the other hand, recording energy and the brightness of reconstructed images have some issues, which are caused by thermomagnetic recording with light absorption [2]–[8]. Therefore, to adopt magnetic materials for an optically addressed holographic display, it is important to consider the light absorption of BiDyYFeAlG.

Since the 1990s, Inoue *et. al.* have theoretically and experimentally demonstrated the enhancement of the magneto-optic (MO) effect (Faraday rotation angle) at the localized mode within the stop band, with the sample of the micro-cavity of magnetophotonic crystals (MPCs) [9]–[12]. A lot of research has shown that the apparent magneto-optical and optical properties of magnetic materials can be controlled or changed by their structures.

In this chapter, two magnetic materials with different light absorption property were adopted as holographic media; the high-light-absorption material was amorphous terbium iron (*a*-TbFe), while the low-light-absorption material was bismuth, dysprosium, and aluminum substituted yttrium iron garnet (BiDyYFeAlG). In addition, nanometer-scaled periodic structures, such as MPCs, were also examined and applied to magnetic holographic media. These structures, which can control magneto-optical and optical behaviors, are called artificial magnetic lattice. Including the above materials and structures, magnetic media for magneto-optic holographic three-dimensional display were evaluated comprehensively, focusing especially on light efficiency for the recording and reconstruction of magnetic holograms.

Section 2.2 introduces the holographic media properties that are required; basic properties for magnetic holographic media, theoretical diffraction efficiency of magnetic holograms, and the mathematically calculated method for the brightness of reconstructed images. Section 2.3 introduces MPC and the structural dependency of diffraction efficiency. To improve the brightness of reconstructed images, BiDyYFeAlG was adopted. Magnetic garnet with artificial magnetic lattice structure has been dealt with in section 2.4. Finally, *a*-TbFe/BiDyAl:YIG multi layered media was proposed in section 2.5.

2.2 Background of magnetic media

2.2.1 Basic requests for magnetic material

For hologram reconstruction, optical and magneto-optical properties are important for reconstructing clear, bright, and noise-less three dimensional (3D) images. On the other hand, on erasure and recording of magnetic holograms, magnetic properties are important. Magnetic holograms have the following requirements of hologram media.

(1) Large magneto-optic (MO) effect

The diffraction on magnetic holograms is caused by the MO effect. Magnetic material with large MO rotation angle is required.

(2) High reflectance or transmittance

When magnetic hologram is illuminated by laser light, light absorption is a loss for the reconstruction of holograms.

(3) Flatness and homogeneity

To suppress scattering noise and undesired interference, hologram media is preferably flat and homogenous.

(4) Appropriate Curie temperature

Magnetization of the media should be done by erasure with incident laser light. The magnetic information should be storable at room temperature.

(5) Small coercivity

For optically addressed holographic displays, the magnetic information should be erasable with a small magnetic field.

(6) Thermal properties

Thermal diffusion in magnetic layer causes reduction of diffraction efficiency and slowing of the switch speed.

2.2.2 Diffraction efficiency of magnetic hologram

The diffraction efficiency of a magnetic hologram, which is defined as the ratio of diffracted light intensity to illumination light intensity, can be written as

$$\eta = \frac{I_1}{I_{in}}. \quad (2.2.2-1)$$

Where η is the diffraction efficiency, I_1 is the first order transmitted light, and I_{in} is the illuminated light. There have been many theoretical analyses of diffraction efficiency of magnetic holograms [13]–[15]. To describe the diffraction efficiency of magnetic hologram and their important factors, a simple magnetic grating is assumed; grating pitch is r and the ratio of up and down magnetized domain areas is s/r (Fig 2.2.2-1). x polarized light is incident on the grating. Then, the light transmitted from the grating has polarization rotation through the MO effect, and is attenuated with light absorption. Transmittance functions of the grating for each polarization direction can be written as

$$\tau_y(y) = p(y) \exp\left(\frac{-\alpha t}{2}\right) \sin \theta_F t \quad (2.2.2-2(a))$$

$$\tau_x(x) = \exp\left(\frac{-\alpha t}{2}\right) \cos \theta_F t. \quad (2.2.2-2(b))$$

Where α is the absorption index of magnetic films, t is the thickness of film, θ_F is the specific Faraday rotation angle in $^\circ/\mu\text{m}$, $p(y)$ is a periodic function meaning the direction of magnetization at position y defined for $nr \leq x \leq (n+1)r$, and n is an integer,

$$p(y) = \text{sgn}\left\{\left[y - \left(nr + \frac{s}{2}\right)\right]\left[y - \left([n+1]r - \frac{s}{2}\right)\right]\right\} \quad (2.2.2-3)$$

$$\text{sgn}(t) = \begin{cases} 1 & (t \geq 0) \\ -1 & (t < 0) \end{cases}$$

According to equation (2.2.2-2 (b)), the x component is not diffracted by the magnetic grating, because the transmittance function for the x component has no dependence on magnetization distribution. On the other hand, the y component depends on position y , and is diffracted by the magnetic grating. The transmittance function for y components can be expanded in a Fourier series as follows

$$\tau_y(y) = \exp\left(\frac{-\alpha t}{2}\right) \sin \theta_F t \left[\frac{2s-r}{r} + \frac{4}{\pi} \sum_{m=1}^{\infty} \frac{1}{m} \sin \frac{\pi m s}{r} \cos \frac{2\pi m y}{r} \right]. \quad (2.2.2-4)$$

From equation (2.2.2-4), light intensities of 1st order diffracted light I_1 and 0th order diffracted light intensity I_0 can be written using illuminated light intensity I_{in}

$$I_0 = I_{in} \left(\frac{2s-r}{r}\right)^2 \exp(-\alpha t) \sin^2 \theta_F t \quad (2.2.2-5)$$

$$I_1 = I_{in} \frac{4}{\pi^2} \exp(-\alpha t) \sin^2 \frac{\pi s}{r} \sin^2 \theta_F t. \quad (2.2.2-6)$$

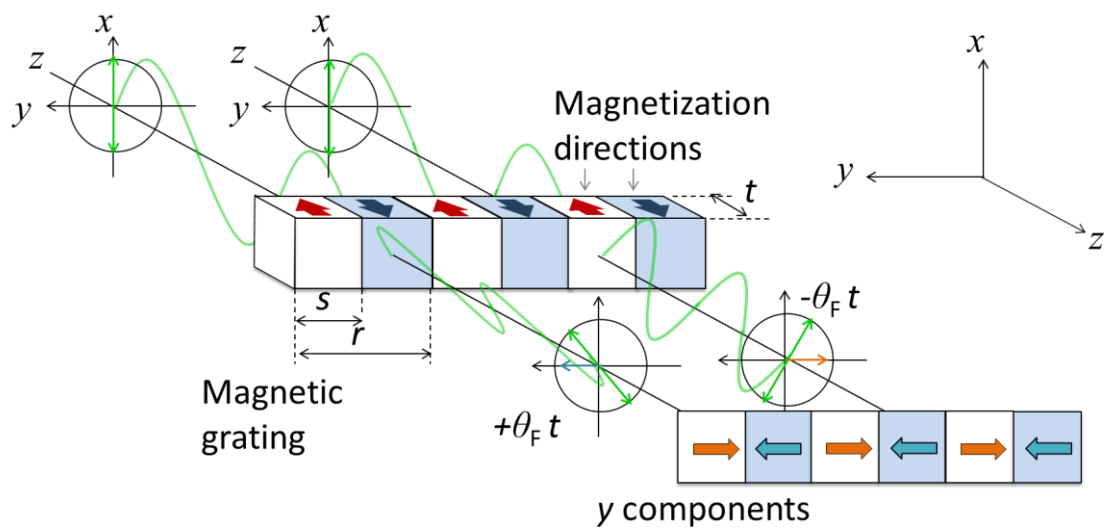


Fig. 2.2.2-1 Schematic diagram of a simple magnetic grating.

From these results, the equation (2.2.2-1) can be changed to

$$\eta = \frac{I_1}{I_{in}} = \frac{4}{\pi^2} \exp(-\alpha t) \sin^2 \frac{\pi s}{r} \sin^2 \theta_F t. \quad (2.2.2-7)$$

According to this equation, diffraction efficiency depends on the thickness of the magnetic medium and has a trade-off between the transmissivity ($\exp(-\alpha t)$) and the Faraday rotation angle ($\theta_F t$).

2.2.3 Illumination light power required for reconstructing hologram

Display standard ISO13406 for liquid crystal displays recommends the brightness of displays to be over 100 cd/m². To evaluate the brightness of reconstructed images on magnetic material, the brightness (unit: cd/m²) is transformed to light power density (unit: W/cm²), and the brightness is estimated from the light power density. From the relationship between candela (unit of brightness) and lumen (unit of light flux), equation 2.2.3-1 can be derived for green light with wavelength of 555 nm.

$$1 \text{ [W]} = 683 \text{ [lm]}. \quad (2.2.3-1)$$

Equation 2.2.3-1 is from the human perception that 683 lm most corresponds to a light source with 1 W, 555 nm, under bright conditions. Light flux L [lm], brightness C [cd], and half apex angle θ of circular cone of solid angle has a relationship as follows.

$$L \text{ [lm]} = 2\pi(1 - \cos\theta)[\text{sr}] \cdot C \text{ [cd]}. \quad (2.2.3-2)$$

From equation 2.2.3-1 and 2.2.3-2, the relationship between the brightness C per unit area and the light power density W is can be explained as,

$$W \text{ [W/m}^2\text{]} = \frac{2\pi}{683} (1 - \cos\theta) \cdot C \text{ [cd/m}^2\text{]}. \quad (2.2.3-3)$$

Then the diffracted light intensity of 3D images is W and the hologram can reconstruct 3D images with a brightness C cd/m². Figure 2.2.3-1 shows the required light power densities to reconstruct 3D images with 100 cd/m² against viewing angle. In this calculation, viewing angle is assumed with full-parallax, and then θ in the equation 2.2.3-3 is half the viewing angle.

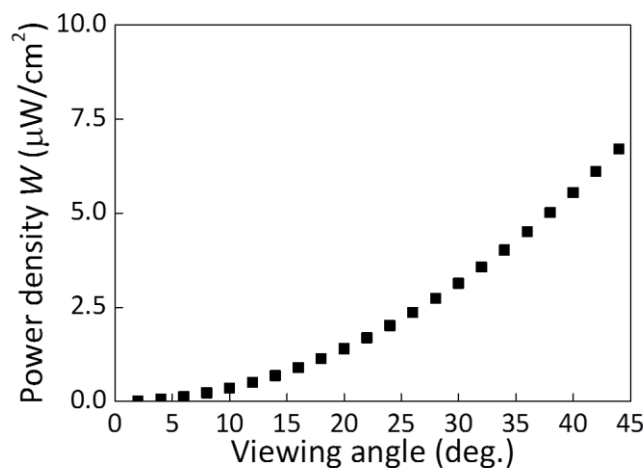


Fig. 2.2.3-1 Required power density to reconstruct 3D images with 100 cd/m².

2.3 Controlling magneto-optical property with artificial magnetic lattice

In section 2.2, the relationship between diffraction efficiency and MO property was described. For obtaining high diffraction efficiency, a large specific MO rotation angle and a small light absorption were important. On the other hand, the light energy density required to record the hologram was predicted to increase with reducing light absorption of magnetic film, because light absorbed by unit volume dominates volumetric heating temperature.

Focus was turned to artificial magnetic lattice structures, which can control the optical and magneto-optical properties of magnetic material by the structures, to solve this tradeoff. This section provides an overview of one of the typical artificial magnetic lattice structures, magnetophotonic crystals (MPCs).

2.3.1 Magnetophotonic crystals

MPCs are artificial periodic structures with defect layers. There are one-dimensional, two-dimensional, and three-dimensional MPCs. This section deals with one-dimensional MPCs. Theoretical predictions about the existence of the enhancement of Faraday rotation in the microcavity structure composed of two dielectric Bragg reflectors and a Bi:YIG defect layer incorporated between them— $(\text{Ta}_2\text{O}_5/\text{SiO}_2)^5/\text{Bi:YIG}/(\text{SiO}_2/\text{Ta}_2\text{O}_5)^5$ —were experimentally confirmed [16], [17]. Figure 2.3.1-1 shows a representative of one-dimensional MPC [10], and Fig. 2.3.1-2 shows a spectra of the transparent mode of this MPC at normal incidence. In the localized mode for the photonic bandgap, the Faraday rotation angle was increased to 10 times that of the Bi:YIG single-layered film.

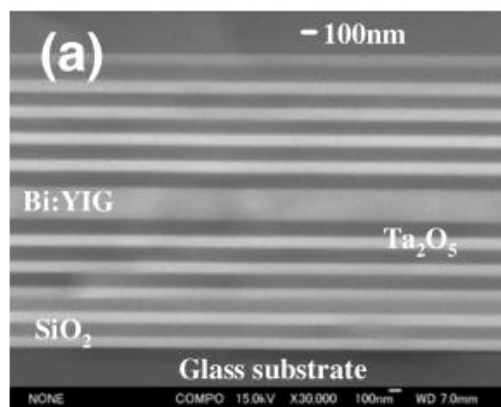


Fig. 2.3.1-1 Cross-sectional SEM images of the one-dimensional MPC. The structure is $(\text{Ta}_2\text{O}_5/\text{SiO}_2)^5/\text{Bi:YIG}/(\text{SiO}_2/\text{Ta}_2\text{O}_5)^5$. [10]

This result has important implications for the application of MPCs to magnetic hologram media. Enhancement of the MO effect directly improves diffraction efficiency. In addition, the problem of collapse of interference fringes caused by thermal diffusion inside magnetic media can be expected to be solved [5]. This problem arises from the thermal distribution along the direction of thickness, i.e., the influence can be expected to reduce by making the media thinner.

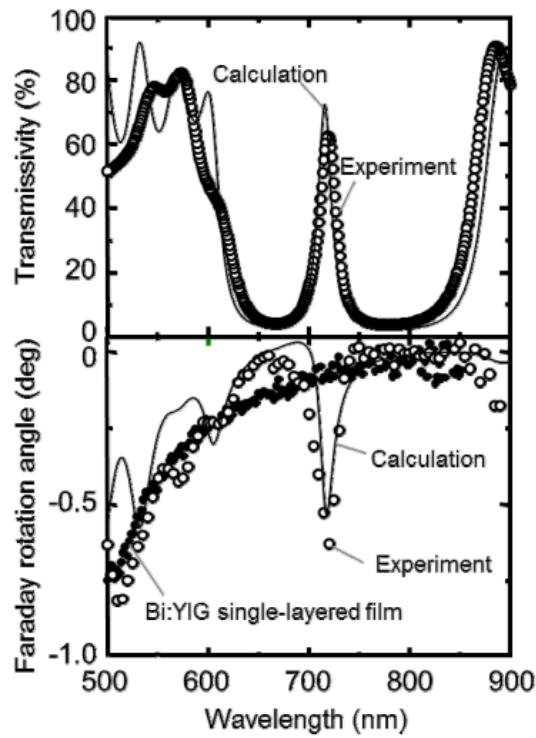


Fig. 2.3.1-2 Spectra of the MPC; transmittance is at the top, and MO Faraday rotation angle is at the bottom. [10]

2.3.2 Numerical calculation for designing media structure

For the application of MPC as magnetic hologram media, MPC structures and their diffraction efficiencies were simulated by finite element method (COMSOL Multiphysics 4.3a). Fig.2.3.2 shows a simulation model. The yellow region was composed of MPCs with BiDyYFeAlG, and their region was magnetized in the down direction. A simple magnetic grating pattern with a line width of $1.36\ \mu\text{m}$ was set up on the BiDyYFeAlG layer. The 1st order diffracted light intensity was evaluated when the magnetic grating diffracted normal incident illumination light. To evaluate performance of MPCs, the defect layer thickness d and number of dielectric mirror pairs n of MPC were changed, then the diffraction efficiency corresponding to each structure was calculated from reference light intensity and diffracted light intensity. $N = 0$ was a monolayer BiDyYFeAlG film. Table.2.3.2-1 shows the parameters of materials for the simulation.

Figure 2.3.2-1 shows the calculation results of diffraction efficiencies for each structure. All structures show saturation with increasing BiDyYFeAlG layer thickness. The saturation of diffraction efficiency was caused by balance of transmittance and Faraday rotation angle. Equation 2.2.2-6 implies this saturation. Figure 2.3.2-2 and 2.3.2-3 also supports this result. On the other hand, the film thickness at which saturation occurs decreased with increasing number of DM pairs n . The results could be considered for transmittance reduction.

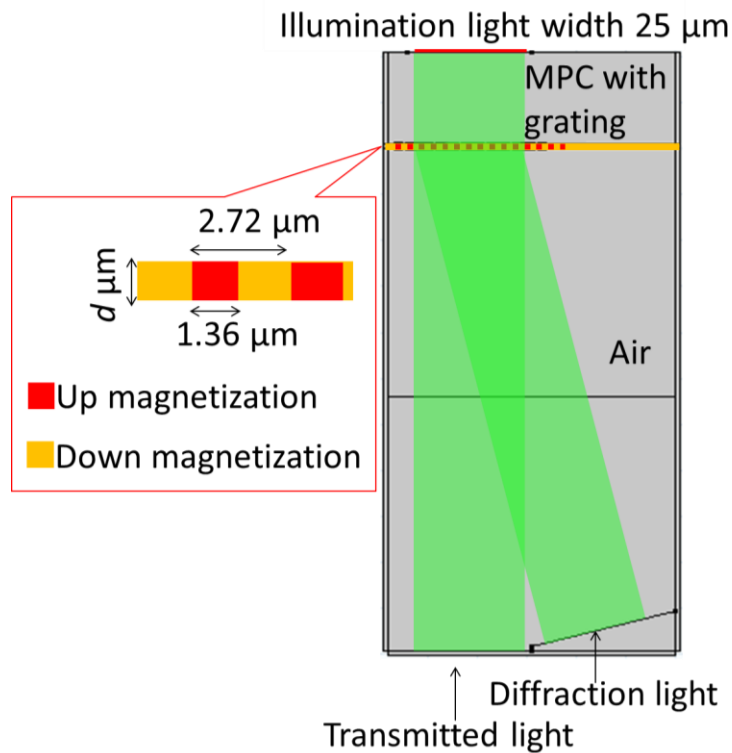


Fig. 2.3.2-1 Schematic image of simulation model to calculate MPC performance for magnetic hologram.

Table 2.3.2-1 Material parameters in the matrix approach. ^a

Material	N	κ	θ_F ($^\circ/\mu\text{m}$)
BiDyYFeAlG	2.27	0.0186	2.13
SiO ₂	1.45	0	-
Ta ₂ O ₅	2.16	0	-
Air	1.00	0	-

^aRefractive index n , extinction coefficient κ , and specific Faraday rotation angle θ_F .

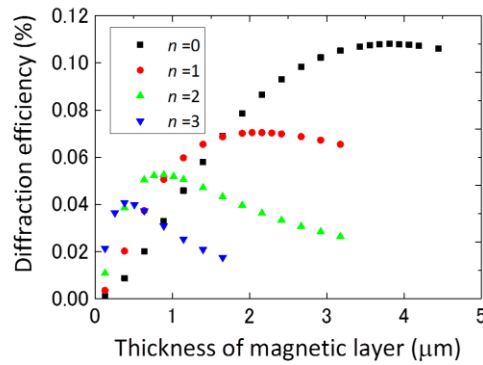


Fig. 2.3.2-2 Simulated diffraction efficiency of each structure, n is the number of DM pairs.

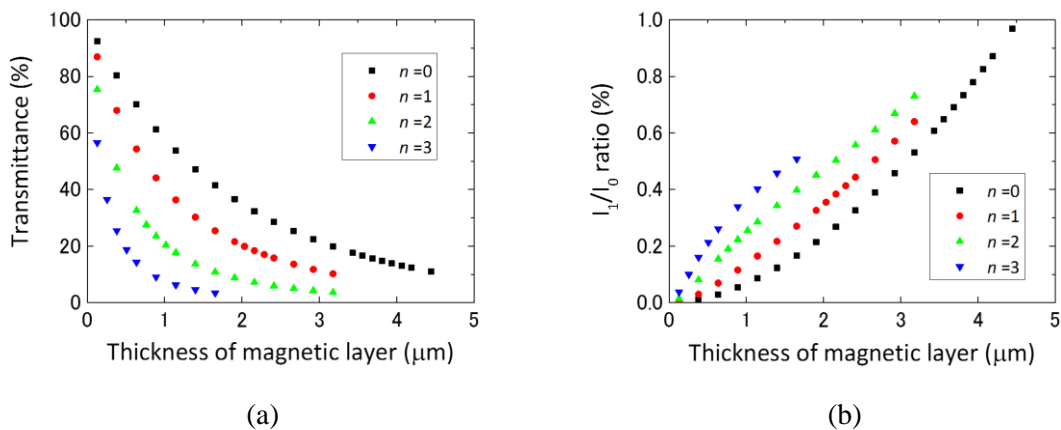


Fig. 2.3.2-3 Optical and magneto-optical properties of MPCs.
 (a) Transmittance reduced with increasing number of DM pair n . (b) I_V/I_0 ratios were increased with increasing film thickness and n , the ratio depends on the Faraday rotation angle.

2.4 Development of magnetic garnet media with artificial magnetic lattice

As proof of principle of the magneto-optic holographic three dimensional display, *a*-TbFe film, a material widely used in thermomagnetic recording applications [6], [18]–[20], was used as magnetic media. However, according to equation 2.2.2-3 the reconstructed images had a low brightness: $4.4 \times 10^{-2} \text{ cd/m}^2$ with reconstruction illumination of 10.8 mW/cm^2 at 532 nm. To represent a 3D image with 100 cd/m^2 from the *a*-TbFe film would require reconstruction illumination of an impractical power, approximately 24 W/cm^2 .

In this section, BiDyYFeAlG and MPC media with the garnet were adopted to improve diffraction efficiency and brightness. As explained in section 2.2, the magnetic film should have high transmittance and a large Faraday rotation angle for improved diffraction efficiency. BiDyYFeAlG shows the high transmittance and large Faraday rotation angle in visible wavelengths. Fabry–Pérot resonance in MPCs structures was also considered. MPCs with a defect layer of thin MO film can exhibit properties similar to thick MO films because the MPCs localize light in the magnetic defect layer [10]. The thin MO film should reduce the power consumption for the thermomagnetic recording, clarify the recorded pattern, and obtain high diffraction efficiency.

2.4.1 Samples fabrication

BiDyYFeAlG mono layer films were fabricated by changing the thickness using ion beam sputtering on a substituted gadolinium gallium garnet substrate (SGGG substrate). Table. 2.4.1-1 shows the fabrication conditions. The BiDyYFeAlG films were annealed at $700 \text{ }^\circ\text{C}$ for 10 minutes in atmosphere to obtain a poly crystalline state.

An MPC was designed by considering the balance of the brightness and the angular dependence. The structure was calculated by a matrix approach [12]. The designed MPC had a magnetic defect layer of BiDyYFeAlG. Bragg mirrors were constructed using multiple layers of SiO_2 and Ta_2O_5 . The MPC was fabricated by ion beam sputtering on a SGGG substrate, and the resulting structure was the SGGG substrate / $(\text{Ta}_2\text{O}_5/\text{SiO}_2)^2$ / BiDyYFeAlG / $(\text{SiO}_2/\text{Ta}_2\text{O}_5)^2$. The

Table 2.4.1-1 Sputtering conditions of RF ion beam sputtering.

Substrate	SGGG (Substituted Gadolinium Gallium Garnet)
Target	$\text{Bi}_{1.5}\text{Dy}_{1.0}\text{Y}_{1.0}\text{Fe}_{3.8}\text{Al}_{1.2}\text{O}_x$, SiO_2 , Ta_2O_5
Gas	Ar: 6 ccm, O_2 :10 ccm
Beam conditions	1000 V / 10 mA
Post anneal	$700 \text{ }^\circ\text{C}$ 10 min, atmosphere

designed thickness of the BiDyYFeAlG layer was 1.05 μm . The thickness of the SiO_2 and Ta_2O_5 layers were determined as $\lambda/4n$, where λ was the resonant wavelength of 532 nm and n is the refractive index of each material. The material parameters used in the matrix approach were experimentally determined and are shown in Table. 2.4.1-2. The sample, after the deposition of BiDyYFeAlG layer, was annealed at 700 $^\circ\text{C}$ for 10 minutes in atmosphere. The localized wavelength of the MPC was tuned to 532 nm by the thickness of cap Bragg mirror layers. Fabricated sample structures were shown in Fig. 2.4.1-1 and 2.4.1-2

Table 2.4.1-2 Material parameters in the matrix approach. ^a

Material	N	κ	θ_F ($^\circ/\mu\text{m}$)
BiDyYFeAlG	2.27	0.0186	2.13
SiO_2	1.45	0	-
Ta_2O_5	2.16	0	-

^a Refractive index n , extinction coefficient κ , and specific Faraday rotation angle θ_F .

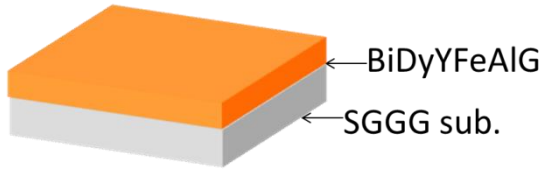


Fig. 2.4.1-1 Schematic structure of BiDyYFeAlG mono layer film.

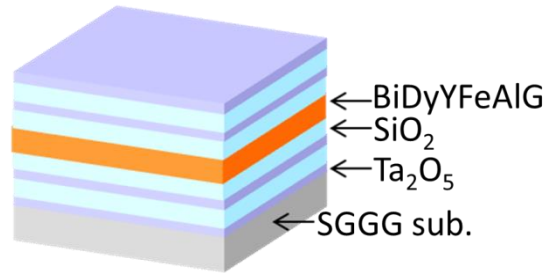


Fig. 2.4.1-2 Schematic structure of the MPC.

2.4.2 Magneto-optical and optical properties

The measured transmittance and Faraday rotation angle for fabricated samples at the wavelength of 532 nm are shown in Fig. 2.4.2-1(a) and (b). The transmittance of BiDyYFeAlG mono layer films decreased with increasing thickness. On the other hand, the Faraday rotation angles were increased with increasing thickness. The MO properties of the MPC were compared to BiDyYFeAlG mono layer films with differing thicknesses. The transmittance of the MPC was 32 %, which was lower than a similar thickness mono layer film. However, the Faraday rotation angle of the MPC was 3.2°, which was higher than a similar thickness mono layer film. Figure 2.4.2-2 shows the measured transmittance and the Faraday rotation angle spectrums of the MPC and a mono layer film with similar magnetic layer thickness. According to the above results, the MPC shows performance close to the thick film properties at the localization mode.

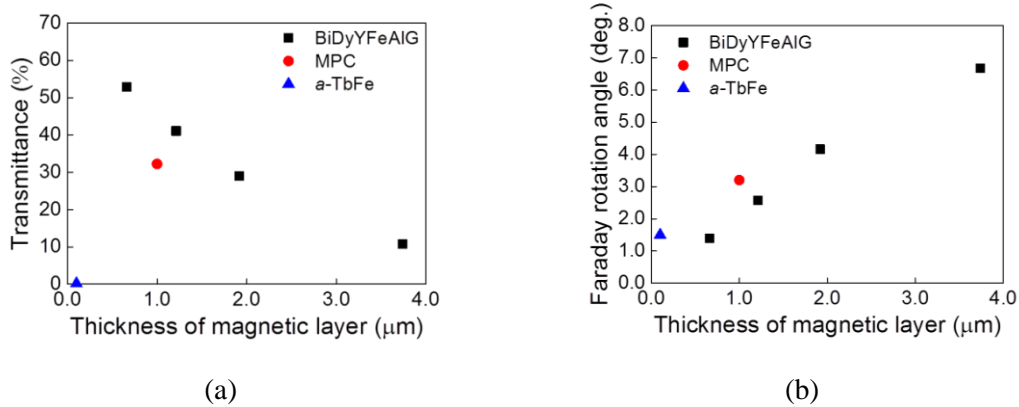


Fig. 2.4.2-1 Magneto-optical and optical properties of fabricated samples. (a) is transmittance, and (b) is Faraday rotation angle.

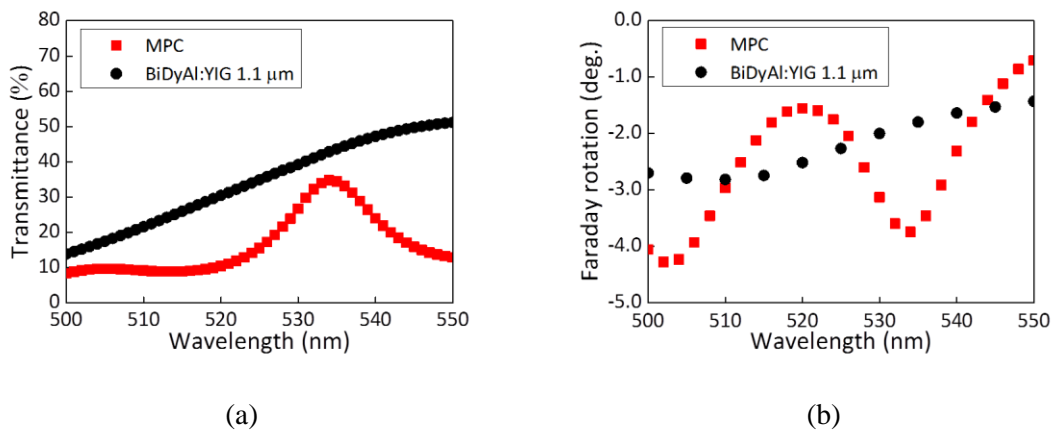


Fig. 2.4.2-2 Spectrum of MPC and a mono layer film. (a) is transmittance, and (b) is Faraday rotation angle.

2.4.3 Measurement of diffraction efficiency

The diffraction efficiencies of fabricated magnetic films were measured by a two-beam interferometer. Figure 2.4.3-1 shows the optical system of the two-beam interferometer. The two-beam interferometer can obtain high energy density for the thermomagnetic recording by using a condenser lens. The incident angle of the two beams was adjusted to 15° so that the line width of an interference fringe pattern was approximately $1.0 \mu\text{m}$ and spatial frequency of the fringe pattern was 500 line pairs/mm. The interference fringe pattern was thermomagnetically recorded on magnetic films using various energy densities, because the diffraction efficiency depends on the depth of recorded fringes. The diffraction efficiency was calculated by equation (2.4.3-1).

$$\eta = T \times \frac{I_1}{I_0} \times 100 (\%) \quad (2.4.3-1)$$

Where η is the diffraction efficiency, T is the transmittance of the magnetic film, I_0 is the zero-order transmitted light, and I_1 is the first order diffracted light, respectively. In equation (2.4.3-1), reconstruction illumination light in equation (2.2.2-1) was replaced by I_0/T .

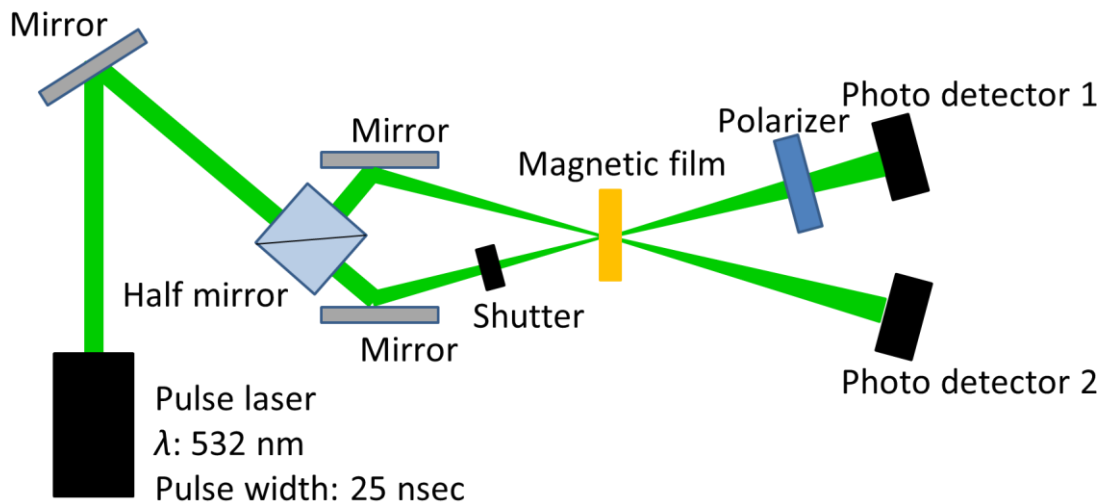


Fig. 2.4.3-1 The two-beam interferometer optical system. First order diffracted light I_1 and transmitted light I_0 were measured by power meters 1 and 2, respectively. A half-wavelength plate and a polarization beam splitter adjust the laser power.

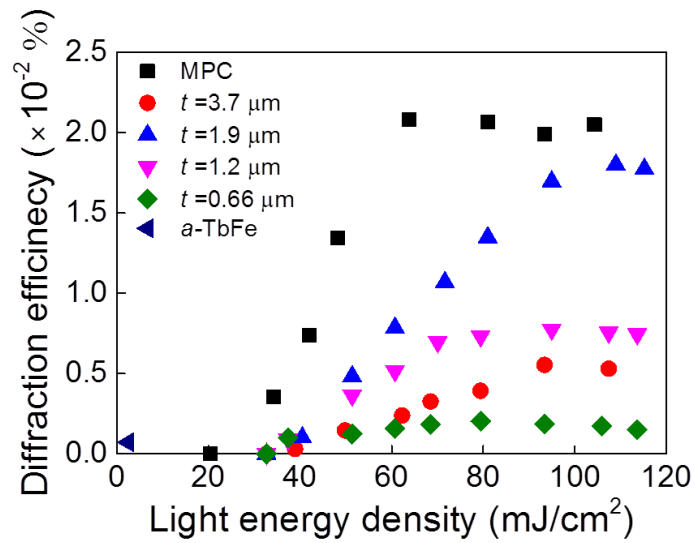
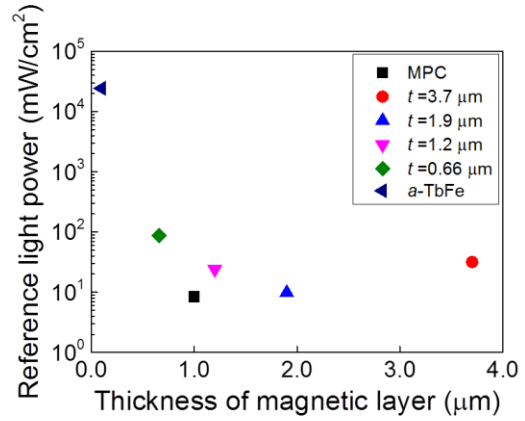
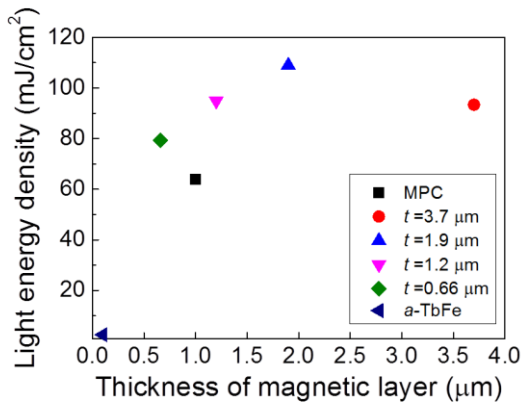


Fig. 2.4.3-2 The relationship between the diffraction efficiency and the light energy density for thermomagnetic recording. Thickness of mono layer films was changed from 0.66 μm to 3.7 μm .

Figure 2.4.3-2 shows the relationship found between the light energy density for the thermomagnetic recording and the resulting diffraction efficiency. The $a\text{-TbFe}$ film when illuminated by the laser with light energy density over 10 mJ/cm^2 was ablated. The diffraction efficiency of the 1.9 μm thick film has a peak value of $1.7 \times 10^{-2}\%$, approximately 2300 times higher than that of the $a\text{-TbFe}$ film. These results mean that BiDyYFeAlG was effective for improving brightness. However, the ratio I_1/I_0 was saturated at a thickness of 1.9 μm and the transmittance of mono layer films decreases at increased thickness; thus, the ratio I_1/I_0 depends on the depth of the recorded fringes. In addition, significant heating occurred in the surface area because of energy absorption, and the shape of the recorded fringe pattern was changed near the surface because of thermal diffusion from the high temperature region there [10]. This caused low fringe depth and the saturation of the diffraction efficiency of the mono layer films. In addition, the diffraction efficiency of the MPC was $2.1 \times 10^{-2}\%$, similar to that of the 1.9 μm thick BiDyYFeAlG mono layer film.

Figure 2.4.3-3 (a) shows the relationship between the thickness of magnetic layer and the recording light energy density for the largest diffraction efficiency, while Fig.2.4.3-3 (b) shows reconstruction illumination power density for generating an image with brightness of the desired 100 cd/m^2 . The reconstruction illumination light power was estimated from diffraction efficiency and equation (2.2.2-3) under the following conditions: viewing angle 22° and

wavelength of reconstruction illumination light 532 nm. The required light energy of the MPC for the thermomagnetic recording was 59 % of the energy needed for the 1.9 μm thick film. In addition, reconstruction illumination light power for the MPC was 10.8 mW/cm^2 to represent 3D images with over 100 cd/m^2 . This power can be realized by a small solid-state laser. These results caused a microcavity structure and a thin defect layer of the MPC. In the MPC, the distribution of absorbed energy was uniform along the thickness direction by Fabry–Pérot resonance between Bragg mirrors. In addition, the MPC reduces the variation of absorbed energy density and thermal distribution along the thickness direction [10]. Therefore, the MPC shows higher diffraction efficiency compared with mono layer films.



(a)

(b)

Fig. 2.4.3-3 (a) The light energy consumption for the thermomagnetic recording. (b) The reconstruction illumination light power for representing 3D images with 100 cd/m^2 brightness using the fabricated magnetic films.

2.4.4 Reconstruction of 3D image

Since the MPC showed the highest diffraction efficiency, a 3D image was constructed from a hologram with the MPC. The hologram was computer-generated by half zone plates converted into a binary hologram, which was the same as the hologram in chapter 1. Figure 2.4.4-1(a) shows a 3D model of the one used to generate the hologram. The reconstruction illumination light was a plane beam with wavelength 532 nm. Pixel size was $1.36 \times 1.36 \mu\text{m}^2$. The total number of pixels in the hologram was $10^4 \times 10^4$ pixels. The viewing angle of the reconstructed image was 22° . The hologram was represented on the MPC by the tiling optical system. The light energy density for fabricating magnetic pixels was $54 \text{ mJ}/\text{cm}^2$.

The reconstructed image from the MPC and the reconstructed image from the *a*-TbFe were compared in the same optical conditions. The reconstruction optical system consisted of a reconstruction illumination source, a polarizer, and an analyzer with cross-Nicol configuration for separating zero-order transmitted light and the reconstructed image. The reconstruction illumination required to achieve $100 \text{ cd}/\text{m}^2$ image brightness was a continuous wave laser with a wavelength of 532 nm and intensity of $10.8 \text{ mW}/\text{cm}^2$. Figure 2.4.4-1 (b)–(d) show the reconstructed 3D holographic image from the MPC, and (e)–(g) show the reconstructed image from the *a*-TbFe. The brightness of the reconstructed image from the MPC was $100 \text{ cd}/\text{m}^2$.

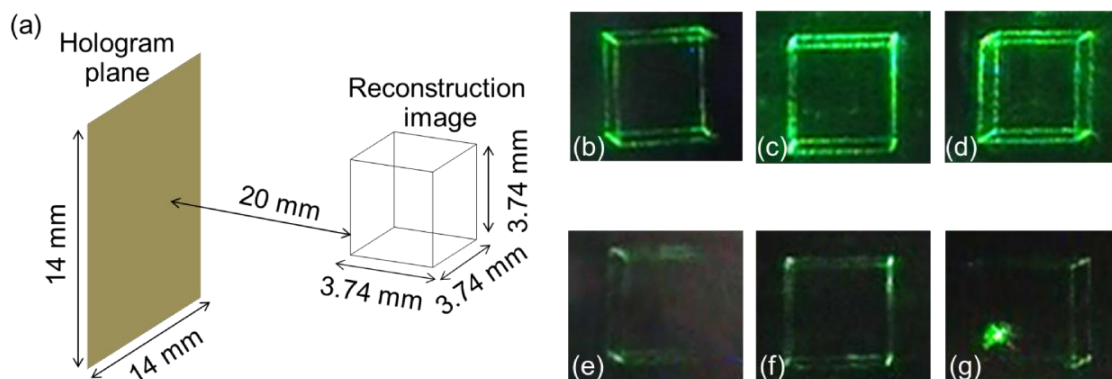


Fig. 2.4.4-1 (a) A model of 3D image for generating the hologram. The wireframe cube was constructed by point light sources. Reconstructed images from MPC (b)–(d) and from *a*-TbFe (e)–(g). (b) and (e) were images from left view point of 11° . (c) and (f) were from center. (d) and (g) were images from right view point of 11° .

2.5 Artificial magnetic lattice media with dissimilar materials

In section 2.4, BiDyYFeAlG films and the MPC were evaluated to improve diffraction efficiency and brightness. Thus, using BiDyYFeAlG was effective in improving diffraction efficiency. However, recording energy density was increased compared to *a*-TbFe film. This issue was caused from a trade-off in terms of light absorption corresponding to the diffraction efficiency. According to equation 2.2.2-6, Fig. 2.4.2-1 symbolized the trade-off. Apropos this, MPC showed a reduction of the recording energy density, and the light behavior in defect layer was close to the thick film. On the other hand, heat behavior in the defect layer was reasonable for the defect layer thickness. In other words, it implied that behaviors of heat and light in the BiDyYFeAlG defect layer against the layer thickness could be separated by the artificial structures [21].

To solve such a trade-off, this section proposes the use of multilayer media comprising two dissimilar magnetic materials showing high diffraction efficiency and low writing energy for the hologram. The structure was constructed with two magnetic materials, which were separated optically and combined magnetically. One material, which has a high light absorption material with large magnetization, was used as the writing layer to reduce recording energy density and to control magnetization direction of another layer. The other layer was reconstruction layer, which was a low-light absorption material with high diffraction efficiency and low coercivity. A floating magnetic field from the writing layer transcribes a magnetic hologram to the reconstruction layer.

This section describes the design and fabrication of the structure, and observes the transfer of a magnetic hologram to the reconstruction layer.

2.5.1 Design of structure

Figure 2.5.1-1 shows the schematic image of the multilayer structure. A layer of *a*-TbFe was used as the writing layer, and the BiDyYFeAlG layer was used as the reconstruction layer. The *a*-TbFe and SiN layers had the same structure as the *a*-TbFe film used in previous research. The thickness of magnetic garnet layer was chosen by considering floating magnetic field from the *a*-TbFe layer. In this structure, illumination reconstruction light for reconstruction of hologram was incident from the BiDyYFeAlG side, and holograms were reconstructed in the reflect mode. To prevent the illumination reconstruction light from being incident on the writing layer, a thin Al layer was incorporated between both magnetic layers. Figure 2.5.1-2 shows the calculated thickness dependence of Al layer reflectance. The reflectance was saturated with over 20 nm thickness. From this result, the thickness of the Al was decided as 20 nm.

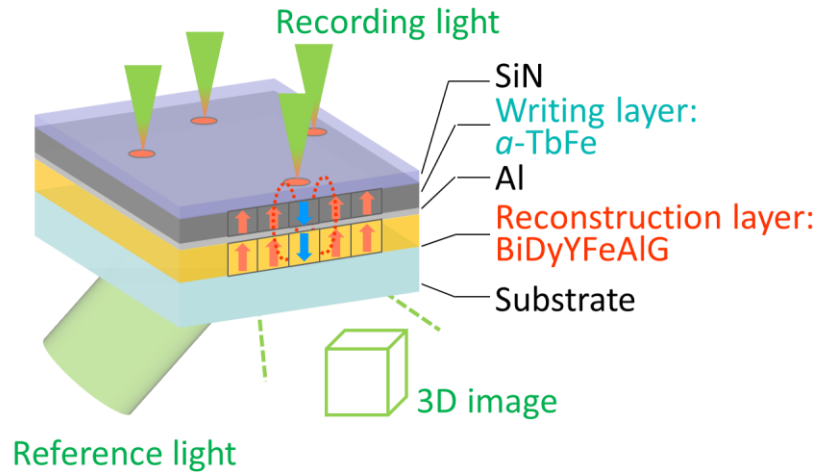


Fig. 2.5.1-1 The concept of α -TbFe/BiDyFeAlG multilayer media. Hologram was recorded on α -TbFe side with thermomagnetic recording, and was transferred to BiDyFeAlG layer.

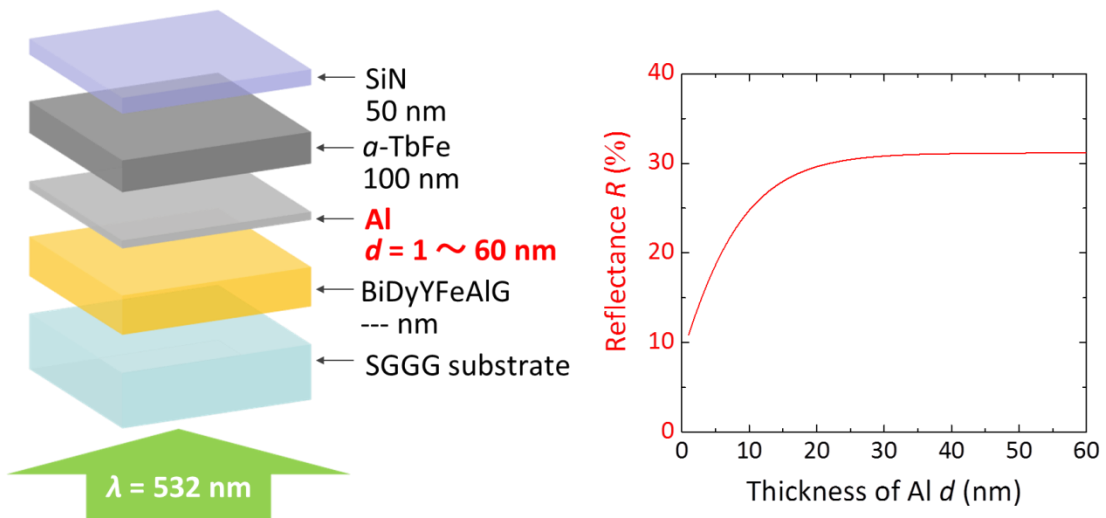


Fig. 2.5.1-2 The thickness dependence of reflectance; incident was from the BiDyFeAlG layer side.

2.5.2 Sample fabrication

Each layer of the multilayer media was fabricated by ion beam sputtering; conditions for this process are shown in Table 2.5.2-1. The BiDyYFeAlG layer was fabricated by RF ion sputtering, and was annealed after sputtering at 750 °C for 15 minutes. After the annealing, Al, *a*-TbFe, and SiN layers were fabricated by DC ion beam sputtering. In addition, an *a*-TbFe film and a BiDyYFeAlG film, which are the same structure, were fabricated to compare multilayer media.

Magnetic and magneto optical properties of fabricated films were measured. Figure 2.5.2-1 shows *M-H* hysteresis loops of the multilayer media, an *a*-TbFe film (Substrate/SiN 20 nm/*a*-TbFe 100 nm/ SiN 50 nm), and BiDyFeAlG film (Substrate/ BiDyFeAlG 576 nm). The *M-H* hysteresis loop of the multilayer media was reasonable as it synthesized both magnetic layers. Figure 2.5.2-2 shows the MO hysteresis loop of fabricated samples. The BiDyFeAlG film was measured by MO Faraday loop, and the BiDyFeAlG side of multilayer film and the *a*-TbFe film were measured by MO Kerr loop. Measured rotation angle of the multilayer film was 1.5°, which was about 1.5 times larger than the Faraday rotation angle of the BiDyYFeAlG film.

Table 2.5.2-1 Conditions of ion beam sputtering.

Power supply type	Radio frequency	Direct current
Target	Bi _{1.5} Dy _{1.0} Y _{1.0} Fe _{3.8} Al _{1.2} O _x ,	Tb ₂₁ Fe ₇₉ , SiN, Al
Gas	Ar: 6 ccm, O ₂ :10 ccm	Ar: 6 ccm,
Beam conditions	1000 V/ 10 mA	1000 V/ 30 mA
Post anneal	750 °C 15 min, atmosphere	

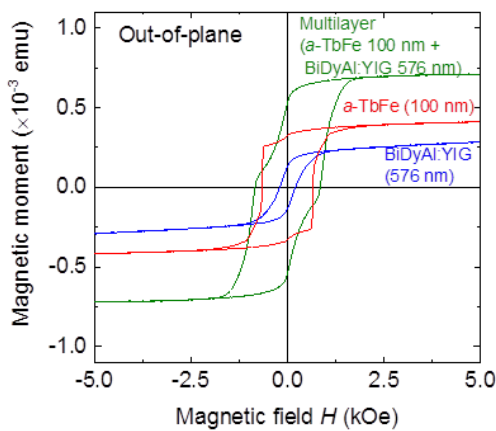


Fig. 2.5.2-2 *M-H* loops of fabricated samples.

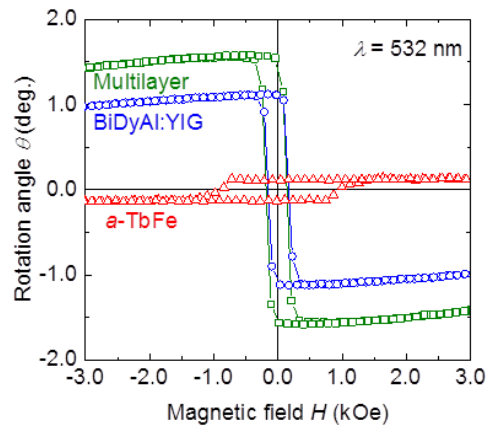


Fig. 2.5.2-3 MO loops of fabricated samples.

2.5.3 Evaluation of light efficiencies

Diffraction efficiencies against recording energy densities were measured for fabricated multilayer film. Simple magnetic grating with $1.36 \mu\text{m}$ linewidth was recorded to the $a\text{-TbFe}$ side of the multilayer film by the tiling optical system. After the recording, diffraction efficiencies were measured on both sides of the multilayer film. Figure 2.5.3-1 shows an optical system to measure the 1st order diffracted light intensity, and incident light intensity was measured at the polarizer. The polarizers were set using cross-Nicol placement.

Figure 2.5.3-2 shows the measurement results of diffraction efficiencies. Thermomagnetic recording to the $a\text{-TbFe}$ side was observed with over 5 mJ/cm^2 laser light energy densities. The peak diffraction efficiency of the $a\text{-TbFe}$ side was approximately $4.8 \times 10^{-5} \%$ with 7.3 mJ/cm^2 laser light. Considering that recording the energy density of a two-beam interferometer is in fact doubled by interference, the recording energy of the $a\text{-TbFe}$ layer was reasonable compared to the results of Fig 2.4.3-2. Diffraction efficiency measured by the BiDyYFeAlG side was $0.95 \times 10^{-3} \%$. In the previous result in section 2.4.3, at least over 20 mJ/cm^2 was required to record a magnetic hologram on the BiDyYFeAlG film. One cause of the reducing recording energy densities was thermal or magnetic influence from the $a\text{-TbFe}$ layer. In addition, diffracted light from the BiDyYFeAlG side had a 11° diffracted angle against normal incident light, which was reasonable for the linewidth of the magnetic grating.

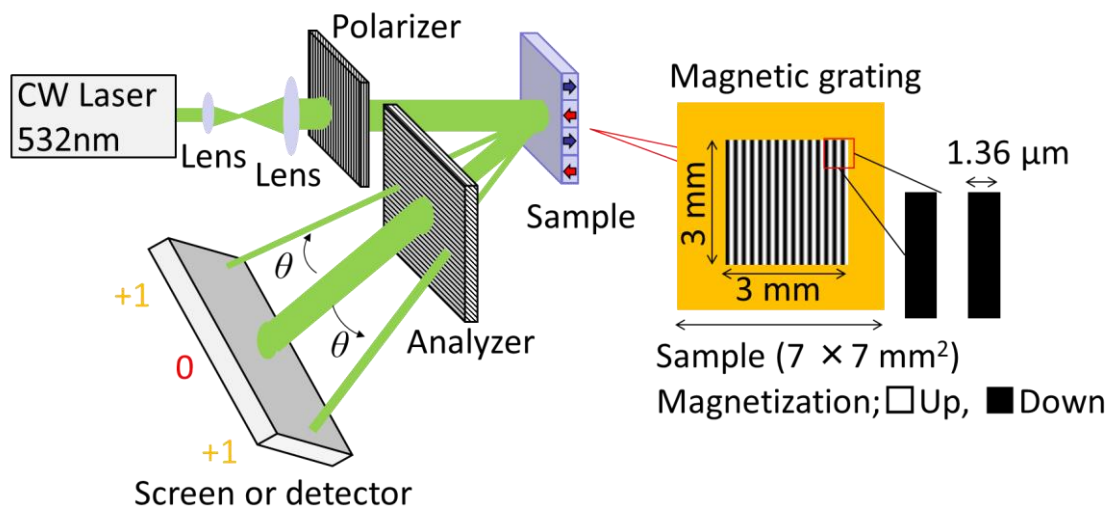


Fig. 2.5.3-1 Schematic image of the optical system for measuring diffraction efficiency.

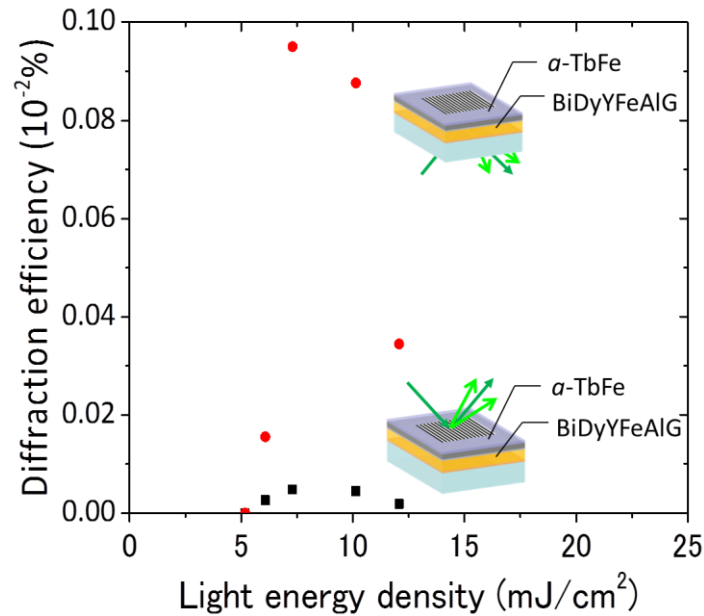


Fig. 2.5.3-2 Measured diffraction efficiencies of the multilayer film. Red plots were measurement results of the BiDyYFeAlG side, black plots were results of the *a*-TbFe side.

On the other hand, diffraction efficiency rapidly reduced against higher laser light energy densities. This phenomenon was clearly different compared to the behavior of directly recorded garnet films in terms of diffraction efficiency change against energy density change. This phenomenon caused thermal diffusion and the collapse of the fringe shape on the *a*-TbFe layer.

These results showed that the *a*-TbFe/BiDyYFeAlG was effective in improving both light efficiencies to record and reconstruct magnetic hologram with fine pixels. Recording properties of the multilayer film could be considered to depend on the thickness of the BiDyYFeAlG layer and the Al layer. Therefore, by inserting a dielectric mirror between the substrate and BiDyYFeAlG layers, a further improvement of diffraction efficiency can be expected.

2.5.4 Reconstruction of 3D image

In the next step, the hologram of a wireframe cube was recorded and reconstructed from the multilayer film. The hologram was computed with the half zone plate method, and recorded on the *a*-TbFe side using the tiling optical system with $7.3 \mu\text{J}/\text{cm}^2$ light energy density. The total resolution was 3800×3800 pixels and display size was 5×5 mm. Figure 2.5.4-1 shows polarized microscope images and their original versions, in which each image shows the magnetization distributions of each side of the multilayer film. The contrast between images from both sides was reversal, because the rotation angle of each layer was the opposite of the other. The hologram pattern recorded to the *a*-TbFe side was transferred to the BiDyYFeAl layer.

To reconstruct the magnetic hologram, reconstruction illumination light was normally incident on the BiDyYFeAlG side via a polarized beam splitter (PBS), and the reconstructed image was observed by reflection mode via PBS. Figure 2.5.4-2 shows the reconstructed image from the BiDyYFeAlG side of the multilayer film.

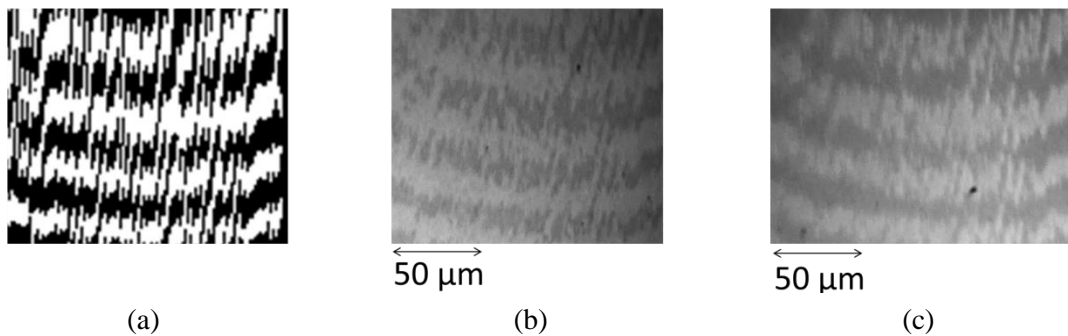


Fig. 2.5.4-1 Polarized microscope images and the original recorded hologram images (a) is the original image on DMD, (b) was recorded image on the *a*-TbFe layer, and (c) was transferred image on the BiDyYFeAlG layer.

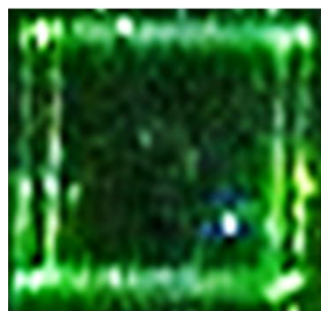


Fig. 2.5.4-2 Reconstructed image from the BiDyYFeAlG layer side; one side of the cube was approximately 3 mm.

2.6 Summary

Chapter 2 discussed the improvement of light efficiency of magnetic media. To apply magnetic media for holographic display, light efficiencies of recording and reconstructing of hologram were regarded as a problem, and these efficiencies dominated by media material.

In this thesis, artificial magnetic lattice structure was used to improve these light efficiencies. An MPC was fabricated by ion beam sputtering on a SGGG substrate, and the resulting structure was a SGGG substrate / $(\text{Ta}_2\text{O}_5/\text{SiO}_2)^2$ / BiDyYFeAlG / $(\text{SiO}_2/\text{Ta}_2\text{O}_5)^2$. The MPC shows a performance close to the thick film properties in the localization mode. By using the magnetophotonic crystal, the recording and reconstructing light efficiencies were improved. The MPC media showed a diffraction efficiency of $2.1 \times 10^{-2}\%$, and could generate 3D images with over 100 cd/m^2 brightness using reconstruction illumination of 10.8 mW/cm^2 . Illumination light energy was greatly reduced from 24 W/cm^2 of the *a*-TbFe film. In addition, the MPC could reduce the light energy density for thermomagnetic recording by 59 % relative to the mono layer BiDyYFeAlG film, which had similar diffraction efficiency.

In addition, a multilayer structure was proposed that comprised two different magnetic materials as magnetic hologram media showing high diffraction efficiency and low writing energy. Thermomagnetic recording to the *a*-TbFe side was observed with over 5 mJ/cm^2 laser light energy density. The peak diffraction efficiency the of *a*-TbFe side was approximately $4.8 \times 10^{-5}\%$ with 7.3 mJ/cm^2 laser light. Considering the recording energy density of previous works, the recording energy of the *a*-TbFe layer was reasonable. The diffraction efficiency measured by the BiDyYFeAlG side was $0.95 \times 10^{-3}\%$. At least 20 mJ/cm^2 was required to record magnetic hologram on the BiDyYFeAlG film. One cause of the reducing recording energy density was thermal or magnetic influence from the *a*-TbFe layer. In addition, diffracted light from the BiDyYFeAlG side had a 11° diffracted angle against normal incident light, which was reasonable for the linewidth of the magnetic grating. The *a*-TbFe/BiDyYFeAlG multilayer media showed high a diffraction efficiency corresponding to the BiDyYFeAlG layer and low recording energy density corresponding to the *a*-TbFe layer.

References

- [1] H. Takagi, P. Boey Lim, M. Inoue, and H. Umezawa, "Solid-State Spatial Light Modulator with Magneto-Optical Effect," *Rev. Laser Eng.*, vol. 38, no. 5, pp. 356–362, 2010.
- [2] S. Tay, P. Blanche, R. Voorakaranam, A. V. Tunç, W. Lin, S. Rokutanda, T. Gu, D. Flores, P. Wang, G. Li, P. St Hilaire, J. Thomas, R. A. Norwood, M. Yamamoto, and N. Peyghambarian, "An updatable holographic three-dimensional display.," *Nature*, vol. 451, no. 7179, pp. 694–698, 2008.
- [3] K. Buse, A. Adibi, and D. Psaltis, "Non-volatile holographic storage in doubly doped lithium niobate crystals," *Nature*, vol. 393, no. 6686, pp. 665–668, 1998.
- [4] H. Horimai, X. Tan, and J. Li, "Collinear holography," *Appl. Opt.*, vol. 44, no. 13, p. 2575, May 2005.
- [5] Y. Nakamura, H. Takagi, P. B. Lim, and M. Inoue, "Effect of recording condition on the diffraction efficiency of magnetic hologram with magnetic garnet films," *J. Appl. Phys.*, vol. 116, no. 10, 2014.
- [6] H. Takagi, K. Nakamura, T. Goto, P. B. Lim, and M. Inoue, "Magneto-optic spatial light modulator with submicron-size magnetic pixels for wide-viewing-angle holographic displays.," *Opt. Lett.*, vol. 39, no. 11, pp. 3344–7, 2014.
- [7] Y. Nakamura, H. Takagi, P. B. Lim, and M. Inoue, "Magnetic volumetric hologram memory with magnetic garnet," *Opt. Express*, vol. 22, no. 13, pp. 16439–16444, 2014.
- [8] R. Isogai, N. Sagara, T. Goto, Y. Nakamura, P. B. Lim, and M. Inoue, "Diffraction Efficiency of Volumetric Magnetic Holograms with Magnetophotonic Crystals," *J. Magn. Soc. Japan*, vol. 38, no. 3–2, pp. 119–122, 2014.
- [9] M. Levy, "Normal modes and birefringent magnetophotonic crystals," *J. Appl. Phys.*, vol. 99, no. 7, 2006.
- [10] M. Inoue, R. Fujikawa, A. Baryshev, A. Khanikaev, P. Lim, H. Uchida, O. Aktsipetrov, A. Fedyanin, T. Murzina, and A. Granovsky, "Magnetophotonic crystals," in *INTERMAG 2006 - IEEE International Magnetism Conference*, 2006, vol. 39, pp. 19–19.
- [11] H. Kato, T. Matsushita, A. Takayama, M. Egawa, K. Nishimura, and M. Inoue, "Theoretical analysis of optical and magneto-optical properties of one-dimensional magnetophotonic crystals," *J. Appl. Phys.*, vol. 93, no. 7, pp. 3906–3911, 2003.
- [12] M. Inoue, T. Fujii, and I. Introduction, "A theoretical analysis of magneto-optical Faraday effect of YIG films with random multilayer structures," *J Appl Phys*, vol. 81, no. 8, pp. 5659–5661, 1997.
- [13] H. Haskal, "Polarization and efficiency in magnetic holography," *IEEE Trans. Magn.*, vol. 6, no. 3, pp. 542–545, Sep. 1970.

- [14] L. A. Zanoni and L. A. Barton, "Magnetic Holography," *Appl. Opt.*, vol. 9, no. 10, pp. 2275–2279, 1970.
- [15] H. Horimai, A. Inoue, T. Miyama, T. Fujii, S. Suzuki, R. Kusaka, and T. Tokushima, "High-Density Information Storage by Means of Magnetic Holography on Amorphous TbFe Thin Films," *J. Magn. Soc. Japan*, vol. 8, no. 2, pp. 109–112, 1984.
- [16] M. Inoue, K. Arai, T. Fujii, and M. Abe, "One-dimensional magnetophotonic crystals," *J. Appl. Phys.*, vol. 85, no. 8, p. 5768, 1999.
- [17] M. Inoue, K. Arai, T. Fujii, and M. Abe, "Magneto-optical properties of one-dimensional photonic crystals composed of magnetic and dielectric layers," *J. Appl. Phys.*, vol. 83, no. 11, p. 6768, 1998.
- [18] 日本材料科学会, "先端材料辞典". 裳華房, 1987. (in Japanese)
- [19] T. G. Pokhil, B. S. Vvedensky, and E. N. Nikolaev, "Thermomagnetic recording in the TbFe films and thermal stability of signals," 1990, vol. 1274, pp. 293–304.
- [20] H. Takagi, K. Nakamura, S. Tsuda, T. Goto, P. Boey Lim, and M. Inoue, "Magneto-optic Three-Dimensional Holographic Display with Tiling Optical Addressing Method," *Sensors Mater.*, vol. 27, no. 10, pp. 1003–1008, 2015.
- [21] K. Nakamura, H. Takagi, T. Goto, P. B. Lim, H. Horimai, H. Yoshikawa, V. M. Bove, and M. Inoue, "Improvement of diffraction efficiency of three-dimensional magneto-optic spatial light modulator with magnetophotonic crystal," *Appl. Phys. Lett.*, vol. 108, no. 2, 2016.

3. Computer generated hologram for binary hologram

3.1 Introduction

Computer generated holograms (CGHs) are a technique to generate arbitrary holograms, which can reconstruct the desired light field. CGHs have some advantages compared to digital holography and photograph-based holography, as shown below. For these reasons, our group has been using CGHs to demonstrate magnetic hologram reconstruction. However, the calculation method of the hologram, such as the wireframe cube used in previous chapters, was unsuitable for calculating complex objects with surface.

(1) Non-limitation for recording optical system

Digital holography and photograph-based holography have to use light interference on the sensor or photosensitive materials. On the other hand, CGHs can treat a minimized object, such as the moon, humans, and more [1].

(2) High affinity for digital data

CGHs can use digital data instead of object light field to obtain object information (e.g., measurement result of fMRI, CT, and depth camera). In addition, non-real objects can be also used as models [2]–[5].

(3) Optimization for holographic display

In CGHs, parameters of holograms can be arbitrarily chosen. Wavelength, pixel size, display resolution, and more can be optimized to the holographic display [6]–[9].

The purpose of this chapter is the improvement of reconstruction images by calculation method of CGHs. The calculation of object light propagation is especially important for increasing reconstruction image quality. For this purpose, the two-dimensional image based method was investigated to generate holograms of objects with surface, and to reduce calculation times. In addition, optimization of CGHs by considering magnetic pixel position control with simulated annealing (SA) was also investigated.

In section 3.2, the previous calculation method is described to compare the new calculation method. In section 3.3, the calculation principle and processes of two-dimensional image based method, considering of occlusions, and comparing of calculation times are described. In section 3.4, noise reduction by hologram optimization is discussed.

3.2 Hologram calculation with point based method

3.2.1 Fresnel zone plate

The point-based method treats a 3D object as point cloud data. Each point in the point cloud data is assumed to be a self-luminous point. An elementary hologram is calculated for every point source. The whole hologram of the desired object is synthesized by superimposing all the elementary holograms [10][11]. The elementary hologram is called Fresnel zone plate, which is an inline Gabor hologram. Fresnel zone plate is calculated as a light propagation from position of itself to the hologram plane (Fig 3.2.1-1), and can be written as

$$I(x, y) = \frac{A}{R} \cos(k_0 R), \quad (3.2.1-1)$$

$$R = \sqrt{(x - \xi)^2 + (y - \eta)^2 + z^2} \quad (3.2.1-2)$$

Where $I(x,y)$ is light distribution on hologram plane, A is the intensity of the point light source, $k_0=2\pi/\lambda$ is the wavenumber of the laser light, and R is the radial distance between position of light source and point of coordinates (x, y, z) . Then, a radius r of Fresnel zone plate should be limited according to the following equation,

$$r = z \tan\left(\sin^{-1} \frac{\lambda}{2d}\right). \quad (3.2.1-4)$$

Where r is radius of Fresnel zone plate, λ is wavelength of the laser light, and d is the minimum pixel size on holographic media. Outside area of radius r is not supposed by spatial frequency of the media.

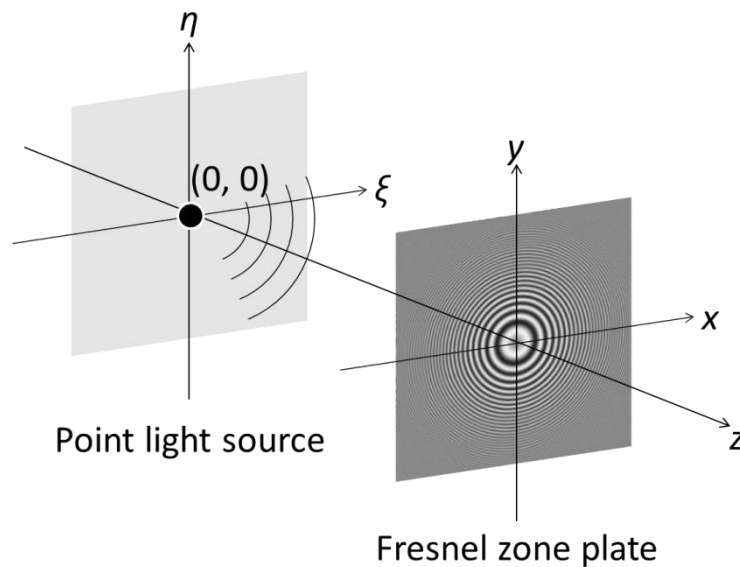


Fig. 3.2.1-1 Optical system on calculation of a Fresnel zone plate.

From equation (3.2.1-1), the whole hologram can be obtained as

$$I(x, y) = \sum_{j=1}^N \frac{A_j}{R_j} \cos(k_0 R_j). \quad (3.2.1-4)$$

Where N is the total number of point light sources, and A_j, R_j are intensity and distance for j^{th} point light sources ($j=1 \dots N$), respectively.

3.2.2 Half zone plate method

Holograms generated with a Fresnel zone plate have problems, which are the same as photography-based holograms. The reconstruction image of the hologram includes a conjugate image and 0^{th} order diffracted light. When the zone plate is illuminated, two wave fronts are generated; a wave front converges to the position of the original point light source, and a conjugate image observed as a divergent wave is generated from the space on the side opposite to the real image with zone plate as the symmetry plane, is generated. To eliminate this noise, a half-zone plate and single sideband filter were used [6]–[8]. Figure 3.2.2-1 shows the light ray of reconstructed images from a half zone plate. Diffracted light rays from the half-zone plate propagate in different directions. In Fig 3.2.2-1, converging light rays have up direction against optical axis, divergent light rays have down directions. It means that the conjugate and reconstructed images can be separated by propagation directions, and conjugate image can be eliminated by the single sideband filter.

To calculate the hologram using a half-zone plate, the same algorithm as normal point-based method in section 3.2.1 can be used by adding an area limited equation 3.2.1-1.

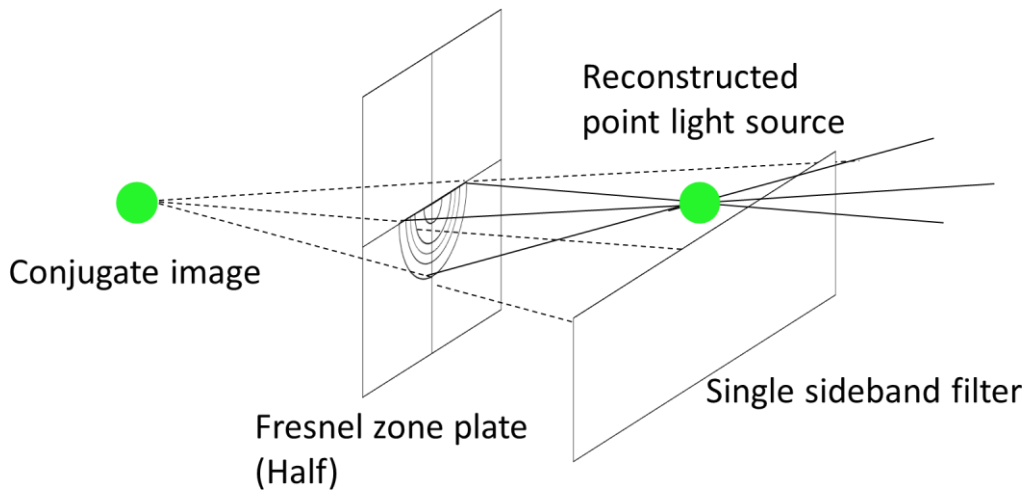


Fig. 3.2.2-1 Reconstruction of point light source with single sideband filter and half zone plate method. Dashed lines mean light rays of a conjugated image and continuous lines mean light rays of real image.

3.3 Hologram calculation with two-dimensional image based method

The point-based method is useful to generate a hologram with very simple and easy calculations. However, this method usually takes long calculation time because calculations are required for each point-light source. To solve the problem, there are many approaches for increasing calculation speed and reduction of calculation factors with optimization of hardware [12], [13]. On the other hand, some approaches, which treat object data as two dimensional images or polygons, have been studied [14]–[16].

In this section, the calculation process and principle of two-dimensional image-based method are described, and the calculation speed of each method is also dealt with. In addition, by reducing calculation time, occlusions can be considered while calculating an object with surface.

3.3.1 Angular spectrum and light propagation

Light propagation between two different planes can be calculated using the angular spectrum method. Angular spectrum method can calculate same results of Rayleigh-Sommerfeld solution at high speed [17].

Monochromatic light propagation from $(x, y, 0)$ plane to (x, y, z) plane was assumed. The complex light field on the $z = 0$ plane be represented by $U(x, y, 0)$, in the same way, $U(x, y, z)$ is a complex light field on the (x, y, z) plane. Across the $z = 0$ plane, $U(x, y, 0)$ has a two-dimensional Fourier transform shown as below,

$$A(f_X, f_Y; 0) = \iint_{-\infty}^{\infty} U(x, y, 0) \exp[-j2\pi(f_X x + f_Y y)] dx dy. \quad (3.3.1-1)$$

From equation 3.3.1-1, $U(x, y, 0)$ can be written as an inverse Fourier transform of its spectrum,

$$U(x, y, 0) = \iint_{-\infty}^{\infty} A(f_X, f_Y; 0) \exp[j2\pi(f_X x + f_Y y)] df_X df_Y. \quad (3.3.1-2)$$

To handle the above equation, a simple plane wave with wave vector \vec{k} , which has magnitude $2\pi/\lambda$ and direction cosines (α, β, γ) , was assumed as illustrated in Fig. 3.3.1-1. The plane wave can be represented as

$$p(x, y, z; t) = \exp[j(\vec{k} \cdot \vec{r}) - 2\pi vt], \quad (3.3.1-3)$$

Where $\vec{r} = x\hat{x} + y\hat{y} + z\hat{z}$ is a position vector with unit-vectors of each axis, while $\vec{k} = \frac{2\pi}{\lambda}(\alpha\hat{x} + \beta\hat{y} + \gamma\hat{z})$. The complex phasor amplitude of the plane wave across a constant z

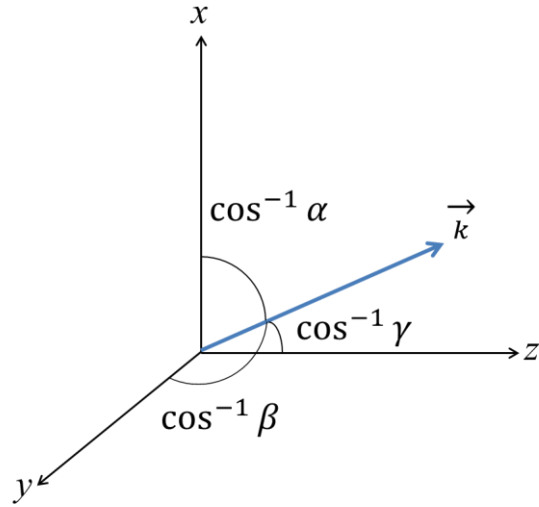


Fig. 3.3.1-1 Wave vector k and direction cosines.

planes is

$$P(x, y, z) = \exp(j\vec{k} \cdot \vec{r}) = \exp\left[j\frac{2\pi}{\lambda}(\alpha x + \beta y)\right] \exp\left[j\frac{2\pi}{\lambda}\gamma z\right], \quad (3.3.1-4)$$

$$\gamma = \sqrt{(1 - \alpha^2 - \beta^2)}. \quad (3.2.1-5)$$

According to these equations, in the $(x, y, 0)$ plane a complex exponential function $\exp[j2\pi(f_x x + f_y y)]$ means a plane wave, which is propagating with direction cosines

$$\alpha = \lambda f_x, \quad \beta = \lambda f_y, \quad \gamma = \sqrt{(1 - (\lambda f_x)^2 - (\lambda f_y)^2)}. \quad (3.2.1-5)$$

Form these equations, equation (3.2.1-1) can be transformed to

$$A\left(\frac{\alpha}{\lambda}, \frac{\beta}{\lambda}; 0\right) = \iint_{-\infty}^{\infty} U(x, y, 0) \exp\left[-j2\pi\left(\frac{\alpha}{\lambda}x + \frac{\beta}{\lambda}y\right)\right] dx dy. \quad (3.3.1-6)$$

Equation (3.3.1-6) is called the angular spectrum of the disturbance $U(x, y, 0)$.

Consider again the propagation of light from the plane $z = 0$ to a parallel plane at nonzero distance z . Propagated complex light field $U(x, y, z)$ can be written as

$$U(x, y, z) = \iint_{-\infty}^{\infty} A(f_x, f_y; z) \exp[j2\pi(f_x x + f_y y)] df_x df_y. \quad (3.3.1-7)$$

Where angular spectrum is treated as functions of spatial frequencies (f_x, f_y) , because it is more

convenient than being treated as functions of the direction cosines (α, β). The angular spectrum $A(f_X, f_Y; z)$ can be written as follows by introducing the Helmholtz equation [17];

$$A(f_X, f_Y; z) = A(f_X, f_Y; 0) \exp\left(j \frac{2\pi z}{\lambda} \sqrt{(1 - (\lambda f_X)^2 - (\lambda f_Y)^2)}\right) \\ \times \text{circ}\left|\sqrt{(\lambda f_X)^2 + (\lambda f_Y)^2}\right|. \quad (3.3.1-8)$$

Where circ function means the bandwidth limitation that is associated with evanescent waves. Equation 3.3.1-7 can be represented by equation (3.3.1-8) as

$$U(x, y, z) = \iint_{-\infty}^{\infty} A(f_X, f_Y; 0) \exp\left(j \frac{2\pi z}{\lambda} \sqrt{(1 - (\lambda f_X)^2 - (\lambda f_Y)^2)}\right) \\ \times \text{circ}\left|\sqrt{(\lambda f_X)^2 + (\lambda f_Y)^2}\right| \exp[j2\pi(f_X x + f_Y y)] df_X df_Y \quad (3.3.1-9)$$

Finally, there transfer function of the light propagation is seen to be

$$H(f_X, f_Y) = \begin{cases} \exp\left[j \frac{2\pi z}{\lambda} \sqrt{(1 - (\lambda f_X)^2 - (\lambda f_Y)^2)}\right] & \sqrt{f_X^2 + f_Y^2} < \frac{1}{\lambda} \\ 0 & \text{otherwise} \end{cases} \quad (3.3.1-10)$$

Thus, the light propagation is stopped outside a circular region of radius $1/\lambda$ in the frequency plane. In the outside region, the wave components are rapidly attenuated by the propagation phenomenon. These components are called evanescent waves. The transfer function (3.3.1-10) is a phase delay in each plane wave accompanying light propagation.

3.3.2 Computing light propagation

Before calculation of the hologram, light propagation between two planes with diffraction was verified. For this purpose, diffraction by grating was calculated. Table 3.3.2-1 shows the grating conditions for the calculation, and Fig. 3.3.2-1 shows the optical systems and process of calculation. The grating was provided as intensity distribution on the left side plane. Light propagation with diffraction was computed with changing the distance z . The propagation calculations were done by equations 3.3.1-9 and 3.3.1-10, and the angular spectrum of grating transmitted light was provided by equation (3.3.1-1) with fast Fourier transform (FFT). Then the area of the $U(x, y; 0)$ needs to be doubled along both the x and y axes, and the additional sampling points must be padded with zeros to prevent aliasing [18]. The product $A(x,y,0) \times H(f_x, f_y)$ provided the phase delay corresponding to propagation. Furthermore, the output window needed to be clipped and reduced to the original size.

Figure 3.3.2-2 shows the calculation results of the propagation. Horizontal axis means the propagation distance between both planes, while vertical axis means the relative position of 1st order diffracted light corresponding to 0th order diffracted light. The calculated relative positions and theoretical relative positions, which were calculated by equation 1.3.2-1, were plotted on the Fig 3.3.2-2.

The diffracted light position showed good agreement with theoretical values. This result means that diffraction by the grating could be computed by using angular spectrum.

Table 3.3.2-1 Grating parameters.

Calculation area	1024 × 1024 pixels
Grating size	100 × 100 pixels
Grating linewidth	2 pixels
Pixel size	2.128 μm
Grating type	Intensity

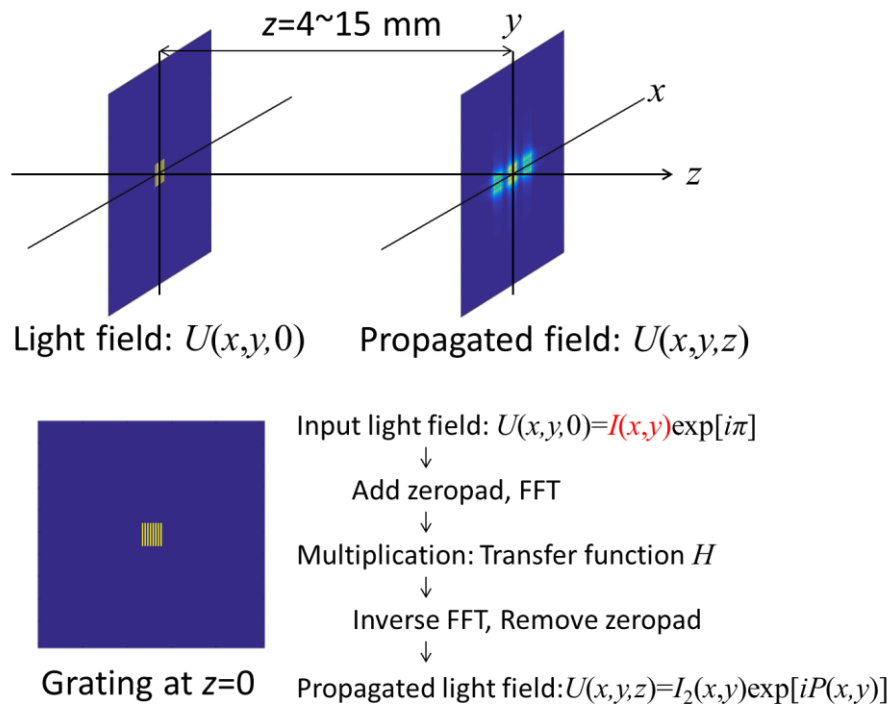


Fig. 3.3.2-1 Schematic simulated optical system for propagation computing.

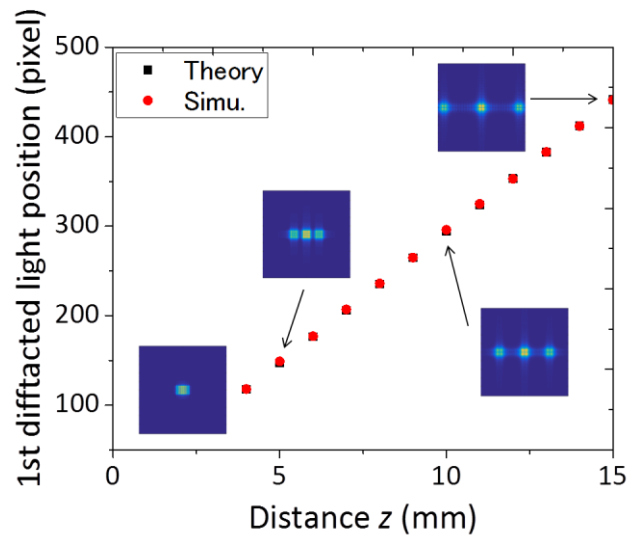


Fig. 3.3.2-2 Calculation results of light propagation with diffraction.

In the next step, continuity of light propagation calculation with angular spectrum was investigated. The optical system and grating parameters were same as in Fig.3.3.2-1, and propagated light field at $z = 0, 5 \text{ mm}, 10 \text{ mm},$ and 15 mm were computed. To investigate the continuity, two types of calculations were done; (a) Propagated light fields at each point were calculated directly. In this case, transfer functions H were calculated for each distance, and all propagations were from the $z = 0$ point. (b) Propagated light fields at each point were calculated to take over previous positions. In this case, a transfer function H was calculated for propagation distance $z = 5 \text{ mm}$ distance. At first, light propagation was calculated from the $z = 0$ to the $z = 5 \text{ mm}$ plane, and the calculated complex light field at $z = 5 \text{ mm}$ was used as input light field in equation 3.3.1-1 to calculate the light field at $z = 10 \text{ mm}$. The light propagation from $z = 10 \text{ mm}$ to $z = 15 \text{ mm}$ was calculated similarly.

The calculation results were shown in Fig. 3.3.2-3. The diffracted light field at each point calculated by both methods showed good agreement. This result means the information of diffracted or propagated light directions were kept in the complex light field. It is supported by the Huygens principle.

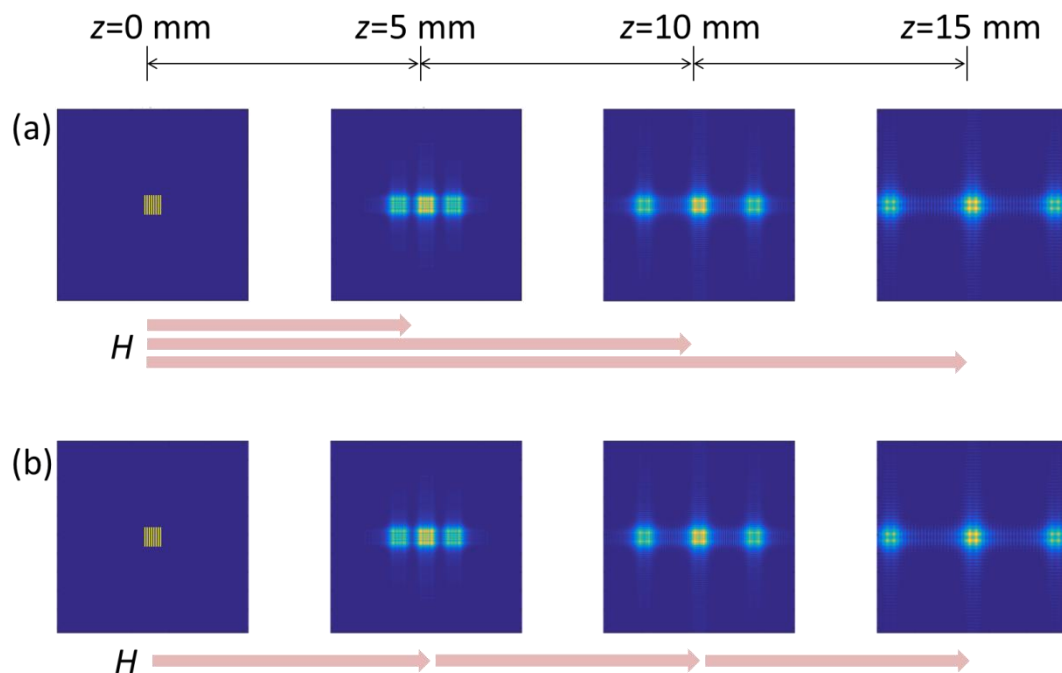


Fig. 3.3.2-3 Continuity of the light propagation calculations, (a) is the intensity distributions of the direct propagated light, (b) is the intensity distribution of the propagated light with taking over.

3.3.3 Calculation process of 2D image-based method

This section deals with the concrete 2D image based calculation method. Computing environments were constructed by MATLAB 2014b. Figure 3-3.3-1 shows the overview of light propagation calculation. A 3D object's data was sampled to a few two-dimensional images. To obtain a hologram of the object at a place, a complex light field was needed at the place. Light field propagation can be separated by propagation distances; light propagation between each sampled plane, and light propagation from top of the object to hologram plane.

Object data was prepared as point cloud data, and was sampled as two-dimensional planes. Each sampled plane included point light sources between itself and the next plane, as shown in Fig. 3.3.3-2. The distance between each plane was chosen as an arbitrary length z_1 ; it defined the resolution of reconstruction images in depth direction. The resolution of these planes should be same as the display resolution of the holographic display. Similarly, pixel pitch of these planes could be also fixed.

Transfer function depends on the propagation distance z in equation 3.3.1-10. On the other hand, it is independent of the absolute coordinates of z axis and object light field. In addition, λ , f_x , and f_y were defined by the optical system in calculations, included hologram resolution and the pixel pitch. Therefore, a transfer function H can be used to calculate light propagation with the same distance z . To reduce calculation time, this section used two transfer functions— H_1 provides phase delay with propagation between each sampled plane (propagation distance is z_1 in Fig 3.3.3-1), H_2 provides phase delay with propagation from the last sampled plane to hologram plane (propagation distance is z_2 in Fig. 3.3.3-1).

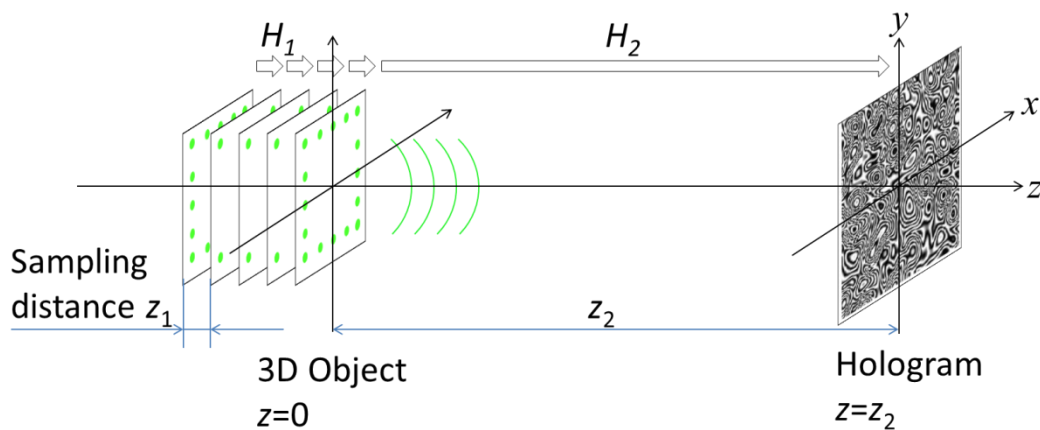


Fig. 3.3.3-1 Overview of light propagation calculation.

For light propagation between each sampled plane, transfer function H_1 and equation (3.3.1-9) were used. In this calculation, the first sampled plane was substituted with the complex light field $U(x, y; 0)$ in equation (3.3.1-9), and was transformed to frequency plane by FFT. Propagation calculation is the same as in section 3.3.2. After the propagation, the next sampled plane on the coordinates $z = z_1$ was added to propagated light field $U(x, y; z_1)$, and light propagation from $z = z_1$ to $z = 2z_1$ was computed. By repeating these processes, a complex light field at the last sampled plane was obtained, in which light fields from all point sources were included. Finally, object light field at $z = z_2$ could be obtained by equation (3.3.1-9), and was a hologram of the sampled 3D object. Calculated holograms were treated as binary or 24 bit bitmap film for visualizing on DMD.

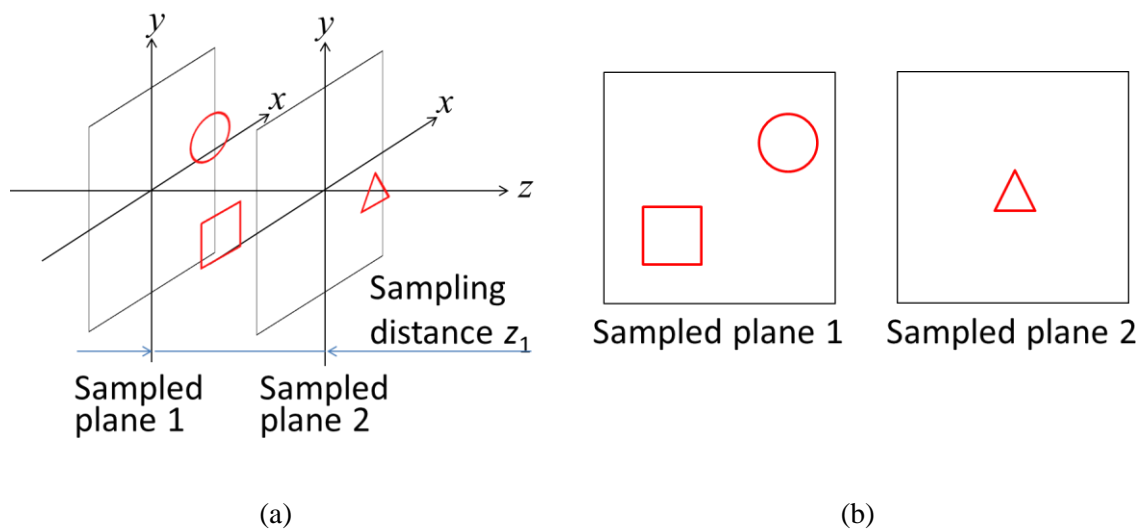


Fig. 3.3.3-2 Schematic image of sampled 2D images; circle and square positioned between sampled plane 1 and plane 2 were treated as a light source on plane 1.

3.3.4 Calculation process of occlusions

Occlusion is a phenomenon in which light from an object is blocked by other objects placed on the optical path. It is an important cue for recognizing object depth. However, occlusion is often ignored in basic research for holographic display [19], and the reconstruction images become “see through” objects, such as the cube in this paper.

To add occlusions for our CGHs, the polygon by polygon method was used in the 2D-image based method [20]. The basic concept is shown in Fig.3.3.4-1. We assumed two planes in Fig. 3.3.4-1. Scattered light from reconstruction image 1 achieved reconstruction image 2 with the light propagation calculation described in section 3.3.2. To calculate holograms of these planes, light distribution of reconstruction image 2 was added to the propagated light field from reconstruction image 1. Then, a part of the propagated light field from reconstruction image 1, which was overlapped with reconstructed image 2, was deleted. This is equivalent to propagated light being blocked by reconstruction image 2. This is the simplified overview of the calculation process of occlusions.

In the above case, the deleted area was the shape of reconstruction image 2. To apply to 3D objects, the shape of the deleted area should be set to be the same as the silhouette of the 3D object. Figure 3.3.4-2 shows the schematic image of calculation method of occlusions. Complex light at i^{th} layer L_i can be written as

$$L_i(x, y, z_i) = I_i(x, y, z_i) + U_{i-1}(x, y, z_i)T_i(x, y, z_i) \quad (3.3.4-1)$$

$$T_i(x, y, z_i) = \begin{cases} 1 & a > 0 \\ 0 & a = 0 \end{cases} \quad (3.3.4-2)$$

$$a = \sum_{j=i}^N I_j(x, y, z_j). \quad (3.3.4-2)$$

Where $I_i(x, y, z_i)$ is point light sources at the i^{th} sampled plane, $U_{i-1}(x, y, z_i)$ is light field propagated from $i-1^{\text{th}}$ sampled plane, N is the number of sampled planes, and $T_i(x, y, z_i)$ is a transmittance function with object silhouette.

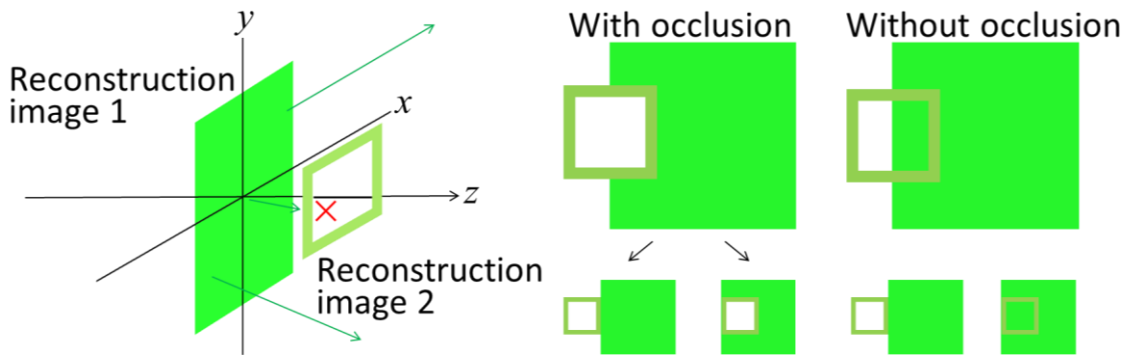


Fig. 3.3.4-1 Schematic image of considering occlusion.

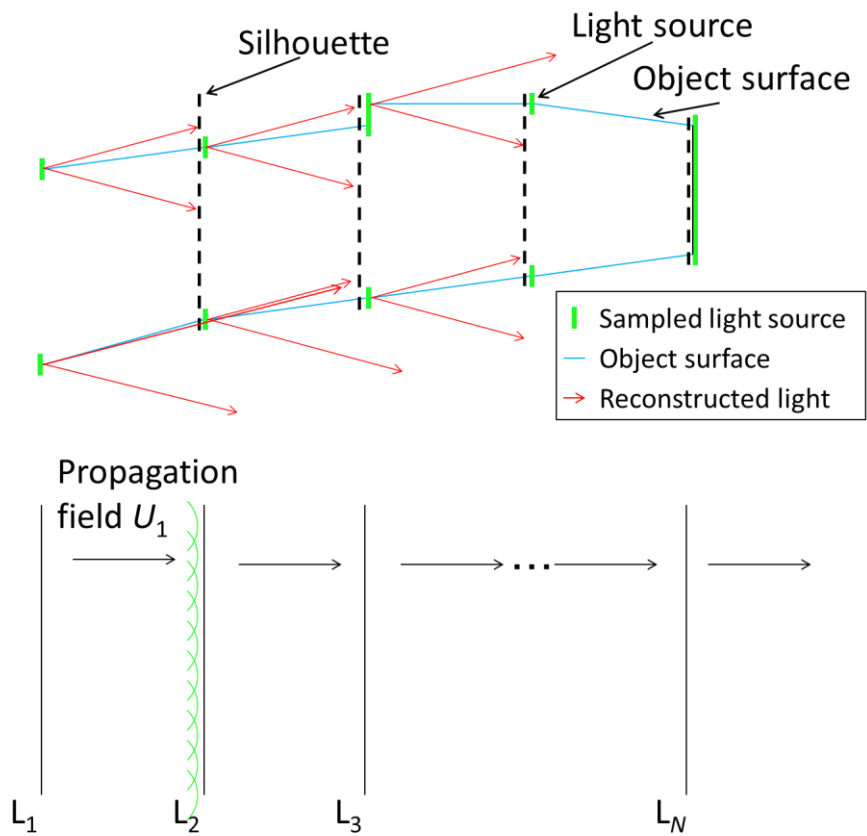


Fig. 3.3.4-2 Overview of occlusion calculation.

3.4 Hologram optimization with simulated annealing

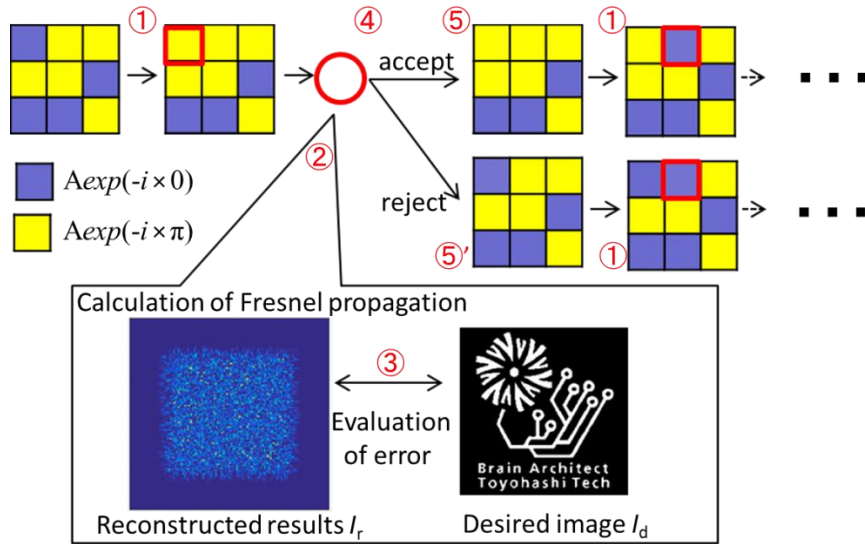
Binarization errors are a hindrance in producing magnetic holograms. Magnetic holograms are represented as directions of magnetization, in which a magnetic pixel has only two states, up or down. These holograms called “binary holograms”. Binary holograms can be displayed on binary spatial light modulators (SLMs) such as digital micromirror device (DMD), therefore they are used in applications like high speed optical addressing holographic displays [21]. On the other hand, it is known that reconstruction images of CGHs include error caused from quantization of fringes [22]. In the case of binary holograms, the quantization error, known as “binarization error”, is the largest.

Binarization error can be erased or suppressed by the calculation method of holograms and by the binarization process to convert from a non-quantization fringe [23], [24]. For this, pixel positions of the magnetic hologram that are not fixed mechanically were focused on. Controlling pixel position is expected to reduce error in the reconstruction image, like Lohman’s binary hologram [25]. However, holograms for holographic 3D displays are handled as 2D images or 2D matrix. Therefore, this section investigates the hologram optimization method, which can control pixel positions on 2D image.

3.4.1 Simulated annealing

Simulated annealing (SA) is used to optimize hologram patterns [26], [27]. Normally annealing means a process in which the metal is heated to a high temperature. It is then slowly cooled to allow it to settle into its lowest energy state. SA uses the same approach. In analogy to the natural process, the distance function here is the energy function, a non-negative energy that is to be minimized. The energy depends on a set of parameters and then stochastically perturbs the variable set by a large amount at high temperature and by lower amounts at lower temperatures. If the perturbed variables increase the energy, the perturbation is either accepted or not accepted depending a stochastically determined probability distribution function governed by the temperature. At a high temperature, the probability of accepting an energy-increasing perturbation is high, and it decreases with the lowering of the temperature. The temperature is slowly decreased until a steady-state minimum is achieved. This is a simplified overview of SA [27].

To optimize the holographic reconstruction image, the random parameter used is the hologram pattern, and the energy function is the difference between calculated reconstruction image and desired image [26]. Figure 3.4.1-1 shows the basic calculation flow of simulated annealing. The process of simulated annealing can be explained as follows. At first, random binary phase hologram $phase_0(x,y)$ is prepared. In step 1, a pixel of random hologram is changed to another state. In step 2, reconstruction image of the hologram is calculated and compared to



(a)

for each temperature T , iteration t ,

for $x \Rightarrow Nx, y \Rightarrow Ny$

① $phase_1(x,y) = \text{abs}(phase_0(x,y) - \pi)$

② $I_t = \text{Fresnel Prop}\{z, phase_1\}$

③ $E_{\text{new}} = \text{norm}(I_{\text{desire}}^2 - I_t^2)$

④ **if** $\exp(E_{\text{best}} - E_{\text{new}}) / T > \text{rand}(0,1)$

⑤ $phase_0 = phase_1$

$E_{\text{best}} = E_{\text{new}}$

else

⑤' $phase_1 = phase_0;$

end

end

(b)

Fig. 3.4.1-1 Calculation flow of basic simulated annealing.

the desired pattern. The simulated reconstructed image is calculated by equation 3.3.1-9 and 3.3.1-10 with FFT. Calculated light field I_{new} is a two-dimensional reconstruction image of the binary phase hologram $phase_1(x,y)$. Error E_{new} is calculated as the difference between calculated light field I_{new} and desired light field (desired image) I_{desire} . In step 3, error E_{new} is compared to the old best error E_{best} . If the change in step1 is effective in reducing the error, the change is accepted. In the other case, the change in step1 is rejected per equation

$$P = \exp \frac{(E_{best} - E_{new})}{T}. \quad (3.4.1.-1)$$

Where P is probability of acceptance and T is a parameter that has the same meaning as temperature in the natural process of annealing. When T is high temperature or E_{new} is larger than E_{best} , but the difference small, the change in step 1 would be accepted with high probability. After these steps the next pixel would be changed and repeated under simulated annealing. In the SA process, acceptance probability P can prevent the error from converging to local minimum.

3.4.2 Parameters of simulated annealing

In this paper, pixel position was added as a parameter of SA. In the magneto-optic holographic three-dimensional display, control resolution of magnetic pixel position could be finer than pixel pitch, e.g., minimum magnetic pixel size was approximately 1 μm . In contrast, pixel position can be controlled with nanometer order by piezo stage. Figure 3.4.2-1 (a) shows the approach method of SA with pixel position control. In Fig.3.4.2-1, a size of minimum magnetic pixel is the same as 4×4 smaller pixels, and a smaller pixel means increased pixel position resolution. For the conventional SA method for generating a hologram, phases or intensity of pixel are used as parameters to change the initial hologram. In the case of a magnetic hologram, there are only two phases available as pixel states, which arise out of the directions of magnetization (Fig.3.4.2-2 (b)). The new method uses phase distribution in a cell instead of pixel phase. A cell was constructed out of 32 small pixels (the same area as two magnetic pixels), which implies control resolution of magnetic pixels; it had 16 states of phase distribution available when considering superposition (Fig. 3.4.2-2). The new SA methods could treat pixel size and pixel position the same way as the conventional method of SA, i.e., the SA algorithm chooses a state from within Fig. 3.4.2-2 at random, instead of changing the phase of pixels. The merit of this method was that we can handle pixel position controlled images as same as high resolution holograms.

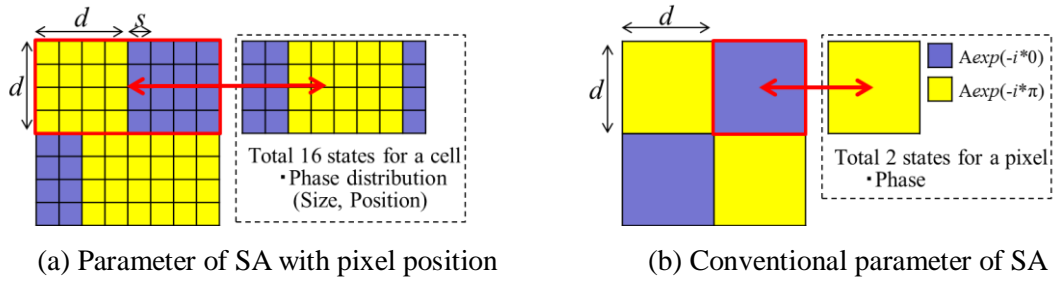


Fig. 3.4.2-1 SA approach for magneto-optic spatial light modulator (MOSLM).

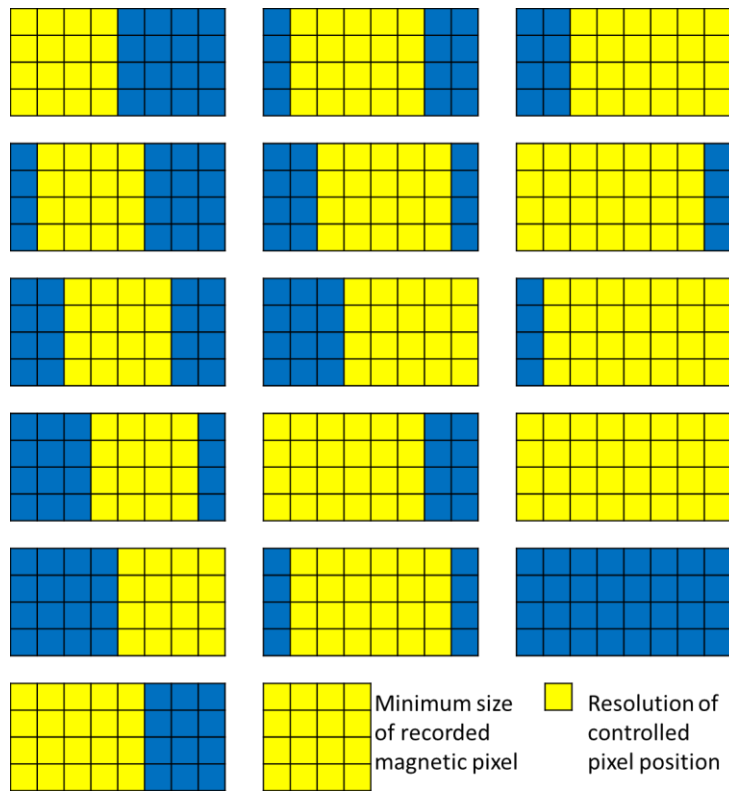


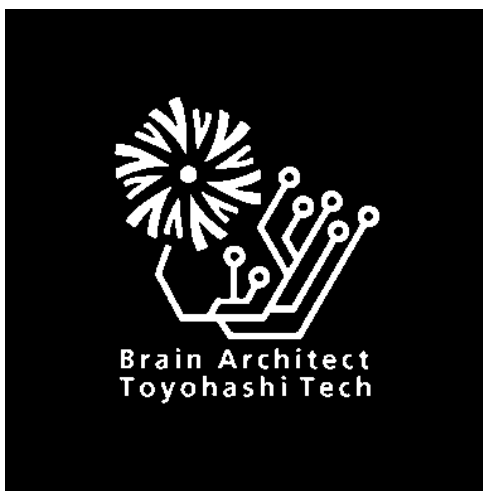
Fig. 3.4.2-2 Available states of a cell. Phase difference between yellow and blue pixel is 180° and yellow region means recorded magnetic pixels.

3.4.3 Comparison of error value

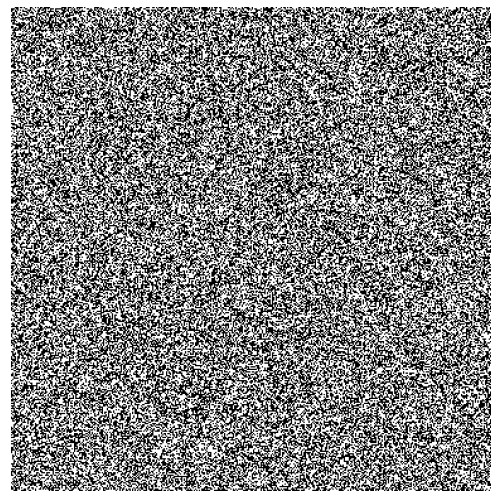
In proof of principle calculations, the magnetic pixel size d was $5.44 \mu\text{m}$ and the minimum position resolution was $1.36 \mu\text{m}$. The temperature parameter was changed 30 times, and calculations were repeated 4 times at each temperature to converge the error value in one temperature. The other calculation parameters are shown in table 3.4.3-1. Figure 3.4.3-1 shows the initial setup of SA with pixel position control. The desired pattern used 2D binary pattern (Fig. 3.4.3-1 (a)), and light distribution I_{desire} was provided by multiplying $\exp(-j\pi)$ to bright pixel. Each pixel of the initial random hologram (Fig 3.4.3-1 (b)) were represented as $A\exp(-j\pi)$ or $A\exp(j\pi)$, then A was adjusted to that both images got the same total light intensity. SA with pixel position control was computed with the above conditions, with 16 states from within Fig 3.4.2-2. To compare error value, conventional SA with the minimum unit of area of changing pixel as 4×4 pixels was computed under the same conditions.

Table 3.4.3-1 Calculation parameters.

Calculation area resolution	1536×1536 pixels
Minimum stage resolution	$1.36 \mu\text{m}$, 1×1 pixel
Minimum magnetic pixel size	$5.44 \times 5.44 \mu\text{m}$, 4×4 pixels
Propagation distance	6 mm
Light wavelength	532 nm
Temperature change	30 times
Iteration in each temp.	4 times



(a) Desired pattern



(b) Random binary hologram

Fig. 3.4.3-1 Initial setup of simulated annealing.

Figure 3.4.3-2 shows error value E_{best} with changing temperature. The error values of pixel position fixed SA converged faster than those of pixel position controlled SA. A reason for this result was the number of available combinations of holograms, which depends on the pixel resolution of the hologram. For the same reason, converged error value of the pixel position controlled SA was smaller than that of the conventional method. These results suggested that if a cell size within Fig.3.4.2-2 was enlarged, calculation result would reduce the error.

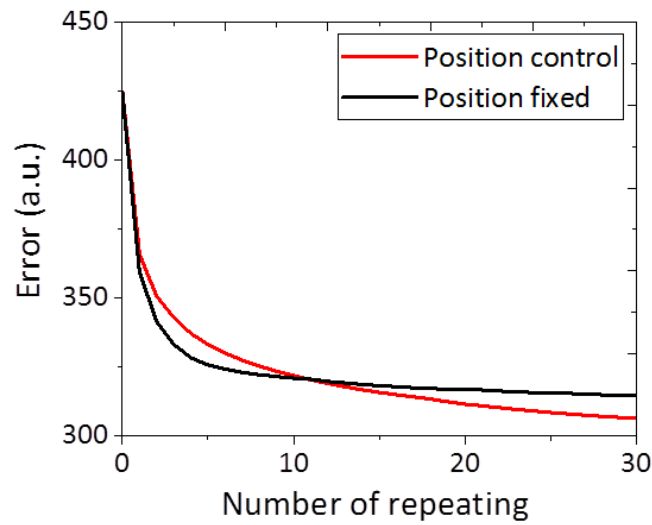
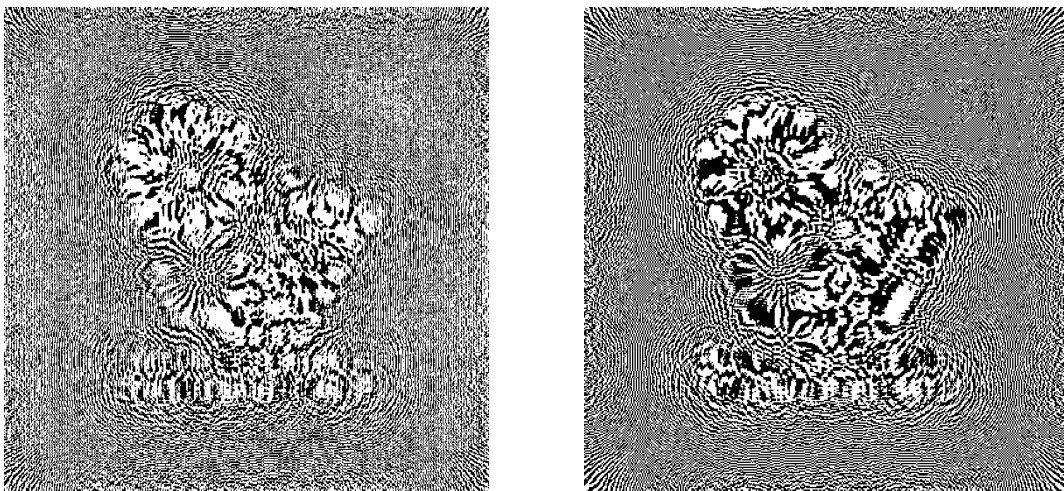


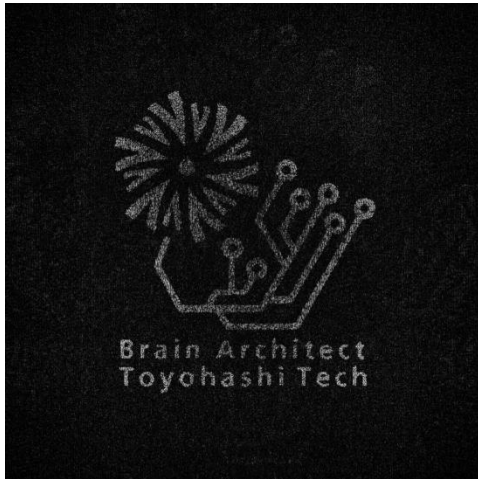
Fig. 3.4.3-2 Error value with changing temperature parameters.



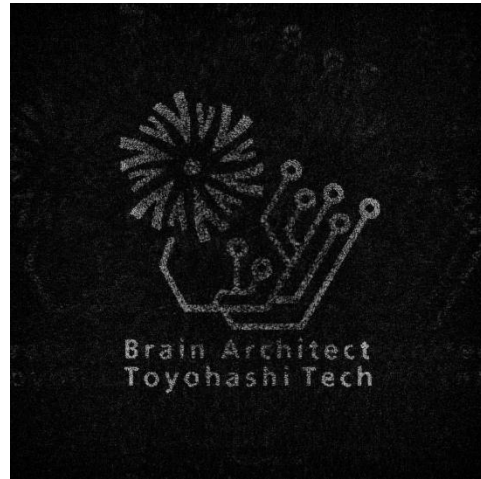
(a) with pixel position control

(b) with pixel position fix

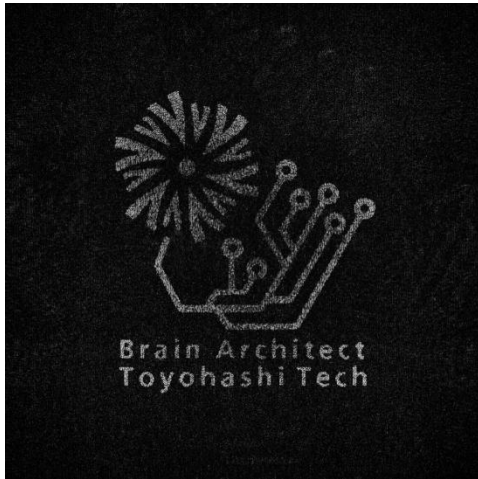
Fig. 3.4.3-3 Converged fringe pattern of both SA methods at temperature = 30.



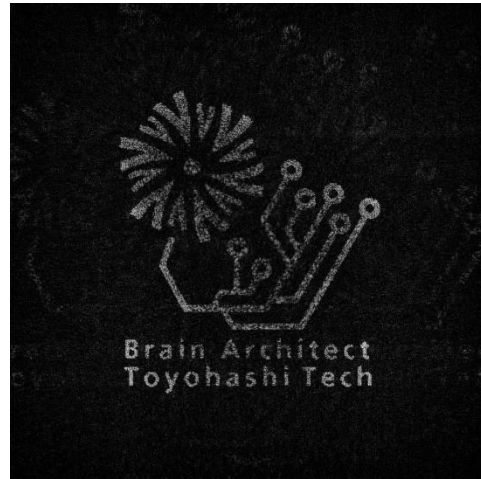
(a-1) At temperature = 5



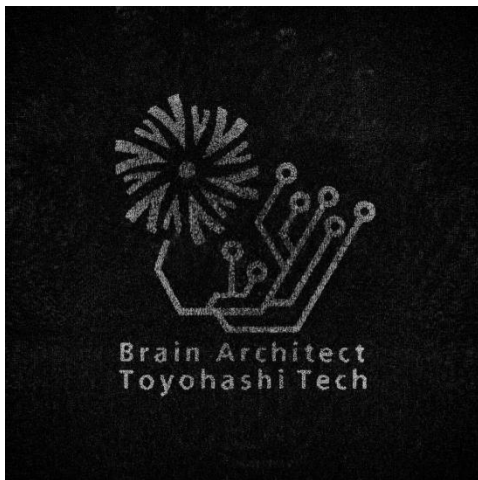
(b-1) At temperature = 5



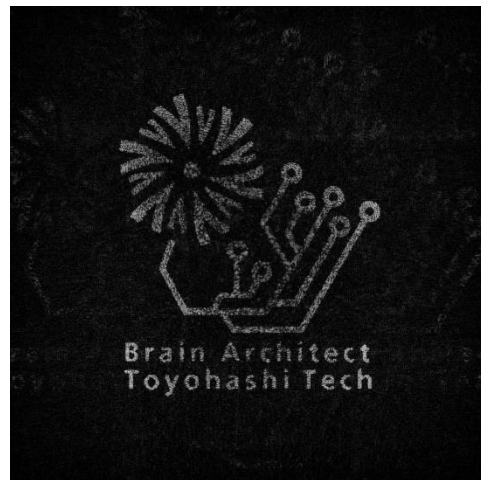
(a-2) At temperature = 11



(b-2) At temperature = 11



(a-3) At temperature = 30



(b-3) At temperature = 30

Fig. 3.4.3-4 Simulated reconstructed images of both SA methods, (a-1)~(a-3) were calculated by SA with pixel position control, (b-1)~(b-3) were by conventional SA.

3.5 Summary

Chapter 3 discusses calculation methods of computer generated holograms for magnetic holograms. The purpose of this chapter is improvement of reconstructed images by calculation method of CGHs. Calculation of object light propagation is especially important for increasing reconstructed image quality.

To calculate a complex object and its surface, the two-dimensional image based method was adopted. This method was suitable for generating a complicated hologram composed of many point light sources. Computing environments were constructed by MATLAB 2014b. In this method, 3D object data is sampled to some two-dimensional images, and light propagations from each plane to hologram plane are calculated. In addition, this method was found suitable for additional calculation of hologram such as occlusions. To add the occlusions to the CGHs, the polygon by polygon method was used.

In the next step, the reduction method of binarization error considering pixel position control was proposed. Holograms on magneto-optic holographic three-dimensional display were binary holograms, which were represented by perpendicular magnetization directions. The usual reconstructed images with binary holograms included binarization errors. Therefore, the study focused on ensuring that pixel position of magnetic hologram was not fixed mechanically. To reduce binarization errors, the pixel positions of computer generated holograms were considered using the simulated annealing (SA) method.

In the magneto-optic holographic three-dimensional display, control resolution of magnetic pixel position could be finer than pixel pitch. For example, the minimum magnetic pixel size was approximately 1 μm ; in contrast, pixel position could be controlled at the nanometer order by piezo stage. For conventional SA method of generating a hologram, phases or intensity of pixels are used as parameters for changing the initial hologram. In the case of magnetic holograms, the available states of pixels were only in two phases, which were produced by the directions of magnetization. In contrast, the new method used pixel position distribution in a cell, and the cell was used instead of pixel phase. A cell was constructed by 32 small pixels (the same area as two magnetic pixels) which means control resolution of magnetic pixel, and had 16 available states of phase distribution when considering superposition. The SA could treat pixel positions of magnetic hologram as a calculation parameter, and error value included in simulated reconstruction images were reduced.

References

- [1] K. Matsushima, S. Nakahara, Y. Arima, H. Nishi, H. Yamashita, Y. Yoshizaki, and K. Ogawa, "Computer holography: 3D digital art based on high-definition CGH," *J. Phys. Conf. Ser.*, vol. 415, p. 12053, 2013.
- [2] U. Schnars and W. Juptner, "Digital recording and numerical," *Inst. Phys. Publ.*, vol. 13, p. 17, 2002.
- [3] M. Daibo, "Visualization of x-ray computer tomography using computer-generated holography," *Proc. SPIE*, vol. 3457, no. July, pp. 134–145, 1998.
- [4] A. Koike, H. Morii, M. Yomori, Y. Neo, T. Aoki, and H. Mimura, "Full-color image reconstruction by holography for 3D x-ray CT," *Proc. SPIE*, vol. 7008, p. 70081H–1-70081H–8, 2008.
- [5] S. H. Lee, S. C. Kwon, H. B. Chae, J. Y. Park, H. Kang, and J. D. K. Kim, "Digital hologram generation for a real 3D object using by a depth camera," *J. Phys. Conf. Ser.*, vol. 415, no. 1, p. 12049, 2013.
- [6] O. Bryngdahl and A. Lohmann, "Single-Sideband Holography*," *J. Opt. Soc. Am.*, vol. 58, no. 5, p. 620, 1968.
- [7] T. Kurihara and Y. Takaki, "Improving viewing region of 4f optical system for holographic displays," *Opt. Express*, vol. 19, no. 18, p. 17621, 2011.
- [8] T. Mishina, F. Okano, and I. Yuyama, "Time-alternating method based on single-sideband holography with half-zone-plate processing for the enlargement of viewing zones.," *Appl. Opt.*, vol. 38, no. 17, pp. 3703–3713, 1999.
- [9] Y. Takaki and Y. Tanemoto, "Modified resolution redistribution system for frameless hologram display module.," *Opt. Express*, vol. 18, no. 10, pp. 10294–10300, 2010.
- [10] G. T. Nehmetallah, R. Aylo, and L. Willams, *Analog and Digital Holography with MATLAB*. SPIE, 2015.
- [11] J. P. Waters, "Holographic image synthesis utilizing theoretical methods," *Appl. Phys. Lett.*, vol. 9, no. 11, pp. 405–407, 1966.
- [12] H. Yoshikawa, T. Yamaguchi, and T. Miyahara, "Image type computer-generated hologram of shaded object," *Proc. - 9th IEEE/ACIS Int. Conf. Comput. Inf. Sci. ICIS 2010*, pp. 827–830, 2010.

- [13] Y. Ichihashi, H. Nakayama, T. Ito, N. Masuda, T. Shimobaba, A. Shiraki, and T. Sugie, “HORN-6 special-purpose clustered computing system for electroholography,” *Opt. Express*, vol. 17, no. 16, pp. 13895–13903, 2009.
- [14] K. Matsushima, H. Schimmel, and F. Wyrowski, “Fast calculation method for optical diffraction on tilted planes by use of the angular spectrum of plane waves.,” *J. Opt. Soc. Am. A*, vol. 20, no. 9, pp. 1755–1762, 2003.
- [15] K. Matsushima, “Computer holography: 3D imaging of virtual and real objects,” *SPIE Newsroom*, pp. 2–4, Apr. 2011.
- [16] T. Shimobaba, K. Matsushima, T. Kakue, N. Masuda, and T. Ito, “Scaled angular spectrum method,” *Opt. Lett.*, vol. 37, no. 19, p. 4128, 2012.
- [17] J. W. Goodman, *Introduction to Fourier Optics 3ed*, Third edit. 2005.
- [18] K. Matsushima and T. Shimobaba, “Band-limited angular spectrum method for numerical simulation of free-space propagation in far and near fields,” *Opt. Express*, vol. 17, no. 22, pp. 19662–19673, 2009.
- [19] R. H.-Y. Chen and T. D. Wilkinson, “Computer generated hologram with geometric occlusion using GPU-accelerated depth buffer rasterization for three-dimensional display.,” *Appl. Opt.*, vol. 48, no. 21, pp. 4246–4255, 2009.
- [20] K. Matsushima, M. Nakamura, and S. Nakahara, “Silhouette method for hidden surface removal in computer holography and its acceleration using the switch-back technique,” *Opt. Express*, vol. 22, no. 20, pp. 24450–24465, 2014.
- [21] Y. Takaki and N. Okada, “Hologram generation by horizontal scanning of a high-speed spatial light modulator,” *Appl. Opt.*, vol. 48, no. 17, p. 3255, 2009.
- [22] Y. Frauel, T. J. Naughton, O. Matoba, E. Tajahuerce, and B. Javidi, “Three-dimensional imaging and processing using computational holographic imaging,” *Proc. IEEE*, vol. 94, no. 3, pp. 636–653, 2006.
- [23] A. Kirk, K. Powell, and T. Hall, “A generalisation of the error diffusion method for binary computer generated hologram design,” *Opt. Commun.*, vol. 92, no. 1–3, pp. 12–18, 1992.
- [24] M. P. Chang and O. K. Ersoy, “Iterative interlacing error diffusion for synthesis of computer-generated holograms,” *Appl. Opt.*, vol. 32, no. 17, pp. 3122–3129, 1993.

- [25] B. R. Brown and A. W. Lohmann, "Computer-generated Binary Holograms*," *IBM J. Res. Dev.*, vol. 13, no. 2, pp. 160–168, 1969.
- [26] N. Yoshikawa and T. Yatagai, "Phase optimization of a kinoform by simulated annealing," *Appl. Opt.*, vol. 33, no. 5, pp. 863–868, 1994.
- [27] R. J. Ludman J., Caulfield H. J., *Holography for the New Millennium*. 2002.

4. Optical systems for holographic video

4.1 Introduction

This chapter discusses the construction of optical systems to represent holographic video using magnetic media. As discussed in chapter 2, magnetic holograms require a higher recording density compared to other light addressed spatial light modulators (SLMs) and other hologram media [1]–[6]. Therefore, an optical system was required for magneto-optic holographic three-dimensional display to obtain the energy density of recording light suitable for magnetic hologram recording. In the tiling optical system, a demagnification optical imaging system using objective lenses was used to decrease the magnetic pixel size, and to increase laser light energy density of recording light at the same time [7]. However, this method led to an increase in the scanning distance and an enlargement of the optical system using the imaging optical system.

This chapter deals with two optical systems as proof of principle of a magneto-optic holographic three-dimensional display. To demonstrate continuous recording and erasure of magnetic holograms, a demonstration optical system was constructed using an amorphous terbium iron film (*a*-TbFe) film and thermal assist. The *a*-TbFe film can record magnetic holograms with low recording light energy density, and thermal assist is a popular method for thermomagnetic recording to reduce recording energy. Holograms recorded on the *a*-TbFe film were erased by an external magnetic field, and the *a*-TbFe film was magnetized by the applied field again for recording more holograms. Coming up is an investigation of an optical system that can reduce the scanning distance to record the entire hologram and enable fast hologram recording using micro lens array.

Section 4.1 discusses the constitution of a holographic video system. Section 4.2 deals with the optical system to demonstrate continuously recording and erasure of magnetic holograms. Section 4.3 describes the optical system for new recording method with micro lens array.

4.2 Rewriting of magnetic holograms

4.2.1 Optical system for continuously recording and erasing magnetic holograms

To demonstrate holographic video using magnetic hologram media, an optical system was constructed for continuously recording and erasing magnetic holograms. Figure 4.2.1-1 shows the schematic image of the demonstration optical system. This optical system included a recording system, an erasure system, and a reconstruction system. The scanning system and demagnification of pixel size were not adopted.

Laser light generated by a Nd:YAG pulsed laser for recording was reshaped by lenses placed before a polarized beam splitter (PBS), and light power was adjusted by a half wavelength plate (HWP) and the PBS. Angle of light incident on the digital micro mirror device (DMD) was tilted after considering the micro mirror angle on the DMD, and reflected light axis was normal against the DMD plane. The DMD modulated the pulsed laser light to the hologram pattern. Modulated light patterns were transferred to magnetic media by two $4f$ -optical-systems without demagnification to obtain screen size. Then, high order diffracted light rays generated by DMD pixel structure were blocked by an iris. Reconstruction illumination light source used a CW laser with a wavelength of 637 nm. Optical axes of both lights were synthesized by dielectric mirror (DM). The color filter prevented recording light from reaching the observer. Another HWP on the optical axis of the illumination reconstruction light was adjusted to increase reflected light by the DM.

4.2.2 Magneto-optical properties of a -TbFe film with thermal assist

A a -TbFe film (substrate/SiN (20 nm)/ a -TbFe (50 nm)/SiN (50 nm)) was used as holographic media to demonstrate continuous recording and erasure of magnetic holograms. The optical imaging system used a $4f$ optical system without demagnification. Recording energy density was not enough to record the hologram on the BiDyYFeAlG because the optical imaging system could not increase the recording light energy density by condensing light. The other issue was that the coercivity of a -TbFe was approximately 1 kOe, which was difficult to control by external magnetic field with video framerate. This section discusses thermal assist of thermomagnetic recording to solve this problem.

A ceramic heater was used to control the a -TbFe film's temperature (Fig. 4.2.2-1). The ceramic heater was attached to the opposite side of the magnetic layer, with the substrate and copper plate in between. Copper plates had a window for incident reconstruction illumination light, to reconstruct magnetic hologram in transparent mode. The a -TbFe film inside the window was heated by heat transfer from the copper plate.

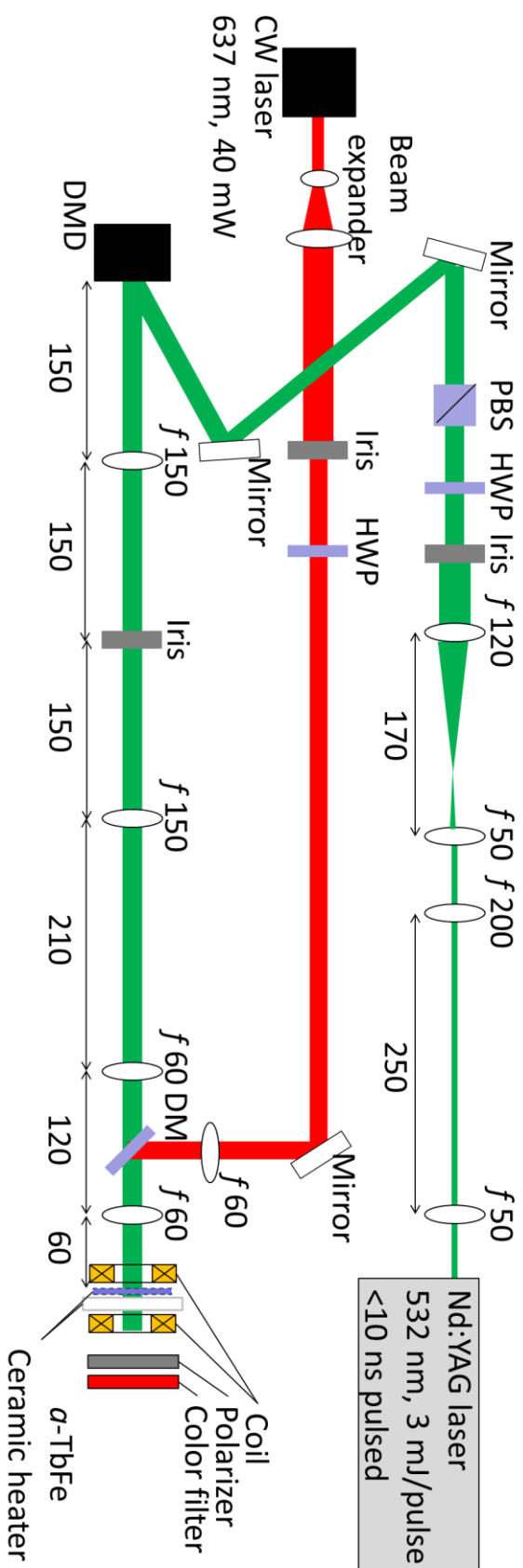


Fig. 4.2.1-1 Schematic image of optical system for continuously recording and erasure of magnetic hologram.

Thermal assist can reduce the recording energy density of thermomagnetic recording by reduction of required heating temperature. The coercivity of the magnetic film also decreases as it approaches the Curie temperature; the Faraday rotation angle of the magnetic films also reduces. To evaluate these reductions, magneto-optic (MO) loops of the α -TbFe were measured against various temperatures using the rotating analyzer method. The Kerr mode of measurement was chosen for obtaining the necessary transmitted light power. Figure 4.2.2-2 shows representative measurement results of MO Kerr loop for the α -TbFe film. These results were measured inside the window. At $T = 30\text{ }^{\circ}\text{C}$, the MO Kerr loop of the α -TbFe film maintained a good squareness ratio. The remanent Kerr rotation angle was reduced when increasing the heater temperature. Coercivity, which is defined as a magnetic field crossed to Kerr rotation angle zero, was also reduced.

Temperature dependence of the coercivity and remanent Kerr rotation angle is shown in Fig. 4.2.2-3. The coercivity of a α -TbFe film was decreased by increasing heater temperature. At a heater temperature of $90\text{ }^{\circ}\text{C}$, coercivity was approximately 70 Oe, or 7 % of the coercivity at room temperature. On the other hand, the remanent Kerr rotation angle at $90\text{ }^{\circ}\text{C}$ was approximately 50 % of rotation angle at the room temperature.

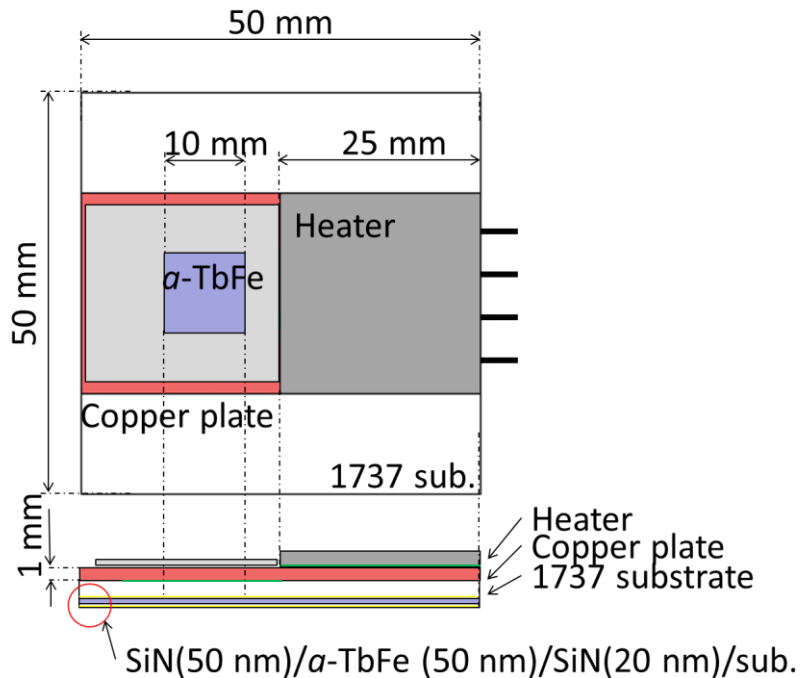


Fig. 4.2.2-1 α -TbFe film with ceramic heater

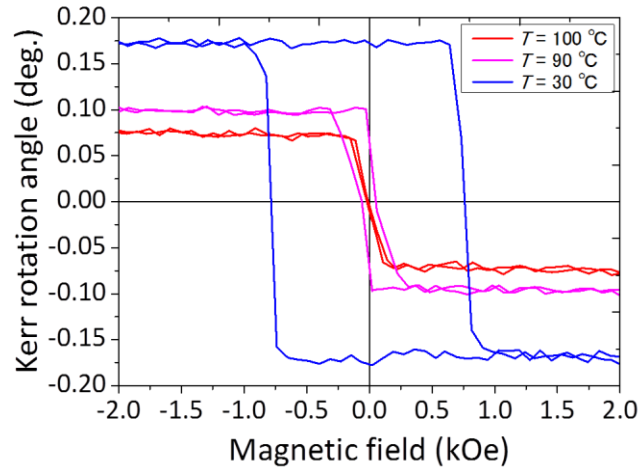


Fig. 4.2.2-2 Representative measurement results of MO Kerr loop; T is the heater temperature.

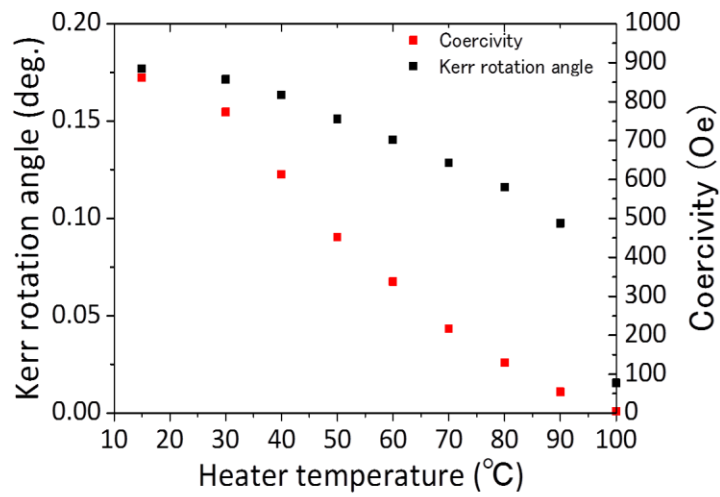


Fig. 4.2.2-3 Temperature dependence of remanent Kerr rotation angle and coercivity.

4.2.3 Continuously recording and erasure of magnetic hologram

(a) Confirming of thermomagnetic recording

Recording area and resolution of thermomagnetic recording with thermal assist were examined by using two test patterns. The first pattern, shown in Fig. 4.2.3-1, was used to measure recorded area with changing assist temperatures. A white or black block square was 8×8 pixels, the pixel size was $13.8 \mu\text{m}$, and the image size was $6 \times 6 \text{ mm}^2$. The test pattern was recorded by the optical system shown in Fig 4.2.1-1. Recorded areas were measured against each heater temperature by using the number of squares and plotted in Fig. 4.2.3-2. Recorded area was increased by raising heater temperature. This area increase caused laser power distribution. At over $100 \text{ }^\circ\text{C}$, magnetic pattern was not recorded because coercivity and remanent magnetization to keep magnetic information were very small. The largest recorded area was approximately 90 % of original image size, and square area was approximately 380×380 pixels. To evaluate recording resolution, the second pattern was recorded on a α -TbFe film with a thermal assist temperature of $88 \text{ }^\circ\text{C}$. Figure 4.2.3-3 shows the second test pattern and its recorded magnetic pattern. Magnetic pixel size was $13.6 \mu\text{m}$, which was the same size as the DMD. From these results, thermal assist condition was determined as the heater temperature being $90 \text{ }^\circ\text{C}$.

(b) Synchronization of recording and erasure

To erase the magnetic pattern, a magnetic field was applied using two coils. Figure 4.2.3-4 shows the overview of the erasure system. The number of turns of each coil was 210. Magnetic flux densities against electric currents were measured in the middle, between two coils. Measurement results of applied magnetic flux densities are shown in Fig.4.2.3-5. The coil system could apply over 400 G with 6 A. According to Fig.4.2.2-2, the magnetic field was sufficient to magnetize the α -TbFe film heated $90 \text{ }^\circ\text{C}$.

To demonstrate a holographic video, synchronization of recording and erasure systems was necessary, and the timing of recording was determined by pulsed laser. The Nd:YAG laser, which generated recording light, generated the trigger signal synchronized to laser pulse output. The recording laser pulse (wavelength 532 nm, pulse width 10 ns, repetition frequency 10 Hz) was synchronized to the representation of DMD by the trigger signal. After recording, an external magnetic field (400 Oe) was applied to erase the magnetic hologram. Figure 4.2.3-6 shows the timing chart of the demonstration system. The process of reconstruction of one frame has been described below. One magnetic hologram, which was recorded by pulsed laser, reconstructed 3D images until the magnetic field was being applied. After the recording, holograms on DMD would be changed to the next frame immediately. Reconstruction illumination light was always irradiated. The holographic video—a rotating wireframe

cube—was displayed using the optical system; the framerate was 10 fps, 13.6 $\mu\text{m}/\text{pixel}$, 367 \times 367 pixels (Fig.4.2.3-7).

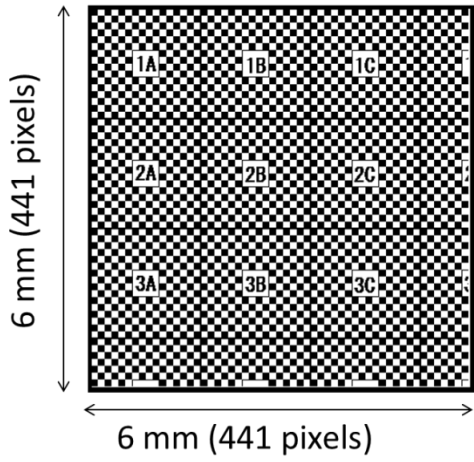


Fig. 4.2.3-1 Test pattern to confirm the recorded area.

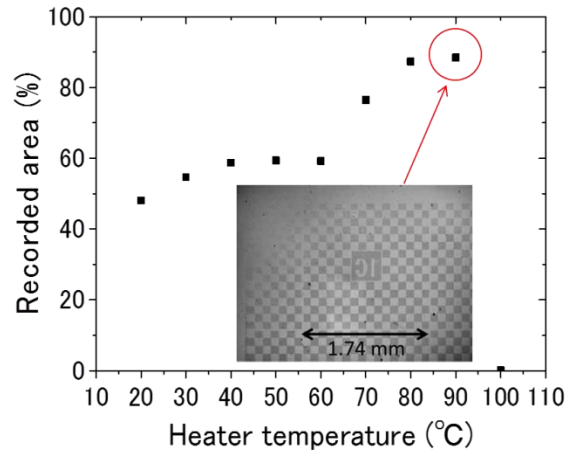
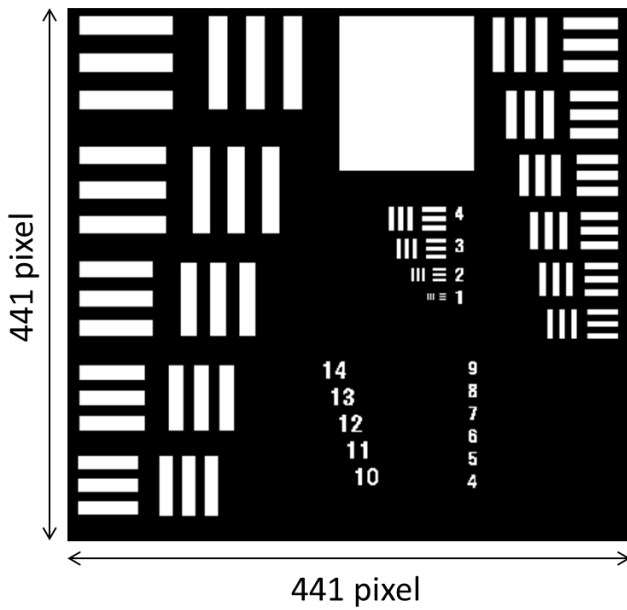
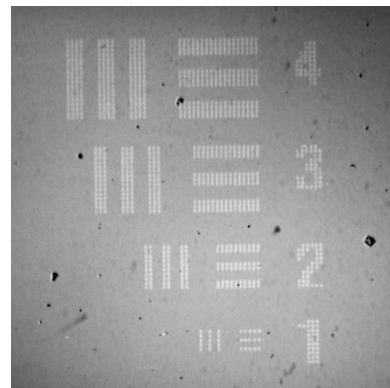


Fig. 4.2.3-2 Recorded areas against heater temperatures.



(a)



(b)

Fig. 4.2.3-3 Test pattern for thermomagnetic recording, (a) is the original image, and (b) is the center of the recorded area. Numbers means the number of pixels of short axis of lines.

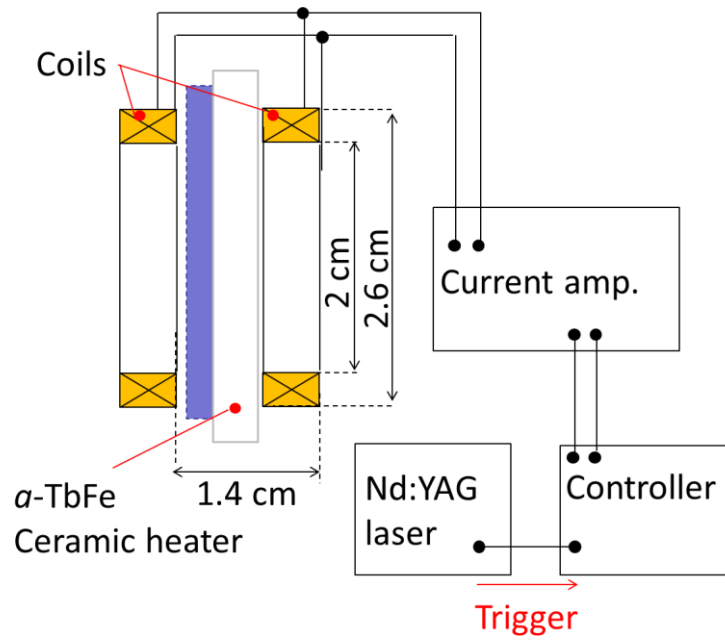


Fig. 4.2.3-4 Overview of erasure system.

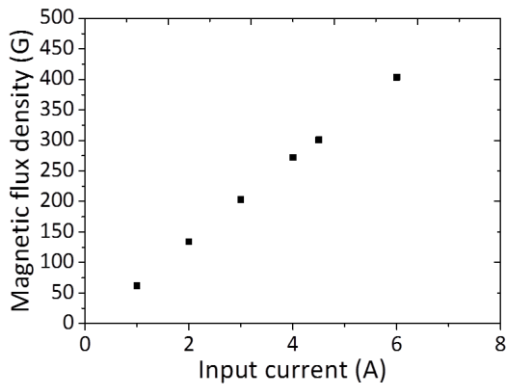
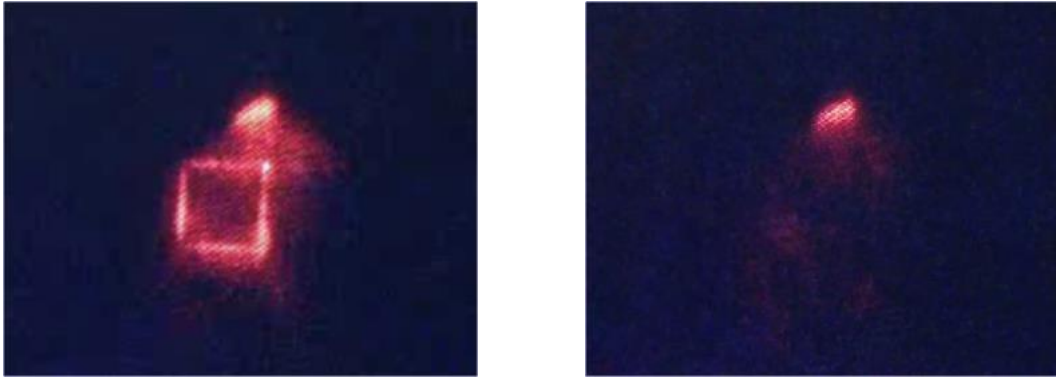


Fig. 4.2.3-5 Magnetic flux densities against electric current.



Fig. 4.2.3-6 Timing chart of the demonstration system to reconstruct 10 fps holographic video.



(a) Reconstructed image

(b) Erasure of magnetic hologram

Fig. 4.2.3-7 Demonstration of refresh and re-write of magnetic hologram.

4.3 Optical system with micro lens array for holographic video

Section 4.2 discusses and demonstrates continuous recording and erasure of magnetic holograms. However, the viewing-angle of the reconstructed holographic video was narrow because the magnetic pixel size was the same as the pixel size of the DMD. To enlarge viewing-angle of reconstructed images, downsizing the magnetic pixels is important. In previous works, magnetic holograms were recorded via the tiling optical system. However, it took over 15 minutes to record a magnetic hologram. To solve this problem, a new optical system was proposed in this paper, which consists of a micro lens array instead of objective lens system in the tiling optical system.

This section deals with the optical addressing method with micro lens array for recording wide-viewing-angle holograms.

4.3.1 Recording algorithm

Figure 4.3.1-1 shows the recording principle of an optical system with micro lens array. Position of the micro lens array should be adjusted to obtain pixel matching to the DMD's pixels. In this system, magnetic pixels were fabricated with the same number of micro lenses for one shot of pulsed laser; the distance of each pixel was dependent on lens pitch. Black pixels in Fig. 4.3.1-1 meant recorded pixels from one shot of pulsed laser. Recorded pixels could fill the whole area of the hologram with one axis scanning, according to the broken line. The recorded magnetic pattern area was almost the same area as the SLM used to record it. Tilting angle θ could be written as

$$\theta = \sin^{-1} \frac{d_{\text{mag}}}{d_{\text{SLM}}}. \quad (4.3.1-1)$$

The number of recording pixels N_{pixel} by a pair of a micro lens and an SLM pixel could be calculated by

$$N_{\text{pixel}} = \left(\frac{d_{\text{SLM}}}{d_{\text{mag}}} \right)^2, \quad (4.3.1-2)$$

then, total scanning length could be represented as

$$L = N_{\text{pixel}} d_{\text{mag}}. \quad (4.3.1-3)$$

According to these equations, the tilting angle to record magnetic hologram with 1 μm pixels by using DMD was 4.2° , the number of recording pixels by an SLM pixel was 196 times, and the total scanning length was approximately 196 μm . Table 4.3.1-1 shows a comparison of the scanning distance and the required scanning speed between tiling and the new recording method. These values represent the conditions for a holographic video with $10 \times 10 \text{ mm}^2$ screen and framerate 5 fps. The mechanical stage of the tiling optical system had to move a long distance for each recording of a part of the hologram. In contrast, the new method with micro lens array had to move the same distance as the magnetic pixel size for each recording, and could reduce the scanning distance that was required to record a DMD-sized hologram with fine pixels. That is the new method with micro lens array, which can record magnetic holograms more efficiently against scanning length.

Table 4.3.1-1 Comparison of required speed and distance for mechanical stages.

	Micro lens method	Tiling optical system
Display area	$10 \times 10 \text{ mm}^2$	$10 \times 10 \text{ mm}^2$
Frame rate	5 fps	5 fps
Moving distance per 1 frame	200 μm	120 mm
Required driving speed	1 mm/s	600 mm/s

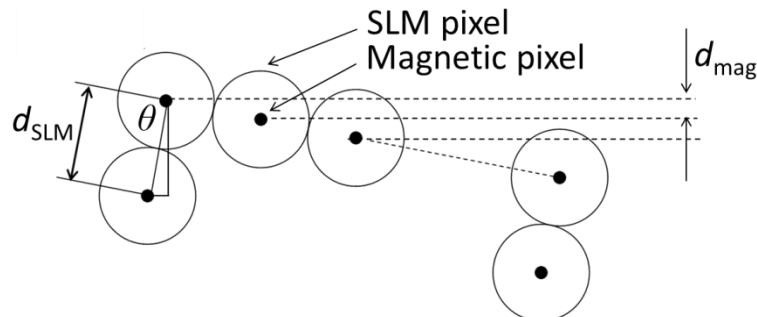


Fig. 4.3.1-1 Schematic image of recording optical system with micro lens array. Incident light for each SLM pixel was condensed to each focus point by micro lens array.

4.3.2 Overview of optical system

To demonstrate thermomagnetic recording of an optical system with micro lens array, an Nd:YAG pulsed laser (wavelength 532 nm, repetition rate 1.4 kHz, pulse width 25 ns) was used as the recording light source. The pulsed laser was expanded by two achromatic lenses, and was incident to the DMD. In this optical system, a $4f$ optical system was used to transfer modulated light distribution on the DMD to micro lens array. The $4f$ optical system was used to make the optical path for incident light to the DMD. If a transparent type of SLM was used, the micro lens array could be placed on top of the SLM. For using a micro lens array, pixel matching to micro lens array and DMD was important to record accurate patterns. The pixel matching between DMD and micro lens array was aligned by checking the transparent light distribution after the micro lens array. For alignment, a latticed pattern that can easily recognize a mismatch was used.

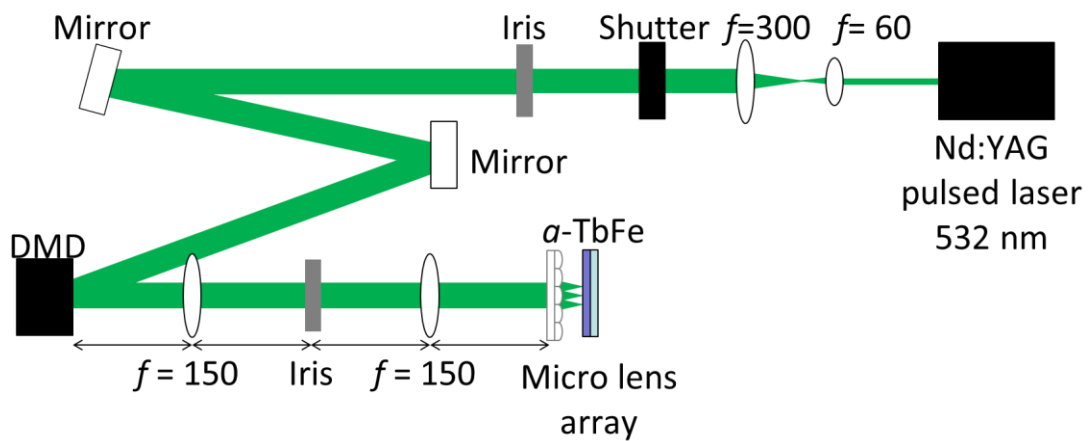


Fig. 4.3.2-1 Schematic image of the optical system with micro lens array for holographic video.



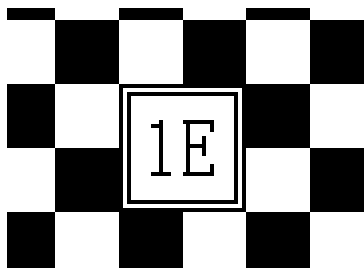
Fig. 4.3.2-2 Alignment pattern to match pixel position; the circular pattern is derived from micro lens.

Figure 4.3.2-2 shows the transparent light image captured by CCD camera. The position of the a -TbFe film was adjusted to the focal length of micro lens array by checking the reflected light from the film at the iris position.

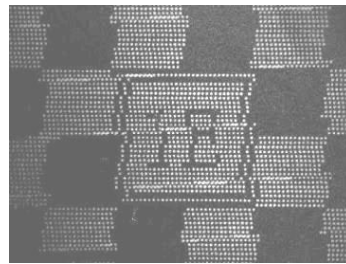
4.3.3 Recording of arbitrary image

As proof of principle, an arbitrary pattern was recorded on the a -TbFe film by the optical system via a micro lens array. The micro lens array had a lens pitch of $120\ \mu\text{m}$ and $8\ \mu\text{m}$ sized fabricated magnetic pixels. The micro lens array could record 85×85 magnetic pixels by a laser pulse. After recording by one shot laser pulse, the magnetic media was moved to the next position by x stage, and magnetic pixels were recorded by the same process. By repeating this process, an arbitrary pattern of central of recorded patterns was obtained. The total resolution of the recorded pattern was 1250×1250 pixels. Figure 4.3.3-1 (a) shows a part of the original pattern, and (b) shows the recorded pattern.

Displacements of recorded patterns were caused by a mismatch between DMD pixel pitch and lens pitch of micro lens array. To recude the dispancemnts, distance between each black pixels in Fig. 4.3.1-1 should be an integral multiple of magnetic pixel size. In addition, the distance of black pixels should be constant in all regions. Although displacements existed, this result proved that an optical system with micro lens array could record arbitrary patterns on magnetic media.



(a) A part of original image



(b) Recorded pattern

Fig. 4.3.3-1 Optical addressing with micro lens array and an axis scanning.

4.3 Summary

Chapter 4 discusses an optical system for holographic video system and demonstrates a holographic video on magnetic medium with narrow viewing angle. The holographic video system consisted of three elements—hologram recording system, hologram reconstruction system, and an erasure system of the magnetic hologram. Synchronization of recording, and construction of erasure systems was done to demonstrate holographic video, and timing of recording was determined by a pulsed laser. Recording laser pulse (wavelength 532 nm, pulse width 10 ns, repetition frequency 10 Hz) was synchronized to the representation of digital micro mirror device (DMD) by the trigger signal. After recording, external magnetic field (400 Oe) was applied to erase the magnetic hologram. Then, to reduce recording energy and coercivity of magnetic media, the *a*-TbFe media was heated by ceramic heater. The recorded area on the *a*-TbFe film was increased by raising the heater temperature. This area increase caused laser power distribution. At over 100 °C, magnetic pattern was not recorded because coercivity and remanent magnetization to keep magnetic information were very small. The recorded square area was approximately 380 × 380 pixels. Then, magnetic pixel size was 13.6 μm, which was same size as the DMD. From these results, the thermal assist condition determined was that the heater temperature needs to be 90 °C. By using the optical system and the *a*-TbFe film the holographic video—a rotating wireframe cube—was displayed using the optical system; the framerate was 10 fps, 13.6 μm/pixel, 367 × 367 pixels. In addition, the new hologram recording system used a micro lens array matching the DMD pixels to reduce scanning length.

In previous works, magnetic holograms with tiny pixels were recorded using a tiling optical system. However, it took over 15 minutes to record a magnetic hologram (in case of 10000 × 10000 pixels). To solve this problem, a new optical system is proposed in this paper, which consists of a micro lens array instead of objective lens system in the tiling optical system. Position of the micro lens array should be adjusted to obtain pixel matching to the DMD's pixels. In this system, magnetic pixels were fabricated using the same number of micro lenses for one shot of pulsed laser, then the distance of each pixel was determined depending on lens pitch. Fabricated pixels could fill the whole area of the hologram with axis scanning. This method could reduce the scanning distance that was required to record a DMD-sized hologram with fine pixels.

As proof of principle, a pattern was recorded on magnetic medium using the optical system of a micro lens array with lens pitch 120 μm and size of fabricated magnetic pixels 8 μm. 85 × 85 pixels were fabricated by a laser pulse. The total resolution of recorded pattern was 1250 × 1250 pixels. Although displacements existed, this result means that an optical system with micro lens array could record arbitrary patterns on magnetic media.

References

- [1] G. Moddel, K. M. Johnson, W. Li, R. A. Rice, L. A. Pagano-Stauffer, and M. A. Handschy, “High-speed binary optically addressed spatial light modulator,” *Appl. Phys. Lett.*, vol. 55, no. 6, pp. 537–539, 1989.
- [2] Y. Igasaki, F. Li, N. Yoshida, H. Toyoda, T. Inoue, N. Mukohzaka, Y. Kobayashi, and T. Hara, “High Efficiency Electrically-Addressable Phase-Only Spatial Light Modulator,” *Opt. Rev.*, vol. 6, no. 4, pp. 339–344, 1999.
- [3] S. Tay, P. Blanche, R. Voorakaranam, A. V. Tunç, W. Lin, S. Rokutanda, T. Gu, D. Flores, P. Wang, G. Li, P. St Hilaire, J. Thomas, R. a Norwood, M. Yamamoto, and N. Peyghambarian, “An updatable holographic three-dimensional display.,” *Nature*, vol. 451, no. 7179, pp. 694–698, 2008.
- [4] P. Blanche, A. Bablumian, R. Voorakaranam, C. Christenson, W. Lin, T. Gu, D. Flores, P. Wang, W.-Y. Hsieh, M. Kathaperumal, B. Rachwal, O. Siddiqui, J. Thomas, R. A. Norwood, M. Yamamoto, and N. Peyghambarian, “Holographic three-dimensional telepresence using large-area photorefractive polymer.,” *Nature*, vol. 468, no. 7320, pp. 80–83, 2010.
- [5] K. Buse, A. Adibi, and D. Psaltis, “Non-volatile holographic storage in doubly doped lithium niobate crystals,” *Nature*, vol. 393, no. 6686, pp. 665–668, 1998.
- [6] H. Horimai, X. Tan, and J. Li, “Collinear holography,” *Appl. Opt.*, vol. 44, no. 13, p. 2575, May 2005.
- [7] H. Takagi, K. Nakamura, S. Tsuda, T. Goto, P. Boey Lim, and M. Inoue, “Magneto-optic Three-Dimensional Holographic Display with Tiling Optical Addressing Method,” *Sensors Mater.*, vol. 27, no. 10, pp. 1003–1008, 2015.

5. Representing method of color and gray holograms

5.1 Introduction

Previous chapters developed the magneto-optic holographic three-dimensional display to represent holographic video with monochrome and monotone. However, to put it to practical use, colorization and multilevel gradations of reconstruction images need to be discussed. This chapter discusses the colorization and multilevel gradations representing methods of magnetic holograms.

To visualize a full color image, three primary color images should be synthesized either temporally or spatially. For a green color image, bismuth, dysprosium, and aluminum substituted yttrium iron garnet (BiDyYFeAlG) was used to increase diffraction efficiency, as described in chapter 2 [1]. However, it is difficult to obtain high diffraction efficiency in the entire visible light region with a single magnetic film. This is because magnetic garnet films such as BiDyYFeAlG have wavelength dependence and thickness dependence of magneto-optical properties [2], [3]. Therefore, this paper focuses on the optical space division method, which could use some independent spatial light modulators (SLMs) for each color [4]–[6]. This study designs three different thickness films to reconstruct each color image, and reconstructs three-dimensional (3D) images with red, green, and blue (RGB) full color. Section 5.2 is constructed in three parts to visualize full color images from magnetic holograms; media structure and their magneto-optical and optical properties, the optical system to visualize full color images, and representation of intermediate colors by synthesizing three primary single color images.

Multilevel gradation of reconstructed light intensity was also important for increasing holographic image quality [7]–[9]. The magneto-optic holographic three-dimensional display had binary pixels at initial state or recorded magnetization state. However, binary pixels could not reconstruct high quality 3D images because of quantization errors [9]. Apart from the optimization of the binary hologram discussed in chapter 3, the modulation of Faraday rotation angle of magnetic pixel by light energy density was investigated as a representation method of multilevel gradation. Section 5.3 investigated the relationship between recording light energy density and pixel depth, modulation of diffraction efficiency corresponding to Faraday rotation angle of recorded magnetic pixels, and reconstruction of 3D image with different levels of brightness from magnetic media.

5.2 Colorization of reconstructed image

5.2.1 Wavelength dependence of brightness

This section enlarges the relationship between the brightness and diffraction efficiency already discussed in chapter 2 to include colorized magnetic hologram images. Equation 2.2.3-3 was rewritten as follows in consideration of relative visibility.

$$B = \frac{683V}{2\pi\left(1-\frac{\cos\theta}{2}\right)} W. \quad (5.2.1-1)$$

Where V is the relative visibility; human vision has clear wavelength dependence in the visible wavelength region, and the comparison of luminosity to the wavelength of light is expressed by the relative value when the maximum sensitivity is 1, that is, relative visibility [10]. Fig. 5.2.1-1 shows the wavelength dependence of relative visibility.

Other important factors were wavelength dependences of magneto-optical and optical properties of BiDyYFeAlG film. Figure 5.2.1-2 shows calculated transmittance, Faraday rotation angle, and diffraction efficiency of the BiDyYFeAlG film (1 μm thickness) corresponding to the wavelength. Faraday rotation angle and transmittance were calculated by the matrix approach method [11], [12]. The brightness of the BiDyYFeAlG film was calculated by using the diffraction efficiency and equation 5.2.1-1, and the result is shown in Fig.5.2.1-3.

It was shown that sufficient brightness can be obtained in the green region. On the other hand, the transmittance decreased in the blue region, and the Faraday rotation decreased in the red region. Therefore, for colorization of holographic images, magnetic films need designed thickness for each color, and the optical space division method was adopted to colorize reconstructed images of magnetic holograms.

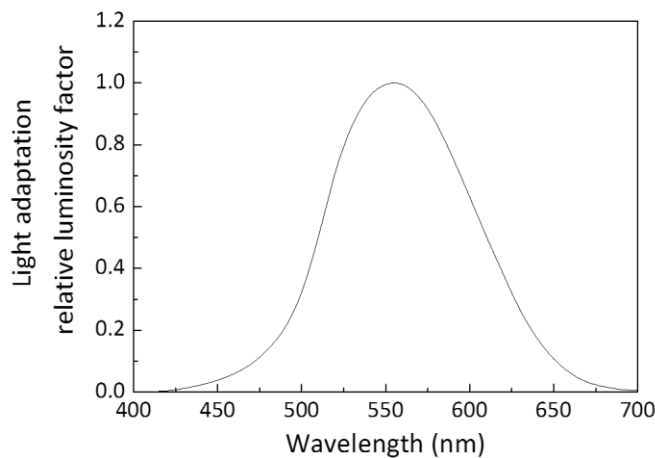


Fig. 5.2.1-1 The wavelength dependence of relative visibility [10].

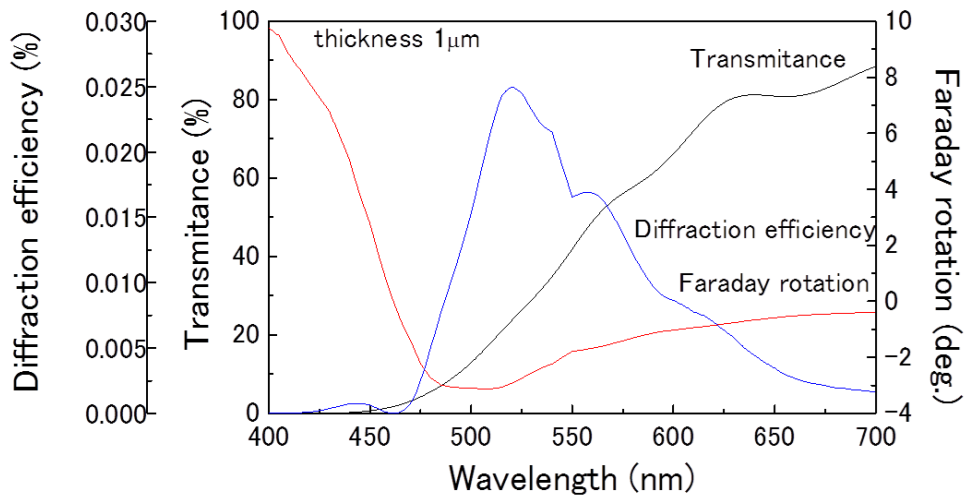


Fig. 5.2.1-2 The wavelength dependence of BiDyYFeAlG properties.

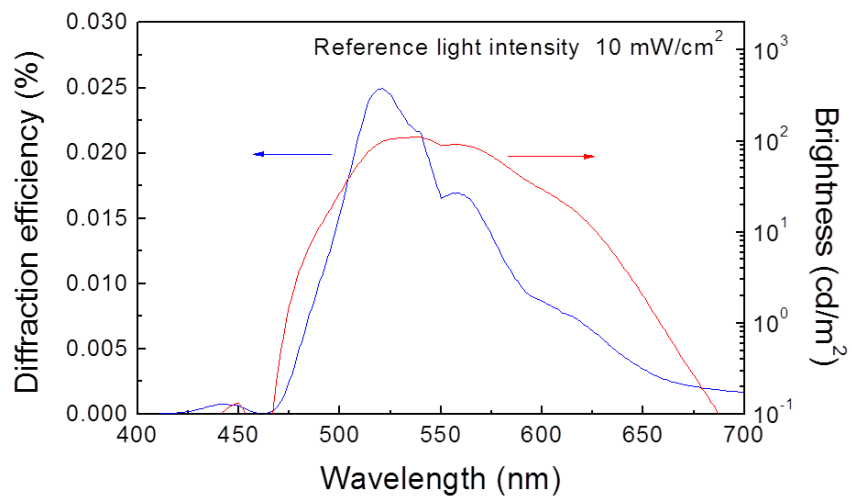


Fig. 5.2.1-3 Theoretical diffraction efficiency and brightness corresponding to wavelength.

5.2.2 Magnetic films for each color

As discussed in chapter 2, the magneto-optical and optical properties of BiDyYFeAlG films depend on their thickness. Therefore, the thickness of BiDyYFeAlG films were designed for each color. Figure 5.2.2-1 shows calculated diffraction efficiency versus thickness for each color. For green and red colors, BiDyYFeAlG thickness was limited by maximum depth of thermomagnetic recording [13]. These films obtained over 100 cd/m² brightness when the reference light intensity is 25.2 mW/cm². Unlike red and green, the thickness of BiDyYFeAlG film for blue color, which is low diffraction efficiency, was selected as maximal value of diffraction efficiency. Table 1 shows diffraction efficiency and thickness for each color. The diffraction efficiency was $0.19 \times 10^{-2} \%$ at 370 nm thickness for 450 nm wavelength, $2.81 \times 10^{-2} \%$ at 1,200 nm thickness for 532 nm wavelength, and $3.12 \times 10^{-2} \%$ at 2,600 nm thickness for 633 nm wavelength.

Table 5.2.2-1 Characteristics of BiDyYFeAlG films.

Wavelength	Calculation			Experiment		
	633 nm	532 nm	450 nm	633 nm	532 nm	450 nm
Thickness (nm)	2600	1200	370	2600	1200	580
Transmittance (%)	69.9	24.9	13.9	59.9	40.0	6.1
Faraday rotation angle (deg.)	1.90	3.02	1.05	1.31	2.34	1.65
Diffraction efficiency ($\times 10^{-2} \%$)	3.12	2.81	0.19	1.25	2.70	0.21

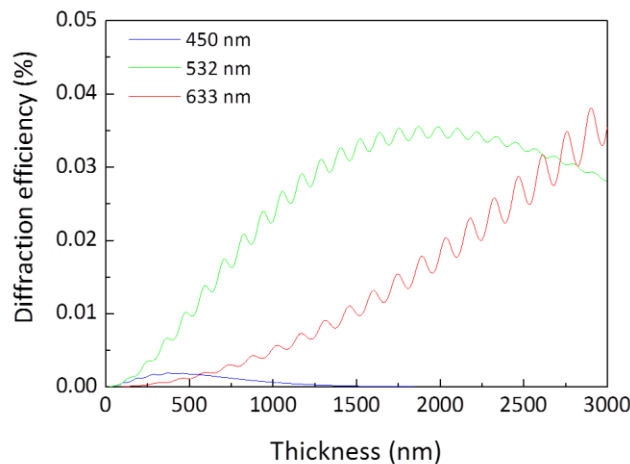


Fig. 5.2.2-1 Theoretical diffraction efficiencies corresponding to thickness of BiDyYFeAlG film for each color that is 450 nm, 532 nm, and 633 nm wavelength.

These designed BiDyYFeAlG films were fabricated by radio frequency ion beam sputtering. Table 1 shows characteristics of BiDyYFeAlG films. The diffraction efficiency of blue and green colors was almost the same as the calculated values. BiDyYFeAlG film for red color is different from the calculated value because of composition deviation.

5.2.3 Optical space division method

The optical space division method can reconstruct the full-colored images by synthesizing reconstructed images of each color. This method uses some SLMs to show single color components of a full-colored image [4]–[6]. In this study, three primary-colored reconstructed images were synthesized to represent magnetic holographic images with intermediate colors.

Fig.5.2.3-1 shows the optical system of optical space division method used to visualize color images. This optical system has three light sources for each color, spatial filter for correcting beam shape, beam expander for expansion of display area, three BiDyYFeAlG films to represent each color image, and polarizers to obtain linearly polarized light and decrease of intensity of 0th order transmitted light, charge-coupled device (CCD) with standard RGB (sRGB) for getting 3D images. The illumination light sources were CW lasers whose maximum intensity was 1,120 μW at 450 nm, 160 μW at 532 nm, and 530 μW at 633 nm for 100 cd/m^2 . The polarizers with cross-Nicol configuration passed only diffracted light and cut no modulation 0th order transmitted light for clear reconstruction images without 0th order

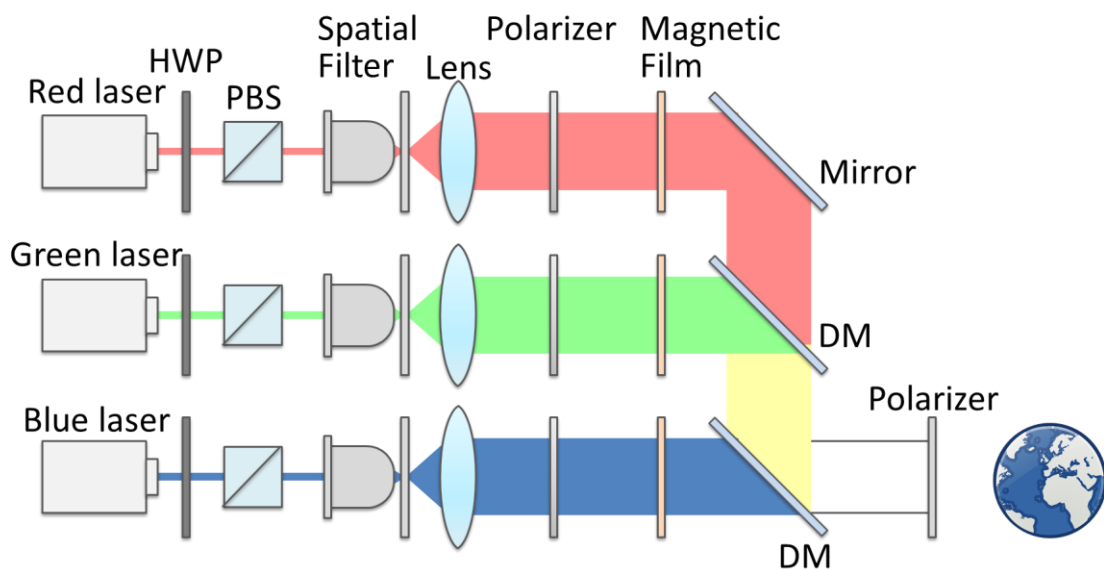


Fig. 5.2.3-1 Schematic image of optical system of optical space division method.

transmitted light, because the polarization angle of reconstructed light from magnetic hologram was rotated 90 degrees from incident light due to the magneto-optic effect.

5.2.4 Reconstruction of color image

To evaluate color modulation with the optical space division method, two single-colored images were synthesized to visualize intermediate colors. Figure 5.2.4-1 shows a model of the reconstructed image for each color. Each model contained a square with 2 mm sides. The distance between the magnetic hologram and the square was 20 mm. Hologram patterns of these models were obtained by half zone plate method for each color [14].

This study confirmed that the display color can be controlled gradually by the intensity ratio of the illumination light; the two colors were synthesized with three patterns of R-G, G-B, and R-B. The illumination light intensity was modulated at 6 gradations per color in the range of R: 0 to 500 μW , G: 0 to 250 μW , and B: 0 to 1200 μW . Reconstructed and synthesized images were captured with a CCD camera conforming to the sRGB standard. Captured images were plotted on Fig.5.2.4-2. Intermediate colors were represented by synthesizing two primary colors. When the illumination light intensity of one of the two synthesized colors was 0 μW , the colors of the synthesized image were changed depending on the illumination light intensity of the other light source, and the brightness was gradually changed. By synthesizing each single-color image with different brightness, it was confirmed that the display color is gradationally controlled by the ratio of the illumination light intensities.

A white color image could be also represented by illumination light intensity modulations; ratio of light intensity of each reconstructed image was blue: green: red = 0.66: 0.92: 1.00, where reconstructed light intensities were adjusted by varying the illumination light intensities. Fig.5.2.4-4 shows the gamut of reconstructed plate images. Primary colors of blue,

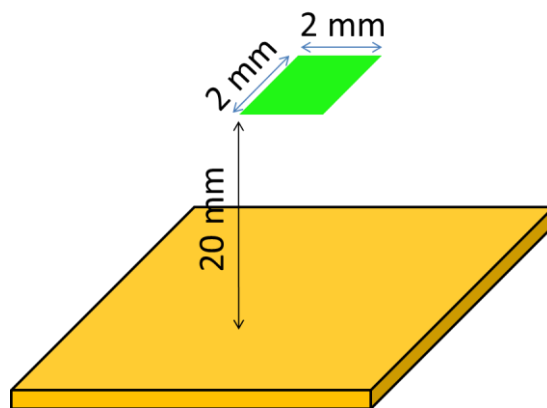
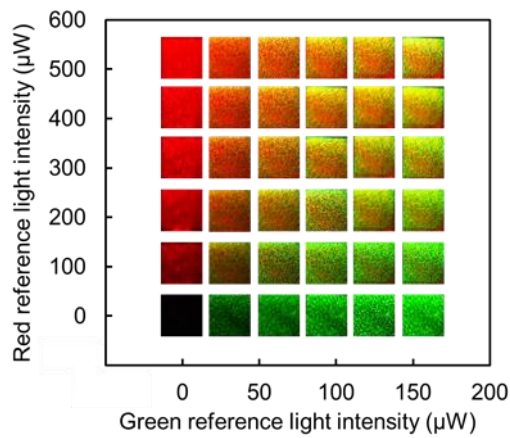
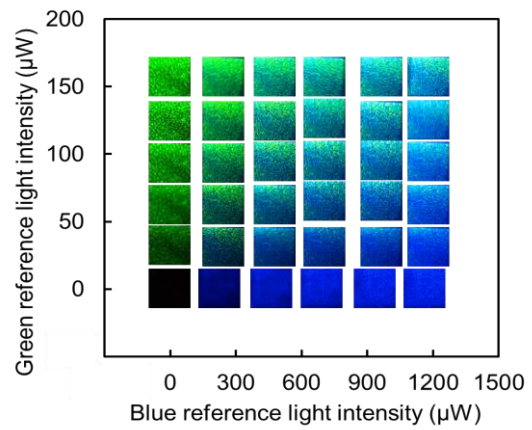


Fig. 5.2.4-2 Plate image model used to visualize intermediate colors by synthesizing reconstructed image with other colors.

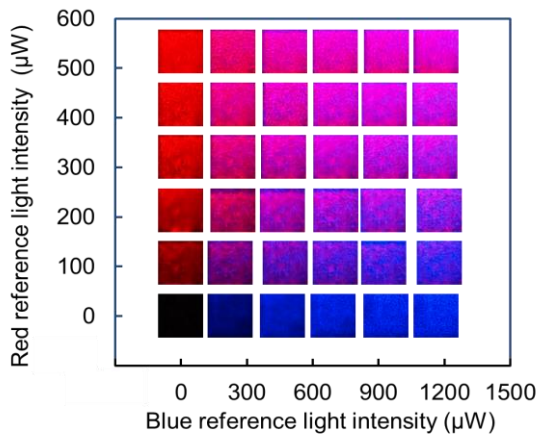
green, and red were plotted on each peak point of triangle, intermediate colors of two colors were on line of triangle, and intermediate colors of three colors were in a triangle, as shown in Fig.5.3.4-4. The gamut of theoretical values were calculated by each illumination light wavelength. Measurement points were in sRGB triangle because the CCD for getting reconstructed images was based on sRGB.



(a)



(b)



(c)

Fig. 5.2.4-3 Intermediate colors by modulation of illumination light intensity.

For demonstration of the colorized magnetic holograms, a 3D image with blue, green, and red colors was reconstructed as shown in Fig.5.2.4-5. The diameter of each sphere was 3.0 mm. The distance between each sphere and the BiDyYFeAlG film was 20 mm. Image resolution of hologram pattern was 8180×5696 pixels in $11.1 \times 7.7 \text{ mm}^2$ for 450 nm, 8080×8277 pixels in $11.0 \times 11.3 \text{ mm}^2$ for 532 nm, and 9560×6099 pixels in $13.0 \times 8.3 \text{ mm}^2$ for 633 nm. These differences in image resolution were caused because the diameters of Fresnel zone plate depended on the wavelength of light. Illumination light intensities were $441 \mu\text{W}$ at blue, $32 \mu\text{W}$ at green, and $216 \mu\text{W}$ at red.

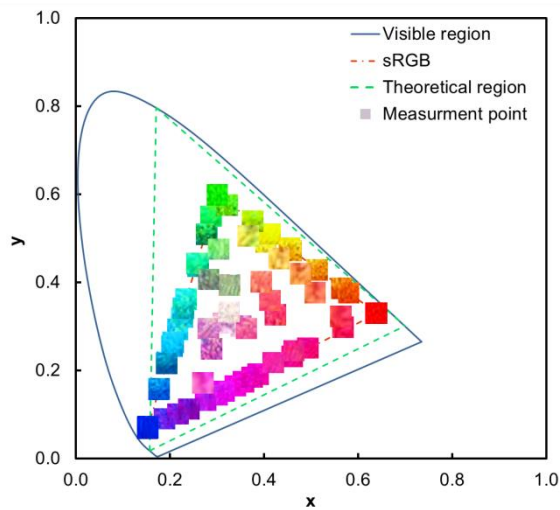


Fig. 5.2.4-4 Color gamut mapping of synthesized images.

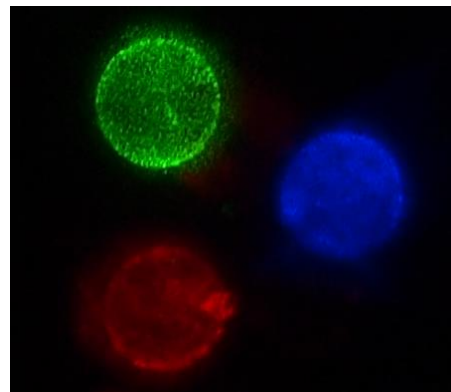


Fig. 5.2.4-5 3D spheres with RGB color.

5.3 Representation of gray level hologram

5.3.1 Faraday rotation angle modulation

As discussed in chapter 2, the diffraction efficiency of a transmission-type magnetic hologram depends on the Faraday rotation angle of each pixel and transmittance of the magnetic film. The reason that the magnetic hologram is a binary hologram, is that the rotation angle of each pixel has only two values corresponding to an incident recording light, or not. Generally, the Faraday rotation angle depends on the following equation

$$\theta_F = F \frac{M}{M_s} l. \quad (5.3.1-1)$$

Where F is the Faraday rotation coefficient that depends on the magnetic material, M is magnetization in light path direction, M_s is saturated magnetization, and l is light path length in magnetic media. Faraday rotation F , saturated magnetization M_s , and light path length l are fixed in fabrication condition of magnetic media. This paper focused on controlling magnetization M by controlling recording light energy density. For controlling magnetization M , the pixel depth that was the deepest position in an area with more than Curie temperature in thermal magnetic recording, was controlled.

The relationship of the magnetic pixel depth and recording light energy density was calculated with finite element simulation (COMSOL multi physics 4.3.a). Figure 5.3.1-1 shows the simulation model. The magnetic material was BiDyYFeAlG with perpendicular magnetization. Thickness of BiDyYFeAlG was 1.2 μm . Recording pixel pattern was magnetic lattice pattern, width of recording light was 1.36 μm , pitch of the light was 1.36 μm . The resolution of the magnetic pixel is same as the tiling optical system [15]. Depth of recorded magnetic pixel was defined as the region heated over the Curie temperature. Materials properties used for the simulation were shown in table 5.3.1-1.

Figure 5.3.1-2 shows a calculated relationship between recording light energy density and pixel depth. The pixel depth changed continuously when the recording light energy density increased. When recording, the light-energy density was from 35 mJ/cm^2 to 120 mJ/cm^2 , the pixel depth was from 0 μm to 1.18 μm . As a result, the magneto-optic holographic three-dimensional display could represent multi-level pixels by controlling recording light energy density.

Table 5.3.1-1 Thermal and optical properties for recording depth simulation

Material	Heat conductivity [W/m-K]	Specific heat capacity [J/kg-K]	Refractive Index n	Extinction Coefficient κ
Air	0.033	1007	1.00	0
BiDyYFeAlG	7.00	570	2.09	0.034
SGGG	7.05	381	2.07	0

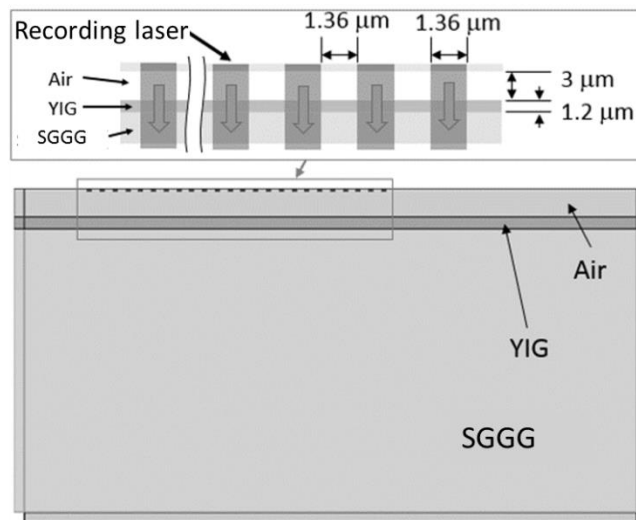


Fig. 5.3.1-1 Simulation model of thermomagnetic recording.

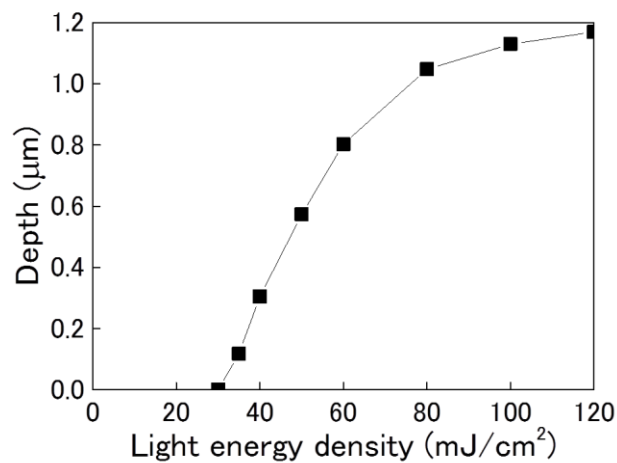


Fig. 5.3.1-2 Calculated pixel depth versus recording light energy density of thermomagnetic recording.

5.3.2 Evaluation of Faraday rotation angle

For evaluation of multi-level pixels in experiments, the BiDyYFeAlG film was fabricated by ion beam sputtering on substituted gadolinium gallium garnet substrate (SGGG sub.). The sputtering target was $\text{Bi}_{1.5}\text{Dy}_{1.0}\text{Y}_{1.0}\text{Fe}_{3.8}\text{Al}_{1.2}\text{O}_x$. The BiDyYFeAlG film had good perpendicular magnetization, a large Faraday rotation, and high transmissivity in the visible wavelength. The BiDyYFeAlG film was annealed at 750 °C in atmosphere. The thickness of the BiDyYFeAlG film was 2.8 μm . The BiDyYFeAlG was thicker than the calculation model as a proof of principle. Faraday rotation angle and transmittance were approximately 8° and 20 %, respectively, at 532 nm wavelength.

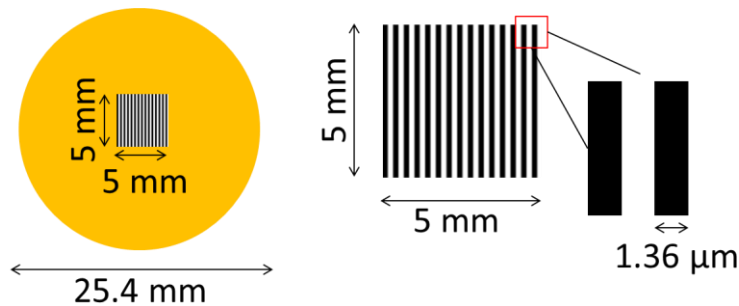


Fig. 5.3.2-1 A simple magnetic grating with every recording light energy density. The grating was recorded via a tiling optical system.

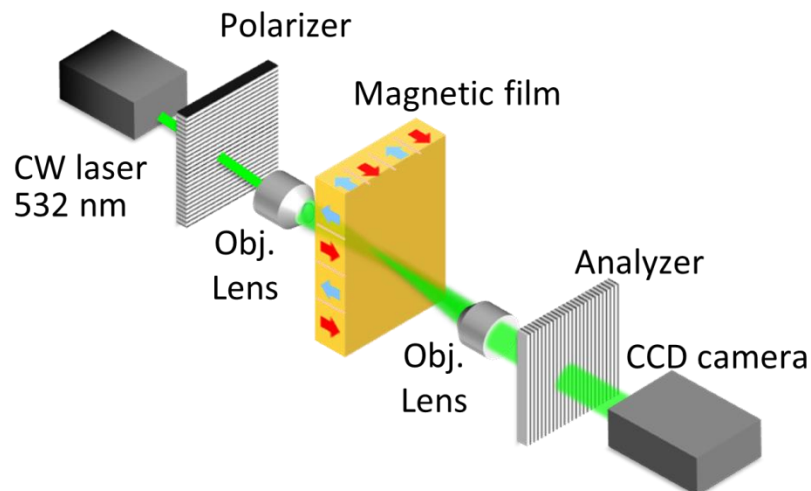


Fig. 5.3.2-2 Schematic image of optical system to measure the Faraday rotation angle distributions by rotating polarizer method.

To evaluate diffraction efficiency, the BiDyYFeAlG film recorded a magnetic grating pattern with changing recording light energy density as shown in Fig.5.3.2-1. A magnetic pixel array acted as magnetic grating pattern with an area of $5 \times 5 \text{ mm}^2$, a line of grating was $1.36 \mu\text{m} \times 5 \text{ mm}$, and the stripe pitch was $1.36 \mu\text{m}$. The recording light was pulsed laser with 532 nm wavelength, 10 ns pulse width, and light energy density from 60 to 120 mJ/cm^2 . To measure the Faraday rotation angle distribution on the BiDyYFeAlG film, a measurement system combining rotating analyzer method and polarization microscope was used as shown in Fig. 5.3.2-2.

Figure 5.3.2-3 shows the measurement results of Faraday rotation angle distribution on the BiDyYFeAlG film with magnetic grating. The yellow region was not illuminated by recording light, and the Faraday rotation angle of the red region was changed with increasing recording energy density. Figure 5.3.2-4 shows the averaged Faraday rotation angle of peak value in each line corresponding to the recorded and non-recorded areas. Faraday rotation angle of the recorded area was represented as θ_{down} , and Faraday rotation angle of non-illuminated area was represented as θ_{up} . θ_{down} was changed continuously and θ_{up} was maintained when the recording light energy increased. The minimum θ_{down} was 0° , because the areas, which were hotter than the Curie temperature, were thermally demagnetized. For each magnetic grating on the BiDyYFeAlG film, diffraction efficiency was measured. These results are shown in Fig. 5.3.2-5. When the recording light energy density was between 60 mJ/cm^2 and 120 mJ/cm^2 , the diffraction efficiency changed continuously from $0.4 \times 10^{-2} \%$ to $3 \times 10^{-2} \%$. In addition, theoretical diffraction efficiency, which was calculated by using the follow equations, was also plotted in Fig. 5.3.2-5.

$$\eta = \frac{4}{\pi^2} T \sin^2 \Delta\theta_F \quad (5.3.2-1)$$

$$\Delta\theta_F = \frac{\theta_{\text{up}} - \theta_{\text{down}}}{2} \quad (5.3.2-2)$$

Where η is diffraction efficiency, T is transmittance of the magnetic film, and $\Delta\theta_F$ is effective Faraday rotation angle of magnetic gratings. Both results showed good agreement with each other, meaning that the diffraction efficiency of magnetic hologram could be controlled by changing the Faraday rotation angle of the magnetic pixels.

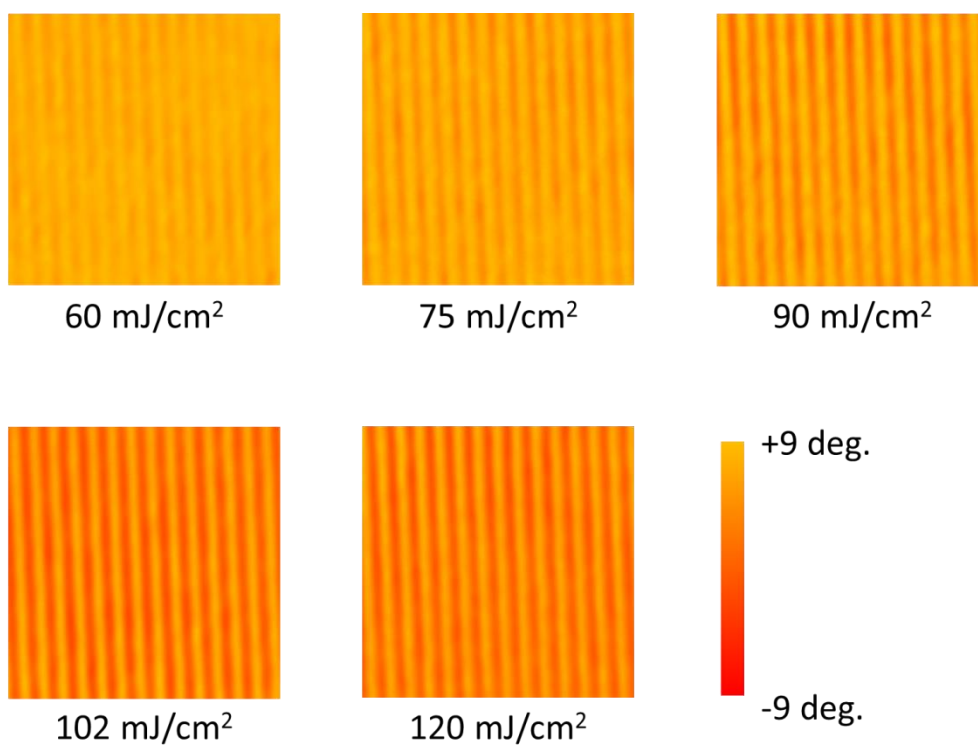


Fig. 5.3.2-3 Distribution of Faraday rotation angle of magnetic grating on the BiDyYFeAlG film. The yellow area did not get incident recording light.

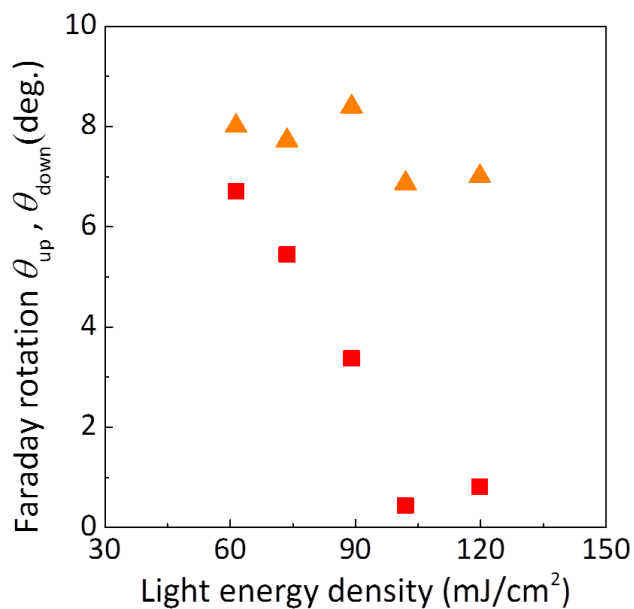


Fig. 5.3.2-4 Faraday rotation angle versus recording light energy density. θ_{up} was initial Faraday rotation on the area that was not illuminated with recording light. θ_{down} was controlled by Faraday rotation on the area that was illuminated with recording light.

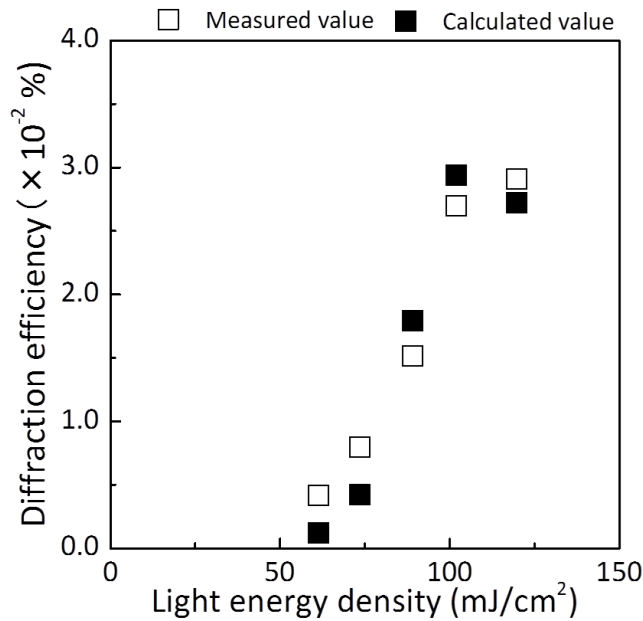


Fig.5.3.2-5 Relationship between diffraction efficiency and recording light energy density. White plots mean measured diffraction efficiency and black plots mean diffraction efficiency that was calculated with measurement results of Fig. 5.3.2-4.

5.3.3 Reconstruction of magnetic hologram with multilevel brightness

Finally, a multi-level brightness 3D image using multi-level pixels was demonstrated. The hologram was generated by computer generated half zone plate method [14], [16]. Figure 5.3.3-1 shows the 3D model of the generated hologram and the optical set up for reconstruction. The 3D model was the image of a wire-framed cube. The size of a pixel was $1.36 \times 1.36 \mu\text{m}^2$. The total number of magnetic pixels was 10000×10000 . A generated hologram was converted into a binary hologram as θ_{up} or θ_{down} . The hologram was recorded on BiDyYFeAlG film by the tiling optical system. For reconstructing 3D image with each-level brightness, the light energy density for recording magnetic pixels was changed to 60 mJ/cm^2 , 90 mJ/cm^2 , and 120 mJ/cm^2 . Illumination light source was continuous wave laser with 532 nm wavelength, and illuminated light was incident on all holograms with 8.6 mW/cm^2 . Figure 5.3.3-2 shows the reconstructed 3D images. The viewing angle of reconstruction image was 23° . The magneto-optic holographic three-dimensional display could represent three-level brightness 3D images using a BiDyYFeAlG film.

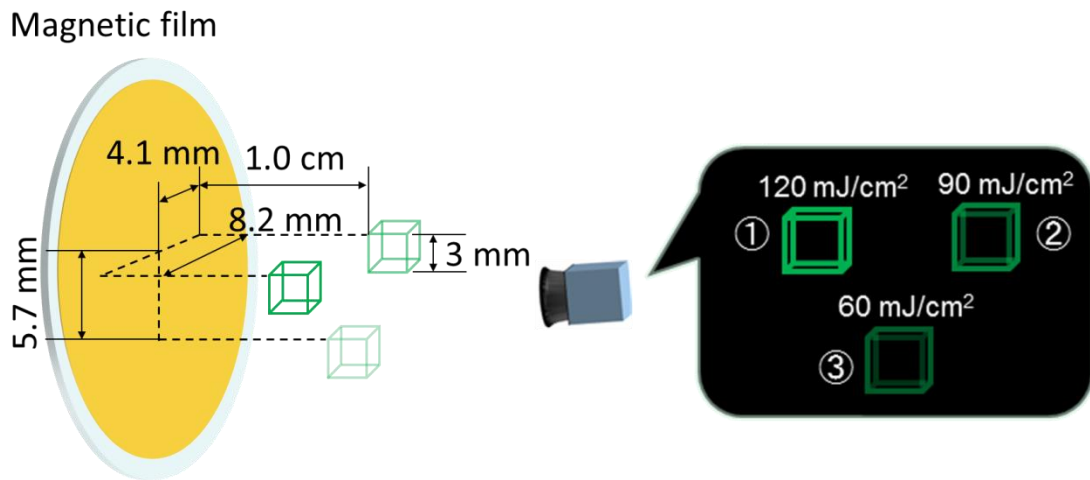


Fig. 5.3.3-1 Models of 3D images with multi-level pixels.

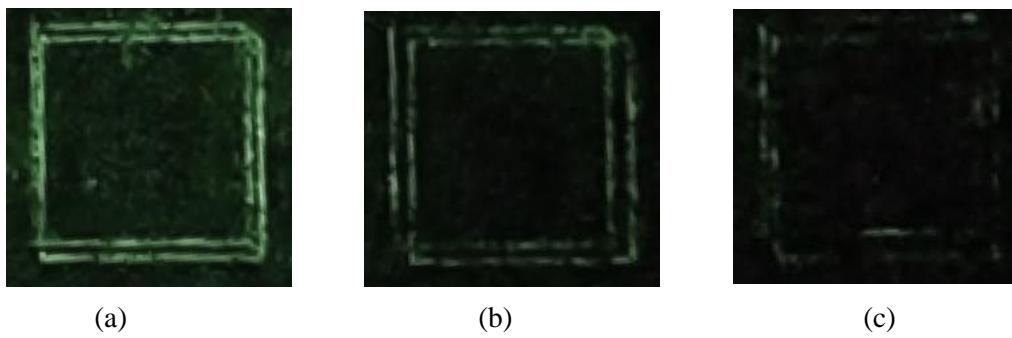


Fig. 5.3.3-2 Reconstructed 3D images with different levels of brightness, which were recorded on a BiDyYFeAlG film. (a) was 120 mJ/cm², (b) was 90 mJ/cm², and (c) was 60 mJ/cm²

5.4 Summary

Chapter 5 discussed methods for improving image quality. In previous chapters, the magneto-optic holographic three-dimensional display was developed to represent holographic video with monochrome and monotone. However, to put it into practical use, colorization and multilevel gradations of reconstruction images were discussed.

As proof of principle for colorization, the optical space division method was adopted. The magnetic material of the media (BiDyAl:YIG) has wavelength dependence on transmittance and Faraday rotation angle. Therefore, the film thicknesses for reconstructing each color image were designed to obtain high diffraction efficiency. Each primary color hologram was recorded on thickness-designed films. By synthesizing each single-color image with different levels of brightness, it was confirmed that the display color is gradationally controlled by the ratio of the illumination light intensities, and the synthesized reconstructed image covered the standard RGB color region, including white. A white color image could also be represented by illumination light intensity modulations; ratio of light intensity of each reconstructed image was blue: green: red = 0.66: 0.92: 1.00, where reconstructed light intensities were adjusted by varying the illumination light intensities.

The Faraday rotation angle depends on recording depth, which was controlled by recording laser power to demonstrate representation of gray level holograms. Faraday rotation angle of recorded area was represented as θ_{down} , and Faraday rotation angle of non-illuminated area was represented as θ_{up} . θ_{down} was changed continuously and θ_{up} was maintained when the recording light energy increased. The minimum θ_{down} was 0° because the areas, which were hotter than Curie temperature, were thermally demagnetized. For each magnetic grating on the BiDyYFeAlG film, diffraction efficiency was measured. When the recording light energy density was between 60 mJ/cm^2 and 120 mJ/cm^2 , the diffraction efficiency was changed continuously from $0.4 \times 10^{-2} \%$ to $3 \times 10^{-2} \%$. In addition, the theoretical diffraction efficiency was calculated by using measured Faraday rotation angles. Both results showed good agreement, implying that the diffraction efficiency of magnetic hologram can be controlled by changing the Faraday rotation angle of the magnetic pixels. The result suggested that the recording power can control the diffraction efficiency, and the brightness of reconstructed images.

Finally, the multi-level brightness 3D image was demonstrated using multi-level pixel. For reconstructing a 3D image with each-level brightness, the light energy density for recording magnetic pixels was changed to 60 mJ/cm^2 , 90 mJ/cm^2 , and 120 mJ/cm^2 . The magneto-optic holographic three-dimensional display could represent three-level brightness 3D images from a BiDyYFeAlG film.

References

- [1] K. Nakamura, H. Takagi, T. Goto, P. B. Lim, H. Horimai, H. Yoshikawa, V. M. Bove, and M. Inoue, "Improvement of diffraction efficiency of three-dimensional magneto-optic spatial light modulator with magnetophotonic crystal," *Appl. Phys. Lett.*, vol. 108, no. 2, 2016.
- [2] W. Wettling, B. Andlauer, P. Koidl, J. Schneider, and W. Tolksdorf, "Optical absorption and Faraday rotation in yttrium iron garnet," *Phys. Status Solidi*, vol. 59, no. 1, pp. 63–70, 1973.
- [3] Y. Asahara, S. Sasaki, K. Haraga, K. Yamaguchi, and T. Fujii, "Theoretical Consideration of Faraday Rotation Spectra of Bismuth Substituted Yttrium Iron Garnet Films," *IEEE Trans. Magn.*, vol. 28, no. 5, pp. 2985–2987, 1992.
- [4] T. Shimobaba, T. Takahashi, N. Masuda, and T. Ito, "Numerical study of color holographic projection using space-division method," *Opt. Express*, vol. 19, no. 11, p. 10287, May 2011.
- [5] K. Sato, "Special Issue Image Technology of Next Generation. Animated Color 3D Image Display using Kinoforms by Liquid Crystal Devices.," *J. Inst. Telev. Eng. Japan*, vol. 48, no. 10, pp. 1261–1266, 1994.
- [6] T. Yamaguchi, "Real-time image plane full-color and full-parallax holographic video display system," *Opt. Eng.*, vol. 46, no. 12, p. 125801, Dec. 2007.
- [7] N. Pandey and B. Hennelly, "Quantization noise and its reduction in lensless Fourier digital holography.," *Appl. Opt.*, vol. 50, no. 7, pp. B58–B70, 2011.
- [8] G. a Mills and I. Yamaguchi, "Effects of quantization in phase-shifting digital holography.," *Appl. Opt.*, vol. 44, no. 7, pp. 1216–1225, 2005.
- [9] O. Matoba, T. J. Naughton, Y. Frauel, N. Bertaux, and B. Javidi, "Real-time three-dimensional object reconstruction by use of a phase-encoded digital hologram.," *Appl. Opt.*, vol. 41, no. 29, pp. 6187–6192, 2002.
- [10] 鈴木守, "カンデラの定義の改定その他について," *J. Spectrosc. Soc. Japan*, vol. 29, no. 2, pp. 127–128, 1980. (in Japanese)
- [11] M. Inoue, T. Fujii, and I. Introduction, "A theoretical analysis of magneto-optical Faraday effect of YIG films with random multilayer structures," *J Appl Phys*, vol. 81, no. 8, pp. 5659–5661, 1997.
- [12] M. Inoue, R. Fujikawa, A. Baryshev, A. Khanikaev, P. Lim, H. Uchida, O. Aktsipetrov, A. Fedyanin, T. Murzina, and A. Granovsky, "Magnetophotonic crystals," in *INTERMAG 2006 - IEEE International Magnetism Conference*, 2006, vol. 39, pp. 19–19.
- [13] R. Isogai, N. Sagara, T. Goto, Y. Nakamura, P. B. Lim, and M. Inoue, "Diffraction Efficiency of Volumetric Magnetic Holograms with Magnetophotonic Crystals," *J.*

- Magn. Soc. Japan*, vol. 38, no. 3–2, pp. 119–122, 2014.
- [14] T. Mishina, F. Okano, and I. Yuyama, “Time-alternating method based on single-sideband holography with half-zone-plate processing for the enlargement of viewing zones,” *Appl. Opt.*, vol. 38, no. 17, pp. 3703–3713, 1999.
- [15] H. Takagi, K. Nakamura, S. Tsuda, T. Goto, P. Boey Lim, and M. Inoue, “Magneto-optic Three-Dimensional Holographic Display with Tiling Optical Addressing Method,” *Sensors Mater.*, vol. 27, no. 10, pp. 1003–1008, 2015.
- [16] T. Kurihara and Y. Takaki, “Improving viewing region of 4f optical system for holographic displays,” *Opt. Express*, vol. 19, no. 18, p. 17621, 2011.

6. Conclusion

This thesis discussed the development of a magneto-optic holographic three-dimensional display using an artificial magnetic lattice. Holographic display is a three-dimensional (3D) display technique that can represent high-presence 3D images. For practical use, a high-speed display that can represent holograms with order-of-light wavelength is required. The magneto-optic holographic three-dimensional display is expected to solve this problem by using magnetic media, which has excellent recording speed and density. Using artificial magnetic lattice structures, a media with high brightness can be recorded using low energy; in addition, a reduction in magnetic hologram noise was realized. Calculation methods of computer generated holograms for a complex 3D object with many point-light sources, optical systems to represent holographic video with tiny magnetic pixels, and quality improvement of reconstructed images, were discussed.

In chapter 1, the previous work of this project group in the development of magneto-optic holographic three-dimensional displays was discussed, in addition to providing some background. In addition, the merits of holography were also discussed.

Chapter 2 discussed the improvement of light efficiency of magnetic media. To apply magnetic hologram for holographic display, light efficiencies of recording and reconstruction of holograms were regarded as a problem, and these efficiencies were dominated by the material of the media. In this thesis, light efficiencies were improved by using a magnetophotonic crystal (MPC) for recording and reconstruction. The diffraction efficiency of MPC was $2.1 \times 10^{-2} \%$, and required illumination light to represent 100 cd/m^2 brightness reduced from 24 mW/cm^2 to 10.8 mW/cm^2 compared to a case of amorphous terbium iron (*a*-TbFe) film. In addition, the MPC could reduce the light energy density for thermomagnetic recording by 59 % relative to a mono layer bismuth dysprosium aluminum substituted yttrium iron garnet (BiDyYFeAlG) film with similar diffraction efficiency. In addition, a multilayer structure, which comprised two different magnetic materials as magnetic hologram media showing high diffraction efficiency and low writing energy, was proposed. The *a*-TbFe/BiDyYFeAlG multilayer media showed high diffraction efficiency corresponding to BiDyYFeAlG and low recording energy density corresponding to a *a*-TbFe layer.

Chapter 3 discussed the calculation methods of computer generated holograms for magnetic hologram. To calculate a complex object and its surface, the two-dimensional image based method was adopted. This method was suitable for generating a complicated hologram composed of many point-light sources, and for additional calculations of hologram such as occlusions. Holograms on magneto-optic holographic three-dimensional display were binary holograms, which were represented by perpendicular magnetization directions. Usual

reconstructed images with binary holograms included binarization errors. Therefore, this paper focused on the pixel position of magnetic hologram that was not mechanically fixed. To reduce binarization errors, pixel positions of computer generated hologram were considered via the simulated annealing (SA) method. The SA method could treat pixel positions of magnetic hologram as a calculation parameter, so that the error value included in simulated reconstruction images was reduced.

Chapter 4 discussed the optical system for a holographic video system, and demonstrated a holographic video on magnetic medium with narrow viewing angle. The holographic video system consisted of three elements—a hologram recording system, a hologram reconstruction system, and an erasure system for the magnetic hologram. To demonstrate holographic video, synchronization of recording and erasure systems were constructed, and timing of recording was determined by pulsed laser. Recording laser pulse (wavelength 532 nm, pulse width 10 ns, repetition frequency 10 Hz) was synchronized to the representation of digital micro mirror device (DMD) by the trigger signal. After recording, an external magnetic field (400 Oe) was applied to erase the magnetic hologram. By using the optical system, a holographic video—a rotating wireframe cube—was displayed with the optical system: framerate was 10 fps, 13.6 $\mu\text{m}/\text{pixel}$, 367×367 pixels. In addition, the new hologram recording system used a micro lens array matching to DMD pixels to reduce scanning length.

Chapter 5 discussed a method to improve image quality. In previous chapters, a magneto-optic holographic three-dimensional display was developed to represent holographic video with monochrome and monotone. However, to put it into practical use, colorization and multilevel gradations of reconstruction images are important. Two methods were proposed to control color or brightness of reconstructed images. As proof of principle for colorization, the optical space division method was adopted. The magnetic material of the media (BiDyAl:YIG) has wavelength dependence of transmittance and Faraday rotation angle. Therefore, the thicknesses of films required to reconstruct each color image were designed to obtain high diffraction efficiency. The synthesized reconstructed image covered standard RGB color region, including white. To demonstrate representation of gray level hologram, the Faraday rotation angle depends on recording depth, which could be controlled by recording laser power. The result suggested that the recording power can control the diffraction efficiency and brightness of reconstructed images.

This thesis established all basic elemental technologies of magneto-optic holographic three-dimensional displays. By effectively combining these elemental technologies, magneto-optic holographic displays can show more realistic and natural 3D images.

Acknowledgments

This thesis was written in the Department of Electronic and Information Engineering, Toyohashi University of Technology. I would like to greatly appreciate the instruction and advice with Assoc. Prof. Hiroyuki Takagi, VP, and Prof. Mitsuteru Inoue.

I appreciate the help in writing this thesis, performing experiments and calculations, and the fruitful advice received from Prof. Hironaga Uchida, Assoc. Prof. Yuichi Nakamura, Assoc. Prof. Lim Pang-Boey, and Dr. Taichi Goto. I thank the supervisors of the Leading Program Prof. Hiroshi Yoshikawa, Prof. Horimai Hideyoshi, and Prof. V. Michael Bove Jr. I am grateful to Prof. Mitsuo Fukuda, and Prof. Shinichi Suzuki for their precise reviews.

In the Leading Program, I would like to appreciate the precious and beneficial advice from Prof. Shigeki Nakauchi, Prof. Seiichi Nakagawa, Prof. Akihiro Wakahara, Prof. Atsunori Matsuda, and Special Prof. Hiromu Ishii.

In chapter 3, I learned the computer-generated hologram in the MIT Media Lab, United States. I would like to appreciate the help received from Mr. Sunny Jolly, Dr. Nickolaos Savidis, Ms. Bianca Datta, Mr. Andrew MacInnes, and Ms. Kristin Hall in the Object Based Media group of MIT Media Lab, in learning that technique.

I thank Dr. Shinichiro Mito, Dr. Ryouzuke Isogai, Dr. Ryouzuke Hashimoto, Mr. Naoki Kanazawa, Mr. Ryohei Morimoto, and Mr. Takuya Yoshimoto for their beneficial advice. A lot of seniors and peers helped advance this research. I would like to thank Mr. Takeru Yonezawa, Mr. Yu Eto, Mr. Kazuki Matsugami, Mr. Kei Kudo, Mr. Sotaro Tsuda, Ms. Aki Nemoto, Mr. Kazuki Yamazaki, Mr. Shoki Sakai, Mr. Makoto Uchino, Mr. Hideyuki Kurahashi, Mr. Masashi Matsumoto, Mr. Yuma Kawaguchi, and Mr. Yota Kimura. I would like to thank Ms. Yumiko Yamamoto for help as a secretary. I would like to thank Dr. Hajime Tsukada, Ms. Yuki Izawa, and Ms. Yuri Tanaka for help activities in the Leading Program.

In addition, I feel grateful to Mr. Naoto Sagara, Mr. Michinari Hoso, Mr. Kazuya Yokomi, Mr. Yuji Hayashi, Mr. Akio Shimada, and Mr. Taiki Yasuda for their considerable support in life outside of the laboratory. I would like to appreciate my family: Mr. Kazushige Nakamura, Ms. Hideko Nakamura, Mr. Shoichi Nakamura, Ms. Ayako Nakamura, Ms. Haruka Nakamura, and Ms. Kie Nakamura for their kindly support.

Research achievements

Papers

1. Hiroyuki Takagi, Kazuki Nakamura, Taichi Goto, Pang Boey Lim, and Mitsuteru Inoue, “Magneto-optic spatial light modulator with submicron-size magnetic pixels for wide-viewing-angle holographic displays”, *Opt. lett.*, **39**, 3344-7 (4 pages), 2014
2. Kazuki Nakamura, Kei Kudo, Taichi Goto, Hiroyuki Takagi, Pang Boey Lim, and Mitsuteru Inoue, “Colorization of Magnetic Hologram Images With Optical Space Division Method,” *IEEE Trans. Magn.*, **50**, no. 11, 4007304 (4 pages), 2014.
3. Hiroyuki Takagi, Kazuki Nakamura, Kei Kudo, Taichi Goto, Pang Boey Lim, and Mitsuteru Inoue, “Colorized Magneto-optic Three Dimensional Display Using Optical Space Division Method” *J. Magn. Soc. Japan* **39**, 44 (2015)
4. Ryosuke Isogai, Shota Suzuki, Kazuki Nakamura, Yuichi Nakamura, Hiroyuki Takagi, Taichi Goto, Pang Boey Lim, and Mitsuteru Inoue, “Collinear Volumetric Magnetic Holography with Magnetophotonic Microcavities,” *Opt Express*, **23**, 13153-13158, 2015
5. Hiroyuki Takagi, Kazuki Nakamura, Sotaro Tsuda, Taichi Goto, Pang Boey Lim and Mitsuteru Inoue, “Magneto-optic Three-Dimensional Holographic Display with Tilling Optical Addressing Method,” *Sensors Mater.*, **27**, 1003-1008, 2015
6. Kazuki Nakamura, Hiroyuki Takagi, Taichi Goto, Pang Boey Lim, Hideyoshi Horimai, Hiroshi Yoshikawa, Victor Michael Bove Jr., and Mitsuteru Inoue, “Improvement of diffraction efficiency of three dimensional magneto-optic spatial light modulator with magnetophotonic crystal,” *Appl. Phys. Lett.*, **108**, 022404 (4 pages), 2016.

International conferences

1. Hiroyuki Takagi, Takeru Yonezawa, Yu Eto, Kazuki Nakamura, Alexander Baryshev, and Mitsuteru Inoue, “Hight-density spatial light modulators for 3D holographic displays”, International Workshop on Holography and Related Technologies 2011, E4, pp.107-108, Utsunomiya, Japan, 17th November 2011.
2. Hiroyuki Takagi, Takeru Yonezawa, Yu Eto, Kazuki Nakamura, and Mitsuteru Inoue, “Thermomagnetic-driven type magneto-optic spatial light modulator with submicron-size pixels”, The Asia-Pacific Interdisciplinary Research Conference 2011, 18PP-67, p.169, Toyohashi, Japan, 18th November 2011.
3. Takeru Yonezawa, Hiroyuki Takagi, Yu Eto, Kazuki Nakamura and Mitsuteru Inoue, “Magneto-optic Spatial Light Modulator with Submicron-size Magnetic Pixels for 3D Holographic Displays”, INTERMAG 2012, EW-14, Vancouver, Canada, 10th May 2012.
4. Yu Eto, Kazuki Nakamura, Kazuki Matsugami, Hiroyuki Takagi, and Mitsuteru Inoue,

- “Three-dimensional holographic display using amorphous TbFe film”, The Joint International Symposium on Optical Memory and Optical Data Storage, TUH-19, pp.112-113, Tokyo, Japan, 2nd October 2012.
5. Hiroyuki Takagi, Yu Eto, Kazuki Nakamura, Pang Boey Lim, and Mitsuteru Inoue, “Light-Addressed Magneto-Optic Spatial Light Modulator for Three-Dimensional Electronic Holographic Displays”, The Joint International Symposium on Optical Memory and Optical Data Storage, Tu-G-03, pp.60-61, Tokyo, Japan, 2nd October 2012.
 6. Mitsuteru Inoue, Yu Eto, Kazuki Nakamura, Kazuki Matsugami, and Hiroyuki Takagi, “Magneto-optic three-dimensional display composed of amorphous films with perpendicular magnetization for real holographic electronic display”, ICAUMS 2012, 4aB-2, p.250, Nara, Japan, 4th October 2012.
 7. Yu Eto, Kazuki Nakamura, Hiroyuki Takagi, Pang Boey Lim and Mitsuteru Inoue, “Three-dimensional display with magnetic hologram composed of a large number of nano-scale magnetic pixels in magnetic thin film with perpendicular magnetization.”, 12th Joint MMM/Intermag, HY-05, p.922, Chicago, USA, 18th January 2013.
 8. Hiroyuki Takagi, Kazuki Nakamura, Pang Boey Lim and Mitsuteru Inoue, “Magnetophotonic microcavity for holographic three-dimensional display”, Collaborative Conference on Materials Research Joint Wihte CC3DR 2013, pp.2-3, Jeju, Korea, 24th June 2013.
 9. Kazuki Nakamura, Kazuki Matsugami, Hiroyuki Takagi, Pang Boey Lim and Mitsuteru Inoue, “Magneto-optical three-dimensional display with magnetic garnet thin films”, IEEE the 2013 Summer Topicals meeting, MP10, Waikoloa, USA, 8th June 2013.
 10. Hiroyuki Takagi, Kazuki Nakamura, Kazuki Matsugami, Pang Boey Lim, and Mitsuteru Inoue, “Magneto-optic three-dimensional display composed of magnetic garnet films”, 58th Annual Conference on MMM, FC-06, pp.528, Denver, USA, 7th November 2013.
 11. Kazuki Matsugami, Kazuki Nakamura, Hiroyuki Takagi, and Mitsuteru Inoue, “Study on Magneto-optic Three-dimensional Display with Light-emitting Diode Array”, ISTS2013, ID226, pp. 257-258, Hong Kong, China, 20th November 2013.
 12. Kazuki Nakamura, Kazuki Matsugami, Taichi Goto, Hiroyuki Takagi, Pang Boey Lim, and Mitsuteru Inoue, “High brightness magneto-optical three dimensional displays using magnetophotonic crystal,” Magnetism and Optics Research International Symposium 2013, Th-02-03 (2 pages), Saitama, Japan, 2nd December 2013.
 13. Ryosuke Isogai, Shota Suzuki, Kazuki Nakamura, Naoto Sagara, Taichi Goto, Hiroyuki Takagi, Yuichi Nakamura, Pang Boey Lim, and Mitsuteru Inoue, “Magneto-optic Volumetric Collinear Holography with Magnetophotonic Crystals”, IEEE International Magnetism Conference, BG-02 (2 pages), Dresden, Germany, 4th May 2014.

14. Kazuki Nakamura, Kei Kudo, Taichi Goto, Hiroyuki Takagi, Pang Boey Lim, and Mitsuteru Inoue, "Colorization of Magneto-optic Three Dimensional Display with Magnetic Garnet Films," IEEE International Magnetics Conference, HV-02 (2 pages), Dresden, Germany, 4th May 2014.
15. Hiroyuki Takagi, Kazuki Nakamura, Kei Kudo, Taichi Goto, Pang Boey Lim, and Mitsuteru Inoue, "Magneto-optic Three-dimensional Display Using Magnetophotonic Crystal", ICO23, p24, Santiago, Spain, 26th August 2014.
16. Kazuki Nakamura, Hiroyuki Takagi, Taichi Goto, Pang Boey Lim, and Mitsuteru Inoue, "Magneto-optic Three Dimensional Display for Gray-level Holograms," The 3rd International Conference of Asian Union of Magnetics Societies, A7-05 (1 page), Haikou, China, 28th October 2014.
17. Hiroyuki Takagi, Kazuki Nakamura, Taichi Goto, Pang Boey Lim, Mitsuteru Inoue, "Magneto - optic Three - dimensional Display Using Magnetic Lattice Structure", The 3rd International Conference of Asian Union of Magnetics Societies, A4-27 (1 page), Haikou, China, 28th October 2014.
18. Kazuki Nakamura, Hiroyuki Takagi, Taichi Goto, Pang Boey Lim, and Mitsuteru Inoue, "Modulation of Faraday rotation angle for gray-level MO-3DD," 59th Annual Magnetism & Magnetic Materials Conference, BV-06 (1 page), Honolulu, USA, 3rd November 2014.
19. Kazuki Nakamura, Hiroyuki Takagi, Taichi Goto, Pang Boey Lim, and Mitsuteru Inoue, "Magnetophotonic crystal for magneto-optic three dimensional display with optical addressing method," 2014 MRS Fall Meeting & Exhibit, L11.07 (1 page), Boston, USA, 30th November 2014.
20. Hiroyuki Takagi, Kazuki Nakamura, Kei Kudo, Taichi Goto, Pang Boey Lim, Mitsuteru Inoue, "Colorization of Magneto-Optic Three-Dimensional Display Composed of Magnetic Garnet Films", 2014 MRS Fall Meeting & Exhibit, L14.16 (1 page), Boston, USA, 4th December 2014.
21. Hiroyuki Takagi, Kazuki Nakamura, Taichi Goto, Pang Boey Lim, and Mitsuteru Inoue, "Magneto-optic Three Dimensional Holographic Display with Tiling Optical Addressing Method", IGNITE2014, 2014-03-36-0042, pp. 256-259, Penang, Malaysia, 15th December 2014.
22. Hiroyuki Takagi, Kazuki Nakamura, Taichi Goto, Pang Boey Lim, and Mitsuteru Inoue, "Magneto-optic Holographic Display Using Magnetophotonic Crystals", BIT's 1st Annual World Congress of Smart Materials-2015, Session 704: Smart Materials for ICT, Display and Imaging Technology, Usan, Korea, 25th March 2015.
23. Kazuki Nakamura, Hiroyuki Takagi, Taichi Goto, Pang Boey Lim, and Mitsuteru Inoue, "Study on magneto-optic three dimensional display composed of magnetophotonic crystal,"

META 2015, P6 (2 pages), New York, USA, 4th August 2015.

24. Hiroyuki Takagi, Kei Kudo, Kazuki Nakamura, Taichi Goto, Pang Boey Lim, Mitsuteru Inoue, “THREE DIMENSIONAL DISPLAY COMPOSED OF MULTI-CAVITY MAGNETOPHOTONIC CRYSTAL FOR COLOR IMAGES”, MORIS2015, Mo-P-07, pp.31-32, Penang, Malaysia, 30th November 2015.
25. Kei Kudo, Kazuki Nakamura, Shoki Sakai, Taichi Goto, Hiroyuki Takagi, Pang Boey Lim, and Mitsuteru Inoue, “Colorization three dimensional holographic display composed of multi-cavity magneto-photonic crystal”, MMM/INTERMAG 2016 Joint Conference, San Diego, USA, 13th January 2016.
26. Hiroyuki Takagi, Kazuki Nakamura, Taichi Goto, Pang Boey Lim, and Mitsuteru Inoue, “Three-dimensional Magneto-optic Spatial Light Modulator Composed of Artificial Magnetic Lattice”, Collaborative Conference on 3D and Materials Research (CC3DMR)2016, Seoul, Korea, 22nd June 2016.
27. Kazuki Nakamura, Taichi Goto, Hiroyuki Takagi, Yuichi Nakamura, Pang Boey Lim, Hironaga Uchida, and Mitsuteru Inoue, “Three dimensional magneto optic spatial light modulator with high efficiency magnetic hologram media”, 2016 MRS Fall Meeting & Exhibit, EM2.8.07 (1 page), Boston, USA, 29th November 2016.
28. Kazuki Nakamura, Kazuki Yamazaki, Hiroyuki Takagi, Pang Boey Lim, Hironaga Uchida, and Mitsuteru Inoue “Multilevel light modulation of three-dimensional magneto-optic spatial light modulator using optically addressing method,” EI2017, SD&A-360 (1 pages), Burlingame, USA, 30th January 2017.

Domestic conferences

1. 米澤建, 江藤優, 中村和樹, 高木宏幸, 井上光輝, “アモルファス垂直磁化膜へのナノスケール磁気ピクセルの形成と空間光変調器への応用,” 電気学会 マグネティックス研究会, MAG-11-039, pp.35-38, 高知, 日本, 3rd August 2011.
2. 米澤建, 江藤優, 中村和樹, 高木宏幸, 井上光輝, “アモルファス Tb Fe 垂直磁化膜へのナノスケール磁気ピクセルの形成と 3次元画像表示のための光変調基礎特性,” 第35回日本磁気学会学術講演会, 29pE-10, p. 297, 新潟, 日本, 29th September 2011.
3. 米澤建, 江藤優, 中村和樹, 高木宏幸, 井上光輝, ” 電子ホログラフィ 3次元ディスプレイへの応用に向けたナノスケール磁気ピクセル空間光変調器に関する研究”, 電気学会マグネティックス研究会, MAG-11-108, pp.87-90, 仙台, 日本, 25th November 2011.
4. 高木宏幸, 江藤優, 中村和樹, 井上光輝, “光アドレス駆動型磁気光学空間光変調器を用いた広視野角電子ホログラフィックディスプレイ”, MAG-12-080, pp.43-46, 函

館, 日本, 8th August 2012.

5. 米澤建, 高木宏幸, 江藤優, 中村和樹, 井上光輝, “ナノ磁気ピクセル空間光変調器を用いた3次元電子ホログラフィディスプレイ”, 電気学会 基礎・材料・共通部門大会, VIII-11, pp.257-262, 秋田, 日本, 21st September 2012.
6. 江藤優, 中村和樹, 高木宏幸, 井上光輝, “タイリング光アドレス方式を用いた磁気光学3次元ホログラムディスプレイの基礎特性”, 平成24年度 電気関係学会 東海支部連合大会, H2-6, 豊橋, 日本, 24th September 2012.
7. 中村和樹, 江藤優, 高木宏幸, 井上光輝, “CMOSを用いたホログラム像の実写と磁気光学3次元ディスプレイへの応用”, 平成24年度 電気関係学会 東海支部連合大会, G5-6, 豊橋, 日本, 25th September 2012.
8. 中村和樹, 江藤優, 高木宏幸, 林攀梅, 高木康博, 井上光輝, “光アドレス方式を用いた磁気光学3次元ディスプレイの基礎特性”, 電子情報通信学会 電子部品・材料研究会(CPM), CPM2012-87(2012-09), pp.11-14, 東京, 日本, 2nd October 2012.
9. 中村和樹, 江藤優, 高木宏幸, 林攀梅, 井上光輝, “磁気光学3次元ディスプレイによる計算機ホログラム像の再生”, 電子情報通信学会 マルチメディアストレージ研究会, MR2012-46, pp.23-26, 名古屋, 日本, 6th March 2013.
10. 中村和樹, 松上一樹, 高木宏幸, 林攀梅, 井上光輝, “磁性ガーネット膜を用いた磁気光学3次元ディスプレイの光利用効率改善”, 電気学会 マグネティックス研究会, MAG-13-083, pp.77-81, 名古屋, 日本, 8th August 2013.
11. 中村和樹, 松上一樹, 高木宏幸, 林攀梅, 井上光輝, “磁性ガーネット膜を用いた磁気光学3次元ディスプレイ”, 第37回日本磁気学会学術講演会, 3aF-5, p.99, 札幌, 日本, 3rd September 2013.
12. 中村和樹, 高木宏幸, 林攀梅, 井上光輝, “磁性フォトニック結晶を用いた磁気光学3次元ディスプレイの基礎特性”, 日本電子材料技術協会 第50回秋期講演大会, P7, p.18, 東京, 日本, 8th November 2013.
13. 磯谷亮介, 鈴木章太, 小林完, 中村和樹, 後藤太一, 高木宏幸, 中村雄一, 林攀梅, 井上光輝, “磁性ガーネット多層構造膜の体積磁気ホログラムの記録・再生特性”, 第19回ボリュームホログラフィックメモリ技術研究会, pp.19-22, 東京, 日本, 21st May 2014.
14. 中村和樹, 後藤太一, 高木宏幸, 林攀梅, 井上光輝, “磁性フォトニック結晶を用いた広視野角磁気光学3次元ディスプレイの光利用効率向上”, 電気学会 基礎・材料・共通 (A) 部門大会, 21-B-a2-5, p.14, 長野, 日本, 21st August 2014.
15. 高木宏幸, 工藤慧, 中村和樹, 後藤太一, Lim Pang Boey, 井上光輝, “磁気光学3次元ディスプレイのカラー化に関する基礎研究”, 第38回日本磁気学会学術講演会, 2pC-11, p.53, 横浜, 日本, 2nd September 2014.
16. 中村和樹, 高木宏幸, 後藤太一, Lim Pang Boey, 井上光輝, “磁気光学3次元ディ

- スプレイによるグレーレベルホログラム表示の基礎研究”, 第 38 回日本磁気学会学術講演会, 2pC-15, p.57, 横浜, 日本, 2nd September 2014.
17. 松上一樹, 根本重紀, 中村和樹, 後藤太一, 高木宏幸, 林 攀梅, 井上光輝, “磁気光学 3 次元ディスプレイのための熱磁気記録光学系の研究”, 電子情報通信学会 電子部品・材料研究会(CPM), Vol.114, No.237, CPM2014-97, p.25-28, 東京, 日本, 8th October 2014.
 18. 根本重紀, 松上一樹, 中村和樹, 後藤太一, 高木宏幸, 林攀梅, 井上光輝, “希土類-遷移金属薄膜による磁気光学 3 次元ディスプレイのピクセル形成エネルギーの低減”, 電子情報通信学会 電子部品・材料研究会(CPM), CPM2014-119, p.65-68, 長野, 日本, 25th October 2014.
 19. 津田宗太郎, 中村和樹, 後藤太一, 高木宏幸, 林 攀梅, 井上光輝, 電子情報通信学会 電子部品・材料研究会(CPM), CPM2014-120, p.69-73, 長野, 日本, 25th October 2014.
 20. 酒井将生, 工藤慧, 中村和樹, 後藤太一, 高木宏幸, 林攀梅, 井上光輝, “磁性フォトニック結晶の広角化に関する研究”, 電気学会マグネティックス研究会, MAG-15-073, pp.13-16, 長岡, 日本, 4th August 2015.
 21. 工藤慧, 中村和樹, 酒井将生, 後藤太一, 高木宏幸, 林攀梅, 井上光輝, “カラー用磁性フォトニック結晶の設計”, 第 39 回日本磁気学会学術講演会, 08aD-8, p.52, 名古屋, 日本, 8th September 2015.
 22. 工藤慧, 中村和樹, 酒井将生, 後藤太一, 高木宏幸, 林攀梅, 井上光輝, “磁気光学 3 次元ディスプレイのカラー化”, 平成 27 年電気学会 基礎・材料・共通部門大会, 18-B-p2-4, pp.166-171, 金沢, 日本, 18th September 2015.
 23. 津田宗太郎, 中村和樹, 高木宏幸, 後藤太一, 林 攀梅, 井上光輝, “人工磁気格子を用いた磁気光学 3 次元ディスプレイに関する研究”, 平成 27 年電気学会 基礎・材料・共通部門大会, 18-B-p2-5, pp.172-177, 金沢, 日本, 18th September 2015.
 24. 根本重紀, 山崎和樹, 津田宗太郎, 工藤慧, 中村和樹, 後藤太一, 高木宏幸, 林攀梅, 井上光輝, “磁気光学 3 次元ディスプレイの書き込みエネルギーの低減および回折効率の向上”, 電子情報通信学会 CPM 研究会, CPM2015-95, pp.55-58, 長岡, 日本, 7th November 2015.
 25. 酒井将生, 工藤慧, 中村和樹, 後藤太一, 高木宏幸, 林攀梅, 井上光輝, “磁気光学 3 次元ディスプレイのための磁性フォトニック結晶の角度依存性の改善”, 電子情報通信学会 CPM 研究会, CPM2015-96, pp.59-62, 長岡, 日本, 7th November 2015.
 26. 倉橋秀之, 中村和樹, 後藤太一, 高木宏幸, 中村雄一, 林攀梅, 内田裕久, 井上光輝, “磁気光学空間光変調器のための有機金属分解法によるビスマス置換ネオジム鉄ガリウムガーネットの作製”, 電子情報通信学会 電子部品・材料研究会 (CPM),

CPM2016-24 (2016-07) ,pp.1-4, 松山, 日本, 22nd July 2016.

27. 中村和樹, 後藤太一, 高木宏幸, Lim Pang Boey, 内田裕久, 井上光輝,
“ a -TbFe/BiDyAl:YIG 積層構造を用いた磁気光学 3 次元ディスプレイの高効率化”,
第 40 回日本磁気学会学術講演会, 08aE-8, 金沢, 日本, 8th October 2016.

Award

1. 優秀賞, 日本電子材料技術協会第 50 回秋季講演大会, (November 2013)
2. “IEEJ Excellent Presentation Award”, IEEJ, (September 2015)